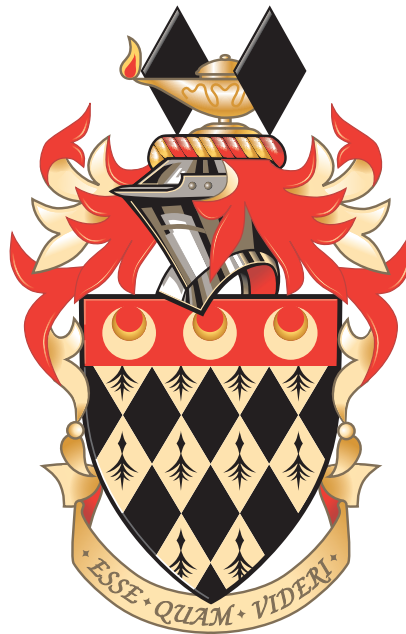# Search for Dileptonic $t\bar{t}H(H \rightarrow b\bar{b})$ with the ATLAS Detector

Benjamin Charles Sowden

Department of Physics

Royal Holloway, University of London

A thesis submitted to the University of London
for the degree of Doctor of Philosophy

11th May 2017

Declaration

I confirm that the work presented in this thesis is my own. Where information has been derived from other sources, I confirm that this has been indicated in the document.

Benjamin Charles Sowden

Abstract

A search for the Higgs boson produced in association with a pair of top quarks (t$\bar{\text{t}}$H) is presented. The analysis uses $13.2\,\text{fb}^{-1}$ of proton-proton collision data with a centre of mass energy of 13 TeV, collected by the ATLAS experiment at the LHC in 2015 and 2016. The search is optimised for events in which the top quarks decay into electrons or muons and the Higgs boson decays into bottom quarks.

The analysis proceeds by separating the events into categories determined by the number of jets present in the event, and the number of those jets which are identified as originating from bottom hadrons. Multivariate techniques are used in the most signal rich regions to provide optimal separation between the signal and background processes. Finally, a template likelihood fit is performed simultaneously across all the regions, constraining the uncertainties on the analysis and determining the most likely value for the production cross section of t$\bar{\text{t}}$H.

The search found the best fit production cross section to be $4.6^{+1.4}_{-1.3}(\text{stat})^{+2.6}_{-1.9}(\text{syst})$ times the standard model predicted result. As such the result does not provide significant evidence for the presence of t$\bar{\text{t}}$H and a 95% confidence limit was set on the production. It is found that the cross section is disfavoured with values higher than 10.1 times the standard model expected value.

Studies are presented showing the inclusion of event quality variables into the multivariate classifier used in the analysis and the inclusion of colour flow variables into both the multivariate classifier and multivariate reconstruction algorithms used in the analysis. For both sets of variables no significant improvement to the performance of the algorithms was seen.

Acknowledgements

This thesis would not exist today without the help and support of many people throughout my studies, and all those who got me here.

Firstly, I would like to thank my supervisor, Glen Cowan, for providing the ideas on which the studies in this thesis are based and the help and direction to complete them. I would also like to thank the other academics, post-docs and students at Royal Holloway who have provided their time (and code) aiding me in this endeavour.

Beyond the academic support provided I would like to thank all those at Royal Holloway, including those previously mentioned and others, for the enjoyable time I have had in Egham (who would have thought it possible?). There were many people who helped me feel welcome at the university both during the work day and in the evenings.

During my studies I have spent longer based at CERN in Geneva than in Egham and as such there are too many people to explicitly name who made my time there unforgettable. The LTA welcomed me back at CERN and provided me with many a much needed respite from work and I would like to thank everyone who joined me on our adventures there. Also, as much as it pains me, I would like to thank those there for honouring me with such ridiculous titles as 'queen of the LTA' and 'glorious leader'.

After returning from CERN I am indebted to my friends and family in London who have kept me on the right side of sanity while enduring the process of birthing this document. Collectively you have made a painful process more bearable. A small collection of these people even went above and beyond, voluntarily subjecting themselves to reading it and finding many places where my writing was lacking, to those I am especially grateful.

I would like to thank the STFC for providing me the funding to carry out this research, and for contributing towards the construction and operation of the LHC without which this research could not have occurred. Finally, I am also grateful to all the people who have put effort into building and running the LHC and the ATLAS experiment which made the fantastic data set I have enjoyed investigating.

Contents

List of Figures

List of Tables

Introduction

The Standard Model of particle physics has been very successful at predicting the interactions of fundamental particles with high precision. In 2012 the only undiscovered particle predicted by the Standard Model, the Higgs boson, was observed by the ATLAS and CMS experiments [1, 2]. Since 2012 there has been extensive work investigating the newly discovered Higgs boson and measuring its properties [3, 4]. While significant progress has been made understanding this new particle there are still large uncertainties on its exact properties. The experiments at the LHC plan to continue exploring these properties along with proposed future experiments targeted specifically at measuring the boson with high precision [5].

This thesis focusses on the measurement a single property of the Higgs boson, its coupling to the top quark. This measurement is difficult to perform because of the high mass of the Higgs boson and even higher mass of the top quark. The high top quark mass means the Higgs boson does not decay to top quarks so the coupling needs to be measured through the production of the Higgs boson in association with top quarks. The work in this thesis focusses on this process with the top quarks decaying leptonically and the Higgs boson decaying into bottom quarks. The cross section of this process is directly proportional to the strength of the coupling between the Higgs boson and the top quarks so gives a direct measurement.

The content of this thesis will be presented in the following order:

- Chapter 1 provides a broad overview of the Standard Model of particle physics focussing on the electroweak symmetry breaking and introduction of the Higgs boson. This is followed by a review of the current experimental status of the Higgs boson. The production methods of the Higgs boson in a hadron collider are presented along with the way in which it decays. Finally a brief summary of the use of the $t\bar{t}H$ process to probe the top Yukawa coupling is covered along with a justification for the importance of measuring the top Yukawa coupling with high precision.

- Chapter 2 introduces the Large Hadron Collider and ATLAS experiment which were used to collect the data presented in this thesis. The various subsystems of the ATLAS detector are described detailing the relevant components within each.

- Chapter 3 describes the ATLAS trigger system, focussing on the inner detector tracking trigger. The performance of the inner detector tracking trigger on the first data collected at 13 TeV is presented for both the electron and muon triggers. The analysis of the performance of the triggers was previously presented by the author at the meeting of the Division of Particles and Fields of the American Physical Society in 2015 [6].

- Chapter 4 explains the process for producing simulated events predicted by the Standard Model which can be compared to the data collected and the algorithms used within the ATLAS collaboration to reconstruct the objects which caused the signals in the detector.

- Chapter 5 details the analysis procedure and results of the search for $t\bar{t}H(H \rightarrow b\bar{b})$ using 13.2 fb^{-1} of data collected by the ATLAS detector in 2015 and 2016. This analysis has previously been presented by the ATLAS collaboration at the ICHEP conference in 2016 [7].

- Chapter 6 presents two studies in which new variables are investigated for use in improving the signal sensitivity of the analysis presented in Chapter 5. Both studies look at classes of variable that have not previously been considered for use in the analysis and test the utility of their addition.

- Chapter 7 summarises the findings presented in the thesis, presents the full combined $t\bar{t}H$ result from ATLAS and provides a brief discussion of the future for the search for $t\bar{t}H(H \rightarrow b\bar{b})$.

The work contained in this thesis was carried out as part of the ATLAS collaboration. The nature of work carried out in a collaboration means that it can be difficult to isolate the work of a single collaborator from the whole. As such the work presented is a combination of the work carried out both by the author and by other members of the collaboration. The split between the two can be summarised as follows.

Chapters 1, 2 and 4 do not contain work by the author but are a review of the theoretical and experimental aspects relevant for the topic of this thesis. The content

for these chapters originate in the theoretical literature and experimental results and reports, all sources for this have been provided as references in the relevant sections.

Chapter 3 details the author's work on evaluating the performance of the inner detector trigger. While the evaluation of the performance was carried out by the author, the trigger itself and software tools used during the evaluation were the work of other members of the ATLAS collaboration.

The analysis presented in Chapter 5 was carried out by the author as part of an analysis team in ATLAS. The author contributed in a continuous manner to the effort of this analysis providing evaluation of the developing quality of the prediction of data both as the tools for prediction were improved by other members of the collaboration and new data was collected. Furthermore the author played a vital role in the processing of the data from the centrally provided data in the ATLAS collaboration to the inputs to the fit during which the selections and corrections are applied. Finally the author contributed all the work towards the fake lepton estimation performed as part of the analysis.

The studies presented in Chapter 6 are entirely the work of the author with all data processing and analysis performed by the author.

Unless otherwise stated all tables and figures in the thesis were produced by the author.

Chapter 1

Theory and Motivation

This chapter introduces the theoretical motivation for the thesis and highlights recent experimental results. In Section 1.1 the Standard Model of particle physics [8–11], the theory behind the process being investigated in the thesis, is described. Particular focus is given to the particle content of the theory and the forces described by the theory in Section 1.1.1 followed by the mathematical construction of the model in Section 1.1.2 and the introduction of electroweak symmetry breaking and the Higgs boson [12–17] in Section 1.1.3. These sections of this chapter are based on descriptions found in [18] and [19].

Details of the discovery of the Higgs boson and the latest experimental results are given in Section 1.2. The different ways in which the Higgs boson is produced and decays in hadron colliders are explained in Section 1.2.1. Justification for specifically investigating the $t\bar{t}H$ process and the experimental status of the search for $t\bar{t}H$ is described in Section 1.2.2. Finally the use of the $t\bar{t}H$ process to measure the top Yukawa coupling is discussed along with the importance of measuring the top Yukawa coupling in Section 1.2.3.

1.1 The Standard Model of Particle Physics

The Standard Model of particle physics (SM) is a theory that attempts to describe the fundamental particles and their interactions. It provides a framework that allows the rate at which processes involving the fundamental particles occur to be calculated. The theory covers three of the four forces of nature: the electromagnetic, weak nuclear force and strong nuclear force. Gravity has not yet been incorporated into the framework of

the SM as there is currently no quantum description of gravity that can be combined with the rest of the theory. This omission is not important for current particle physics colliders as the gravitational force is negligibly small when compared to the other forces at the energies they probe (up to $\mathcal{O}(10^4)$ GeV). In order to probe gravity at colliders it is expected that a collision energy corresponding to the Planck mass ($\mathcal{O}(10^{19})$ GeV) would be required. The SM contains elementary particles that can be categorised into the three generations of quarks and leptons collectively known as fermions which make up matter, the gauge bosons which act as mediators for the forces described in the model and the Higgs boson which is the smallest possible excitation of the Higgs field which gives the other particles their mass.

The SM is a renormalisable quantum field theory based on the invariance under transformations of the gauge group

$$SU(3)_\text{C} \times SU(2)_\text{L} \times U(1)_\text{Y}. \tag{1.1}$$

The three constituent groups of the gauge group lead to the three fundamental forces described by the SM. The first, $SU(3)_\text{C}$, is the group of Quantum Chromodynamics (QCD) which describes the strong nuclear force where the C refers to colour, the charge associated with this force. The next two groups combined, $SU(2)_\text{L} \times U(1)_\text{Y}$, are the groups of the unified ElectroWeak theory (EW) which describes the electromagnetic and weak forces, here L refers to left-handed weak isospin and Y refers to hypercharge.

1.1.1 Particle Content and Interactions

The SM describes many particles; in order to classify these particles in their different types a few properties of the particles are needed to identify their unique set of quantum numbers. First the spin of each of the particles can be used to separate the particles into two types of matter, fermionic and bosonic. Particles with a half-integer spin ($\frac{1}{2} + n, n \in \mathbb{N}$) are known as fermions and obey Fermi-Dirac statistics, whereas those with integer spin ($n, n \in \mathbb{N}$) are known as bosons and obey Bose-Einstein statistics.

Table 1.1: The fermions in the Standard Model, charges are given in units of electron charge (masses from [20]).

Name	Symbol	Electric Charge	Mass
Quarks			
Up	u	$+\frac{2}{3}$	2.2 MeV
Down	d	$-\frac{1}{3}$	4.7 MeV
Charm	c	$+\frac{2}{3}$	1.27 GeV
Strange	s	$-\frac{1}{3}$	96 MeV
Top	t	$+\frac{2}{3}$	173.21 GeV
Bottom	b	$-\frac{1}{3}$	4.18 GeV
Leptons			
Electron	e	-1	0.51 MeV
Electron neutrino	ν_e	0	<2 eV
Muon	μ	-1	106 MeV
Muon neutrino	ν_μ	0	<0.19 MeV
Tau	τ	-1	1.78 GeV
Tau neutrino	ν_τ	0	<18.2 MeV

Fermionic Content

The fermions are the particles with half integer spin; the fundamental fermions can be seen in Table 1.1. While fermions can have any half integer spin, all the fundamental fermions in the SM have a spin of $\frac{1}{2}$. The only fermions observed with different spin are bound states of the fundamental particles. The fundamental fermions in the SM can be further subdivided into the quarks and leptons, within which there are two types each and three generations within each type. The quarks and leptons can be distinguished by the way in which they interact via the four fundamental forces.

Quarks interact via all four of the fundamental forces; they can be separated into the up and down types. The up-type quarks, the up, charm, and top quarks, all have an electric charge with a magnitude $\frac{2}{3}$ that of the electron and positive sign. The down-type quarks, the down, strange, and bottom quarks, all have an electric charge with a magnitude $\frac{1}{3}$ that of the electron and negative sign. All the members of each type share the same quantum numbers except their generation and mass. The mass increases with generation with the heaviest quarks in each type being the top and bottom quarks, and the top being the heaviest quark by more than one order of

Table 1.2: The bosons in the Standard Model and the interactions they mediate, charges are given in units of electron charge (masses from [20]).

Spin 1 - Gauge Bosons					
Interaction	Associated Charge	Name	Symbol	Electric Charge	Mass
Electromagnetism	Electric Charge	Photon	γ	0	0
Weak	Weak Isospin	W boson	$W^{\pm}$	± 1	80.4 GeV
		Z boson	Z	0	91.2 GeV
Strong	Colour	Gluon	g	0	0

Spin 0 - Scalar Boson			
Name	Symbol	Electric Charge	Mass
Higgs boson	H	0	125.09 GeV

magnitude. For each force the quarks interact with there is an associated charge; as they interact via the strong force they each have a colour charge.

Unlike the quarks, leptons possess no colour charge and as such do not interact via the strong force. The leptons are also split into two types: the charged leptons and the neutral leptons (neutrinos). The charged leptons, the electron, muon, and tau, each have an electromagnetic charge equal to the electron charge, which by convention has a negative sign. The neutrinos, the electron neutrino, muon neutrino, and tau neutrino, possess no electric charge. As with the quarks, the charged leptons share the same quantum numbers except for their generation and mass. Once more mass increases with generation with the tau being the heaviest lepton. The neutrinos also share the same quantum numbers, however their mass is much smaller than that of the other SM particles and is not well known experimentally.

Each of the fermions also has an anti-particle partner which shares the same mass but with opposite charge (e.g. electric, lepton, colour, etc.). The anti-particles are typically referred to with the same symbols as their particle equivalents but with a bar across the top, for example the anti-top symbol is $\bar{t}$.

The Forces and Bosonic Content

There are three forces described in the SM, each of which has a corresponding charge and mediators: its gauge bosons. The force carriers of the SM are bosonic particles, that is to say particles with an integer spin, listed in Table 1.2. There are 13 bosons in the SM: the photon, two W bosons, the Z boson, 8 gluons and the Higgs boson. The Higgs boson is different to the other bosons in that it does not mediate a force but is instead associated with the Higgs field from which the mass of the fundamental particles is derived.

The electromagnetic force is mediated by the massless and electrically neutral photon. The electromagnetic force couples to particles with a electromagnetic charge with a magnitude proportional to the particle's charge.

The weak force is mediated by three bosons, the two W bosons and the Z boson. It couples to particles with a strength proportional to their weak isospin. The right chiral fermions have zero weak isospin so do not interact via the weak force, the left chiral up-type quarks and neutrinos have $+1/2$ weak isospin and the down-type quarks and charged leptons have $-1/2$ weak isospin. The W bosons have weak isospin equal to their charge, the Z boson and photon have a weak isospin of zero and the Higgs boson has a weak isospin of $-1/2$. As the mediators of the weak force are massive particles the range of the weak force is relatively small; this means the weak force only has a small effect at low energies.

The weak force allows for flavour changing interactions such as the decay d $\rightarrow$ u which occurs when a neutron decays into a proton. The probabilities of such interactions occurring are quantified in the Cabibbo-Kobayashi-Maskawa (CKM) matrix given in Equation (1.2) [20]. These probabilities enter the cross-section calculation at the vertex between the two different quarks with the W boson. For example it can be seen from the CKM matrix that top quarks almost always decay to bottom quarks; the small numbers in the CKM matrix mean it is said the other

decays are Cabbibo suppressed.

$$
\begin{aligned}
V_{\text{CKM}} &= \begin{pmatrix} |V_{\text{ud}}| & |V_{\text{us}}| & |V_{\text{ub}}| \\ |V_{\text{cd}}| & |V_{\text{cs}}| & |V_{\text{cb}}| \\ |V_{\text{td}}| & |V_{\text{ts}}| & |V_{\text{tb}}| \end{pmatrix} \\
&= \begin{pmatrix} 0.97434^{+0.00011}_{-0.00012} & 0.22506^{+0.00050}_{-0.00050} & 0.00357^{+0.00015}_{-0.00015} \\ 0.22492^{+0.00050}_{-0.00050} & 0.97351^{+0.00013}_{-0.00013} & 0.0411^{+0.0013}_{-0.0013} \\ 0.00875^{+0.00032}_{-0.00033} & 0.0403^{+0.0013}_{-0.0013} & 0.99915^{+0.00005}_{-0.00005} \end{pmatrix}
\end{aligned}
\tag{1.2}
$$

The strong force is mediated by massless gluons, they do not have any electromagnetic charge or weak isospin but they do have colour charge. The strong force couples to colour charge, only quarks and gluons have colour charge so gluons only interact with quarks or themselves. Each gluon carries the equivalent of a colour and an anti-colour charge however the physical gluons states are made from superpositions of the possible colour, anti-colour pairs leading to 8 physical gluons. Due to the self interactions of gluons the strong force becomes weaker at smaller length scales, a phenomenon known as asymptotic freedom. The increased strength at larger length scales leads to the creation of quark, anti-quark pairs when colour charges are separated as the energy in the attraction becomes large enough for the creation. These pair produced quarks are seen in collider experiments when two quarks are produced with large relative momentum, a collection of pairs is made near each one which causes a spray of bound quark states in the direction of the quarks observed as jets in the detector.

1.1.2 Building the Standard Model

The Standard Model is a renormalisable quantum field theory; in order to maintain the property of renormalisability it is required that the Lagrangian of the model is invariant under gauge transformations. The requirement that the theory is renormalisable allows the theory to provide predictions at all orders of perturbation theory, allowing the theory to predict our observation.

The gauge transformations are applied to the fields in the Lagrangian, to illustrate this take the example of the Lagrangian for a free real massless scalar field

$$\mathcal{L} = \frac{1}{2}(\partial_\mu \phi)^2, \tag{1.3}$$

for this example consider a local U(1) gauge transformation defined by

$$\phi \to i e^{ie\alpha(x_\mu)} \phi. \tag{1.4}$$

As the Lagrangian is dependent on the derivative with respect to x_μ the Lagrangian is not conserved under this transformation, showing local phase invariance is not possible for a free theory. The invariance can be added by transforming the partial derivative into a covariant derivative

$$\partial_\mu \to D_\mu = \partial_\mu - ieA_\mu$$
$$A_\mu \to A_\mu + \frac{1}{c}\partial_\mu \alpha(x), \tag{1.5}$$

where A_μ is a vector field. The transformation of the vector field is also given, which is required to be as described in order for the Lagrangian to remain unchanged under the local transformation. This example shows that in order to maintain invariance under the local U(1) symmetry it was required to introduce a vector field into the theory. In a theory which only considers the electromagnetic force, e.g. quantum electrodynamics, only a local U(1) gauge symmetry is required to describe the interactions. In this case the vector field (A_μ) describes the electromagentic force with the photon arising as quantisations of the field.

The Standard Model is built from a more complex local symmetry, so next consider the case of an invariance under an SU(2) × U(1) gauge transformation. In this case once more the U(1) symmetry introduces a vector field B_μ and the SU(2) symmetry introduces three vector fields W_μ^k, $k \in 1, 2, 3$. In this form the vector fields introduced do not correspond directly to the observed bosons but a combination of the fields leads to the observed bosons. The physical W bosons can be identified as

$$W_\mu^\pm = \frac{1}{\sqrt{2}}\left(W_\mu^1 \mp iW_\mu^2\right). \tag{1.6}$$

This leaves the Z boson and photon which can be identified from the combination of the W_μ^3 and B_μ fields

$$
\begin{aligned}
A_\mu &= +B_\mu \cos \theta_W + W_\mu^3 \sin \theta_W \\
Z_\mu &= -B_\mu \sin \theta_W + W_\mu^3 \cos \theta_W,
\end{aligned}
\tag{1.7}
$$

where θ_W is the weak mixing angle.

This gives the interactions and physical bosons from the electroweak theory. Quantum chromodynamic theory can be added in a similar manner by also requiring the Lagrangian to be invariant under a local SU(3) gauge transformation. This process will introduce an extra eight vector fields which correspond to the eight gluons observed, each a superposition of the different colour states.

This theory does a good job of describing physical processes involving these forces, but there are no terms in the Lagrangian which provide mass to either the gauge bosons or the fermions. The boson mass terms could be added to the Lagrangian by hand by adding terms of the form $\frac{1}{2} m_X^2 X^\mu X_\mu$ for those particles with an observed mass. Doing this would have the undesirable effect of breaking the gauge invariance that was established making the theory no longer renormalisable and violating the symmetry principle on which the model was constructed. Instead the masses of the gauge bosons and fermions are introduced to the model by spontaneously breaking the SU(2) × U(1) gauge symmetry through the introduction of the Higgs field.

1.1.3 Electroweak Symmetry Breaking and the Higgs Mechanism

The process of electroweak symmetry breaking allows for the addition of the boson and fermion masses to the theory while maintaining invariance under the local SU(2) × U(1) gauge transformation. The first step is to introduce the Higgs potential as a new term in the Lagrangian, this is in addition to the terms previously added as

$$
\mathcal{L}_{\text{SM}} = \mathcal{L}_{\text{QCD}} + \mathcal{L}_{\text{EW}} + \mathcal{L}_{\text{Higgs}}.
\tag{1.8}
$$

As part of introducing this term a new complex scalar doublet is introduced. In order for it to provide mass to both the neutral Z boson and the charged W bosons it needs to contain a charged complex scalar field ϕ^+ and neutral complex scalar field ϕ^0. The

minimal Higgs model introduces these as

$$\phi = \begin{pmatrix} \phi^+ \\ \phi^0 \end{pmatrix}. \tag{1.9}$$

This is then added to the Lagrangian with the new term taking the form

$$\mathcal{L}_{\text{Higgs}} = \left(D_\mu \phi\right)^2 - V(\phi), \tag{1.10}$$

where $V(\phi)$ is the Higgs potential given by

$$V(\phi) = \mu^2 \phi^\dagger \phi + \lambda (\phi^\dagger \phi)^2. \tag{1.11}$$

For positive values of μ^2 and λ the symmetry of the system is maintained. However, in the case that $\mu^2 < 0$ and $\lambda > 0$, new minima are formed in which the symmetry is broken. The potential formed by asserting $\mu^2 < 0$ and $\lambda > 0$ can be seen pictured in Figure 1.1. The minimum of this potential is no longer found at the origin, instead there is an infinite set of degenerate minima located at

$$\phi^\dagger \phi = -\frac{\mu^2}{2\lambda} \equiv \frac{v^2}{2}, \tag{1.12}$$

which means the field has a non-zero vacuum expectation value. This new fundamental state is no longer invariant under the $\text{SU}(2) \times \text{U}(1)$ transformation, i.e. both the symmetries are broken.

This process of breaking the symmetry is known as spontaneous symmetry breaking since the symmetry of the Lagrangian is maintained while the symmetry of the ground state is broken. Goldstone's theorem states that for spontaneously broken symmetries a new massless scalar boson is introduced for each generator of the symmetry that is broken [21]. These additional massless scalar bosons can be absorbed into the physical W and Z bosons as longitudinal degrees of freedom through the use of a gauge transformation. Since the neutral photon is massless the degenerate minima is chosen such that the Higgs field that acquires the non-zero vacuum expectation value is the neutral scalar field defined by

$$\langle 0|\phi|0\rangle = \frac{1}{\sqrt{2}} \begin{pmatrix} 0 \\ v \end{pmatrix}. \tag{1.13}$$
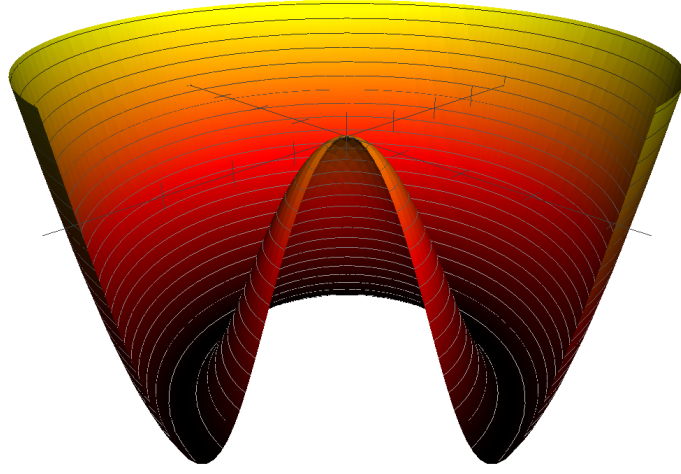
Figure 1.1: Plot of the Higgs field potential $V(\phi)$ with a negative value for μ shown with one quarter of the distribution removed for clarity.

The field can then be expanded around the minimum to give

$$\phi(x) = \frac{1}{\sqrt{2}} \begin{pmatrix} 0 \\ v + h(x) \end{pmatrix}, \tag{1.14}$$

where $h(x)$ represents fluctuations around the minima in the direction perpendicular to the degenerate continuum of minima.

Once again in order for the theory to be renormalisable it must be invariant under local gauge transformations. In order to do this a new covariant derivative is introduced along with the relevant field transformations. The kinetic term of the Higgs Lagrangian, once this covariant derivative has been introduced, can be expanded to reveal the mass terms of the gauge bosons. From this it can be shown that the W bosons have identical mass proportional to the weak coupling constant g_W and the vacuum expectation value of the Higgs field given by

$$m_W = \frac{1}{2} g_W v. \tag{1.15}$$

As with the electroweak theory the W_μ^3 and B_μ fields mix into the two physical particles, A and Z, with masses

$$m_A = 0, \quad m_Z = \frac{1}{2} v \sqrt{g_W^2 + g'^2}, \tag{1.16}$$

where g' is the coupling associated with the $U(1)_Y$ gauge symmetry.

This has solved the problem of the masses of the gauge bosons but there are still no terms to the Lagrangian which account for the fermion masses. This can be solved by adding a term to the Higgs Lagrangian in which the Higgs doublet couples to the fermion fields. This term takes the form

$$\begin{aligned} \mathcal{L}_f &= y_f(\bar{f}_L \phi f_R + \bar{f}_R \phi f_L) \\ &= \frac{y_f}{\sqrt{2}}(\bar{f}_L f_R + \bar{f}_R f_L)(v + h), \end{aligned} \tag{1.17}$$

where f_L (f_R) are the left (right) handed fermions fields and y_f are the Yukawa couplings to the fermions. This additional term is invariant under the local SU(2)xU(1) gauge transformation so does not prevent the renormalisabilty of the theory. The Yukawa couplings are not predicted by the Higgs theory but it can be seen from the first term in the above Lagrangian that they are proportional to the masses of the fermions with the values given as

$$y_f = \sqrt{2}\frac{m_f}{v}. \tag{1.18}$$

The second term in the Lagrangian gives the interaction between the fermions and the Higgs boson with strength proportional to the Yukawa terms. Since these are proportional to the fermion mass the fermions couple to the Higgs boson in proportion to their mass.

1.2 The Higgs Boson

The Higgs boson was discovered at the Large Hadron Collider (detailed in Section 2.1) in July 2012 by both the ATLAS [1] and CMS [2] experiments. Since this discovery, more detailed analysis of the mass [3] and couplings [4] of the Higgs boson have been performed combining the results of the ATLAS and CMS collaborations using the data collected in 2011 and 2012 at $\sqrt{s} = 7$ and 8 TeV. From this combination the best mass measurement finds the Higgs boson's mass to be

$$m_H = 125.09 \pm 0.21(\text{stat}) \pm 0.11(\text{syst}) \text{ GeV}. \tag{1.19}$$

At the time of writing, all measurements of the properties of the Higgs boson discovered in 2012, including the spin, parity and couplings, have been consistent with the Standard Model predictions. This consistency is illustrated in the results of the combined ATLAS and CMS fit to the various production and decay modes shown in Figure 1.2. Details on the different production and decay modes can be found in the next section.

1.2.1 Higgs Boson Production and Decay

The Standard Model predicts the Higgs boson can be produced in a number of ways in a proton-proton collider. The four main production mechanisms searched for at the LHC are gluon-gluon fusion (ggF), vector boson fusion (VBF), associated vector boson production (WH/ZH) and associated top pair production t$\bar{\text{t}}$H. Illustrative tree level Feynman diagrams for these production mechanisms are shown in Figure 1.3.

The four processes are given in the order of their production cross-sections, the values of which are given in Table 1.3. The production cross section for the different processes is known to different orders of perturbation theory for the different process detailed in [22]. The t$\bar{\text{t}}$H cross section calculated at NLO in QCD+EW. It can be seen that ggF is the dominant production mechanism with over ten times the cross section of the next most probable. It is with this production mechanism that this Higgs boson was discovered in 2012 and it provides the best experimental constraints on the properties of the Higgs boson due to the large number of events of this type recorded.

1.2.2 t$\bar{\text{t}}$H

The Higgs boson couples to all massive particles with a coupling strength proportional to their mass. The various Higgs boson production and decay modes give insight into the exact strength of each of these couplings, the measurement of which is an important cross-check of the Standard Model prediction. While ggF has the highest predicted production cross section it contains a fermionic loop. In the Standard Model the top quark is the dominant fermion in the loop but many beyond the Standard Model predictions include significant contributions from undiscovered particles. As such the measurement of couplings between the Higgs boson and the particles in the loop is very model dependent. VBF and associated vector boson production give
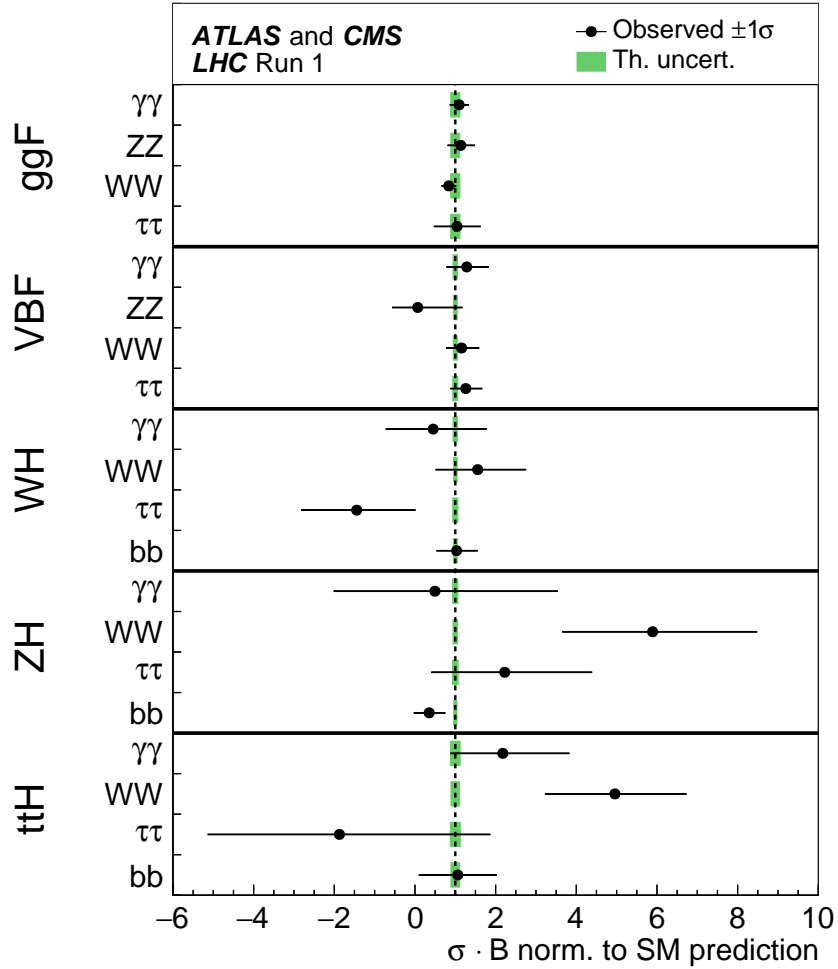
Figure 1.2: Best fit values of the cross section times branching ratio for measured Higgs boson production and decay channels, as obtained from the generic parametrisation with 23 parameters for the combination of the ATLAS and CMS measurements. The results are normalised to the Standard Model prediction for each channel. Missing production and decay channels are not shown due to no measurement being available or the available measurement having non-meaningful precision. Note the results shown are illustrative and the significance of each can not be precisely inferred from this visualisation alone. Furthermore, only the ggF(H $\rightarrow \gamma\gamma$) channel provides a discovery significance in isolation, the Higgs boson properties are measured from a combination of all the measurements shown (from [4]).
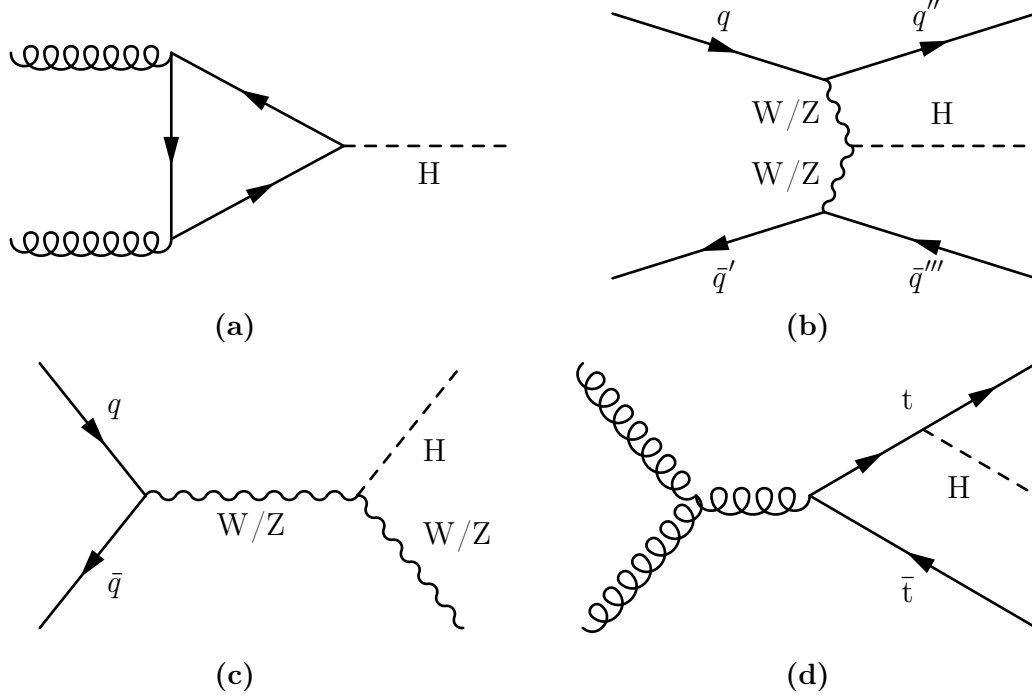
Figure 1.3: Illustrative leading-order Feynman diagrams of the main Higgs boson production channels at the LHC: (a) gluon-gluon fusion, (b) vector boson fusion, (c) associated vector boson production and (d) associated top pair production.

Table 1.3: Table of the production cross-sections at 13 TeV and branching ratios of the Standard Model Higgs boson with the best measured mass of 125.09 GeV. Cross-section errors are theory errors for ggF, combined QCD scale, PDF and strong coupling errors for b$\bar{\text{b}}$H and just QCD scale errors for the other processes. Errors on the branching ratio are from theoretical uncertainties (numbers from [22]).

Higgs boson production cross section at 13 TeV (pb)						
ggF	VBF	WH	ZH	t$\bar{\text{t}}$H	b$\bar{\text{b}}$H	tH
$48.5^{+4.6\%}_{-6.7\%}$	$3.92^{+0.5\%}_{-0.2\%}$	$1.37^{+0.5\%}_{-0.7\%}$	$0.882^{+3.8\%}_{-3.0\%}$	$0.507^{+5.8\%}_{-9.2\%}$	$0.486^{+20.1\%}_{-23.9\%}$	$0.0771^{+6.5\%}_{-14.9\%}$

Higgs branching ratios				
b$\bar{\text{b}}$	WW	gg	$\tau\tau$	c$\bar{\text{c}}$
$0.581^{+0.65\%}_{-0.65\%}$	$0.215^{+0.99\%}_{-0.99\%}$	$0.0818^{+3.40\%}_{-3.41\%}$	$0.0626^{+1.17\%}_{-1.16\%}$	$0.0288^{+1.20\%}_{-1.20\%}$
	ZZ	$\gamma\gamma$	Others	
	$0.0264^{+0.99\%}_{-0.99\%}$	$0.00227^{+1.73\%}_{-1.72\%}$	0.00202	

better measurements of the couplings through the decay channels as they only have dependence on the vector boson couplings and provide extra particles in the final state with which events containing Higgs bosons can be isolated from background processes. However, these production mechanisms do not give insight into the coupling of the top quark to the Higgs boson as its mass is not large enough to allow it to decay to on-shell top quarks. This leaves $t\bar{t}H$ and tH as the main mechanisms through which to probe the Higgs boson's coupling to the top quark due to the presence of the Higgs-top vertex. $t\bar{t}H$ has a cross section over six times that of tH meaning a far greater sample of events with which to probe the coupling.

$t\bar{t}H$ has been searched for in 2012 at the LHC by both the ATLAS [23–26] and CMS [27, 28] collaborations. The results for four of the Higgs boson's decay channels can be seen combined between ATLAS and CMS in Figure 1.2, in this combination the combined significance for the observation of $t\bar{t}H$ production was found to be 4.4σ (expected 2.0σ) with the best fit cross section observed to be $2.3^{+0.7}_{-0.6}$ times the Standard Model expected rate [4].

In this thesis the search for $t\bar{t}H$ is targeted only at events in which the Higgs boson decays into a b-quark pair and the top quarks decay leptonically. For this specific signature the ATLAS collaboration found a best fit cross section of $2.8^{+2.0}_{-2.0}$ times the standard model prediction [26] and the CMS collaboration find a best fit cross section of $1.0^{+3.3}_{-3.0}$ times the standard model prediction [28].

1.2.3 The Top Yukawa Coupling

The values of the Standard Model parameters, as measured in experiment, lead to a theory which remains consistent to energy scales up to and beyond the Planck scale. Beyond this scale the effects of gravity are expected to become significant. However, deviations in the parameters within the error of the experimental measurements can lead to a situation in which the vacuum expectation value of the Higgs field becomes unstable. Due to the variation of the parameters of the model as a function of the energy regime, at large energy scales new minima can form in the potential. These minima can have values such that they are unstable with the minima previously laid out remaining the global minima or they can be new global minima, which would change the vacuum expectation value and in some models mean the universe becomes unstable [29].
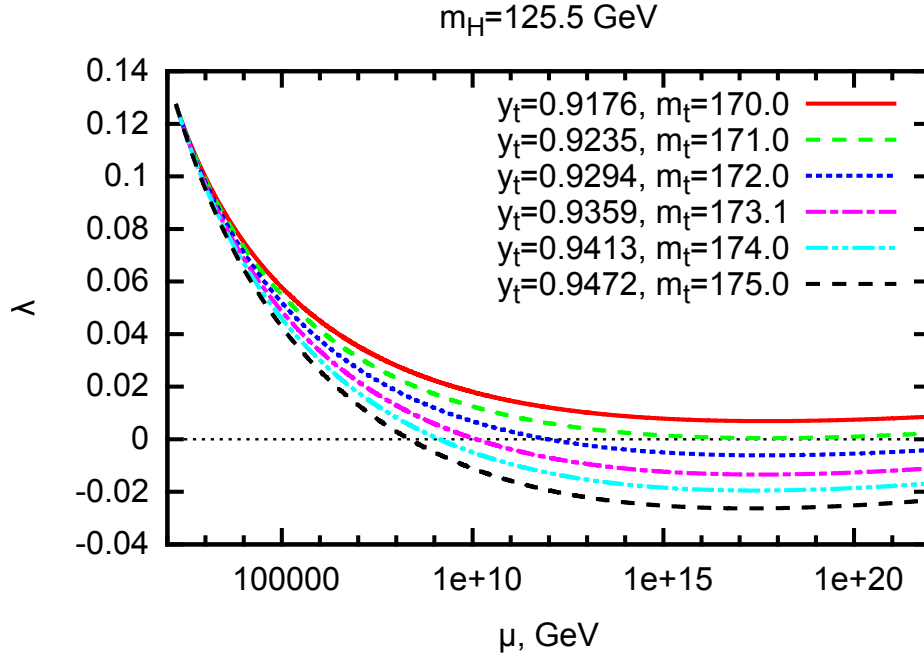
Figure 1.4: Renormalisation group running of the Higgs self-coupling λ shown given the mass of the Higgs boson being 125.5 GeV with several values of the top Yukawa coupling y_t (from [29]).

The change of the potential from having the single minimum to becoming unstable can be considered as happening as a function of the Higgs self-coupling (λ) with negative values of the Higgs self-coupling leading to an unstable potential. The variation of the Higgs self-coupling with the energy scale (μ) can be seen in Figure 1.4 for many values of the top Yukawa coupling. This shows that for small variations in the top Yukawa coupling, large changes in the energy dependence of the self-coupling occur. Some of these mean the change in the potential can occur many orders of magnitude lower than the Planck scale, which would require a new theoretical model to explain. As such a precise measurement of the top Yukawa coupling is necessary to determine at what energy scale the vacuum becomes unstable and at what scale new physics is expected.

The top Yukawa coupling gives the the strength of the coupling between the top and the Higgs boson. The $t\bar{t}H$ cross-section is directly proportional to the square of the top Yukawa coupling due to the presence of the Higgs-top vertex in the calculation. Therefore, a measurement of the $t\bar{t}H$ cross-section can be directly reinterpreted to give a measurement of the top Yukawa coupling.

Chapter 2

The LHC and ATLAS

This chapter provides details on how the data used in this thesis was produced, describing the accelerator complex and detector. First the Large Hadron Collider is introduced in Section 2.1 along with the properties of the collisions it produces and the accelerator complex that supplies it. Next the ATLAS detector is described in Section 2.2 with sections on each of the subdetectors found within and their performance at detecting particles.

2.1 The LHC

The Large Hadron Collider (LHC) is the world's largest particle accelerator, producing particles with the highest energy ever produced in a laboratory. It was designed to accelerate and collide protons with energy up to 7 TeV [30], combining to a centre of mass energy of 14 TeV, seven times higher than the previous highest energy collider. This record breaking energy is achieved through the use of a series of accelerators connected in series culminating with the LHC as depicted in Figure 2.1.

First the protons are obtained through the ionisation of hydrogen gas and initially accelerated in the 33.3 m long accelerating cavities of the LINAC 2. The LINAC 2 is a linear accelerator originally commissioned in 1978 which delivers the protons in bunches to the Proton Synchrotron Booster (PSB) with an energy of 50 MeV [31]. The PSB splits the bunches into four stacked circular synchrotron rings, each 157 m in circumference, simultaneously accelerating them. It accelerates the protons from LINAC 2 up to an energy of 1.4 GeV. Next the protons enter the Proton Synchrotron (PS), a 628 m circumference synchrotron made from 277 non-superconducting magnets.
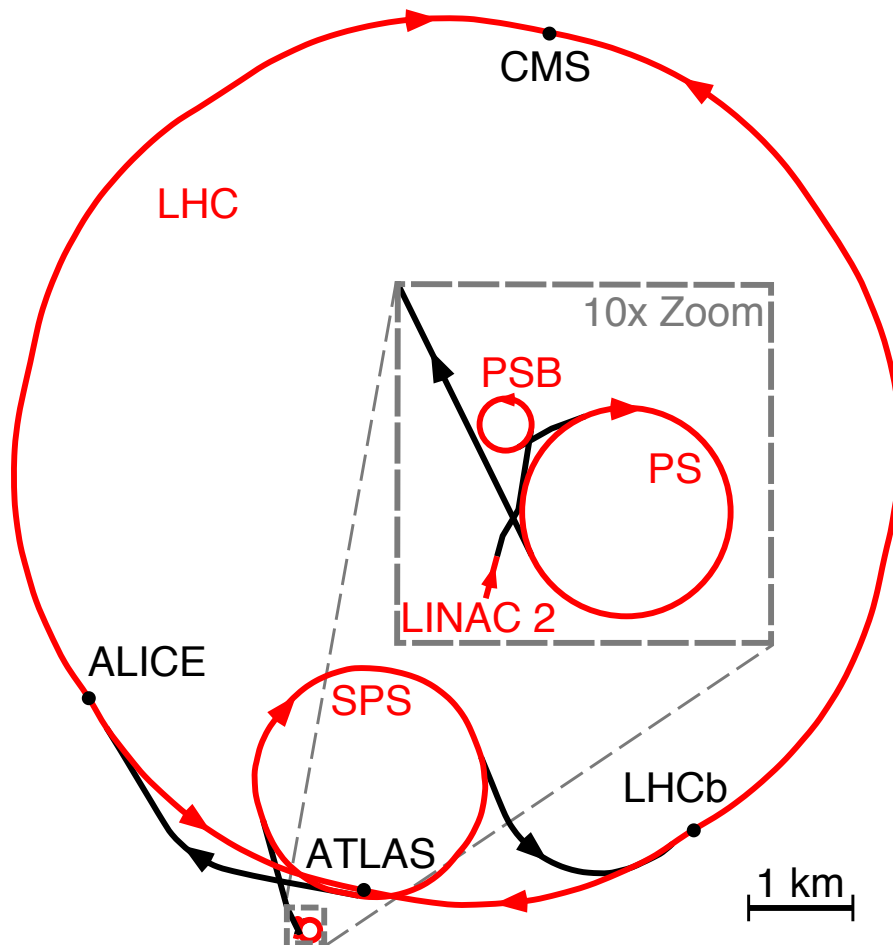
Figure 2.1: Diagram of the LHC accelerator complex at CERN showing the injection chain and the four major experiments on the ring, drawn to scale.

Table 2.1: The design and delivered beam properties for the LHC, showing the evolution from Run 1 to Run 2 and the improvement achieved after the 2015 commissioning year. The 2016 information only takes into account the period for which data was collected for this thesis, up until 10th July 2016.

Parameter	Design value	2012	2015	2016
Beam energy (TeV)	7	4	6.5	6.5
Beta function β* (m)	0.55	0.6	0.8	0.4
Max. num. bunches/beam	2808	1380	2232	2064
Max. num. protons/bunch	1.15×10^{11}	1.7×10^{11}	1.21×10^{11}	1.25×10^{11}
Bunch spacing (ns)	25	50	25	25
Peak luminosity ($\text{cm}^{-2}\,\text{s}^{-1}$)	1.0×10^{34}	7.6×10^{33}	5.0×10^{33}	1.0×10^{34}
Max. average in-time pileup	19	36.2	28.1	34.4

It accelerates the protons to 25 GeV and forms the bunch train structure for the LHC. The protons are then further accelerated by the larger Super Proton Synchrotron (SPS) measuring nearly 7 km in circumference, made from 1,317 non-superconducting magnets. It brings the proton's energy up to LHC injection energy of 450 GeV. The LHC is a 27 km circumference ring made up of 1,232 main dipole magnets to bend the beam around the ring, 392 quadrupole magnets used to focus the beam and thousands of other magnets to fine-tune and control the beam. As previously stated, the LHC was designed to accelerate the protons to 7 TeV, however this has not yet been achieved with the highest energy attained at the time of writing this thesis being 6.5 TeV.

In Table 2.1 the evolution of the LHC operating parameters can be seen. The years before 2012 when the LHC was being commissioned and was operating with a beam energy of 3.5 TeV have been omitted. The running of the LHC up until 2012 is collectively known as Run 1 in which almost 29 fb^{-1} of proton-proton collisions were delivered to the experiments around the LHC ring. Since then, in 2015 and 2016, the energy of the LHC beams has been increased to 6.5 TeV during what is known as Run 2. This thesis uses the 13.2 fb^{-1} of proton-proton collisions delivered by the LHC in Run 2 up until 10th July 2016. The evolution of data taking over the years of operation can be seen in Figure 2.2.

There are four major detectors situated on the LHC ring: ATLAS, CMS, LHCb and ALICE. ATLAS and CMS are on opposite sides of the ring and were designed to study a broad range of physics processes. LHCb and ALICE are one eighth of the
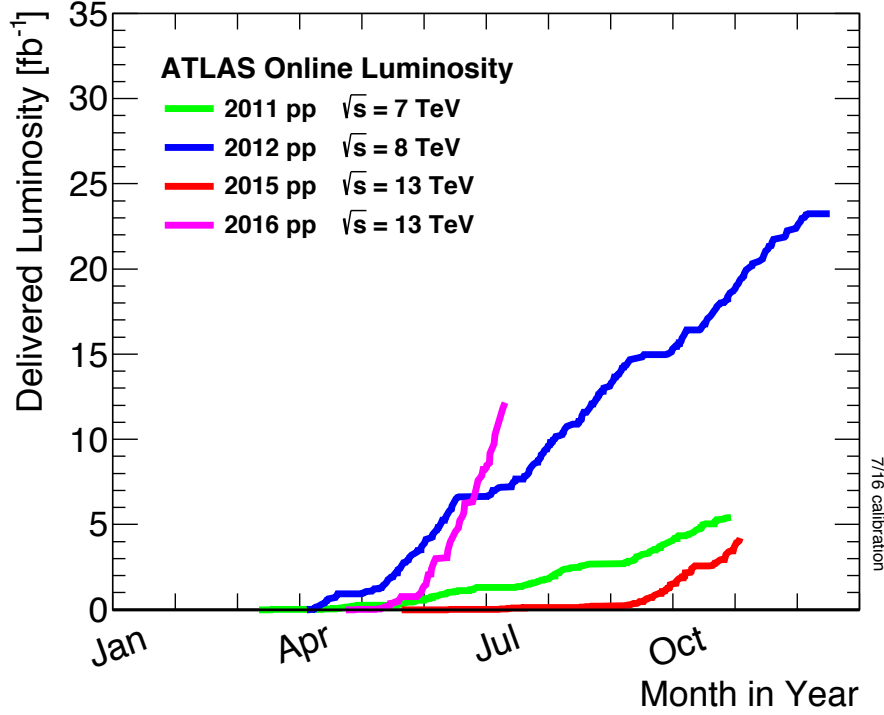
Figure 2.2: Evolution of proton-proton collision data collected by the ATLAS experiment during different years of LHC operation (from [32]).

ring away from ATLAS on either side. LHCb is an asymmetric detector entirely in the forward direction, designed to precisely measure decays of b and c hadrons. The ALICE detector was specifically designed in order to study the very high intensity collisions of heavy ions which the LHC is also capable of accelerating.

2.2 The ATLAS Detector

The ATLAS detector is the world's largest general purpose particle detector. It is 45 m long and 25 m in diameter and weighs approximately 7000 t. It has a cylindrical shape, as shown in Figure 2.3, and is made up of four subsystems: the magnet systems, the inner detector, the calorimeters, and the muon spectrometers. It was designed to be hermetic, detecting particles in all directions from the interaction point, allowing a measurement of the missing transverse momentum from which invisible particles can be inferred.

ATLAS uses a right-handed coordinate system with its origin at the nominal interaction point in the centre of the detector and the z-axis along the beam pipe in
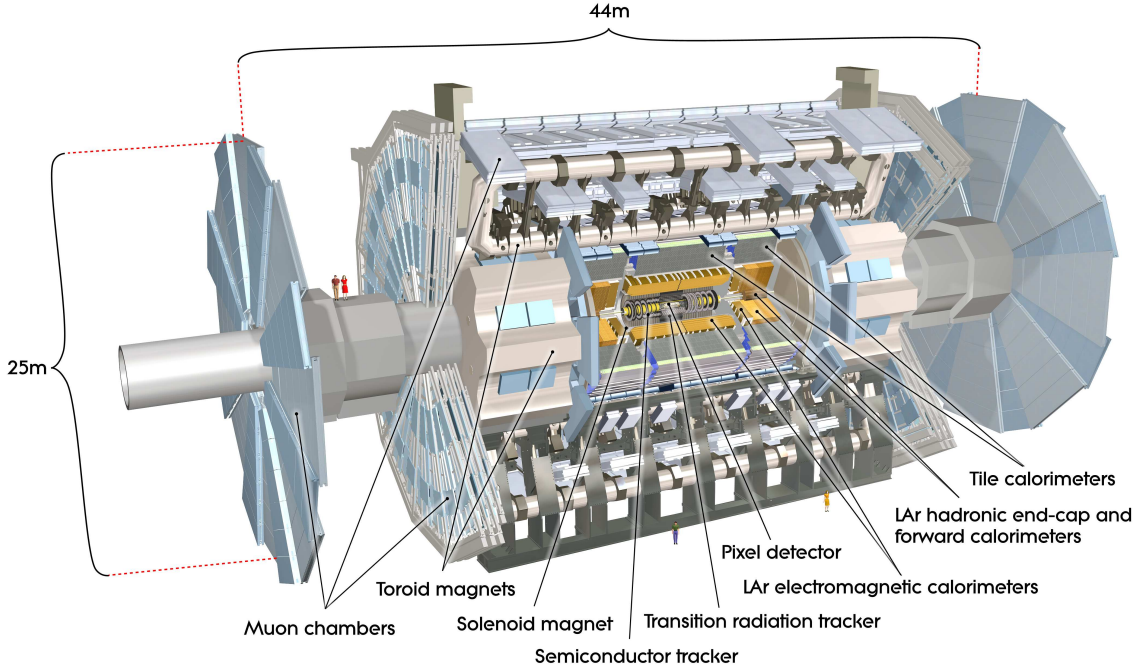
Figure 2.3: Diagram of the ATLAS detector highlighting major components within it (from [33]).

the anti-clockwise direction. The x-axis points towards the centre of the LHC ring, and the y-axis points upward. Cylindrical coordinates (r, ϕ) are used in the transverse plane, ϕ being the azimuthal angle around the beam pipe. The pseudorapidity is defined in terms of the polar angle θ as $\eta = -\ln \tan(\theta/2)$.

The process being searched for in this thesis has electrons, muons and hadronic jets (see Section 4.2.4) in the final state which will interact with the detector. In order to measure these processes with precision all of the subsystems of ATLAS are utilised. The magnet system detailed in Section 2.2.1 is used to measure the momentum of the charged objects since magnets cause the paths of the charged objects to bend with the curvature of the path being correlated to the momentum. Next the inner detector is described in Section 2.2.2, it is used to provide information on the position of charged particles in the centre of the detector in order to determine the path in which they travelled. The calorimeters are used to measure the energy of charged and neutral particles, with the exception of muons and neutrinos which do not strongly interact with the calorimeters. The calorimeters present in the ATLAS detector are described in Section 2.2.3. Finally in Section 2.2.4 there is a description of the muon detectors which are used to measure the momentum of muons with precision and distinguish their tracks in the inner detector from other charged particles.
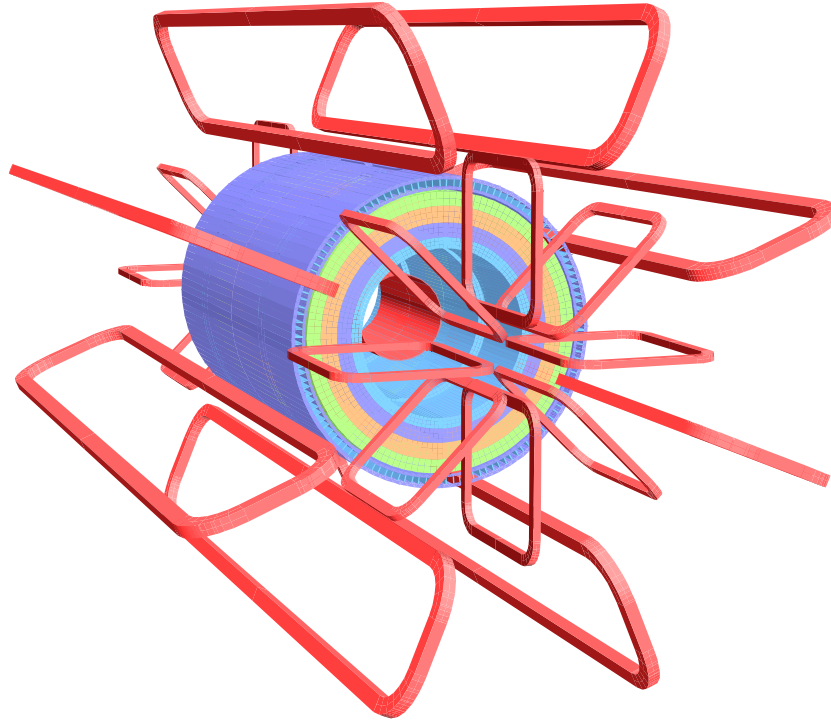
Figure 2.4: Diagram of the ATLAS magnet system windings shown in red along with four layers of the tile calorimeter steel and return yoke (from [33]).

2.2.1 The Magnet System

The ATLAS magnet system is made up of four superconducting magnets: the solenoid, the barrel toroid and two end-cap toroids pictured in Figure 2.4. Collectively they are 26 m long and 22 m in diameter and have a stored energy of 1.6 GJ.

The solenoid is aligned on the beam axis surrounding the inner detector providing a uniform 2 T axial magnetic field. It was specifically designed to reduce the material thickness in front of the calorimeter to prevent a drop off in the calorimeter's performance while maintaining the desired magnetic field within.

The barrel toroid consists of eight separate coils and produces a toroidal magnetic field of approximately 0.5 T for the central muon detectors. The end-cap toroids, each consisting of eight flat, square coils produce a toroidal magnetic field of approximately 1 T required to provide the bending power needed in the end-cap regions of the muon spectrometer.

These strong magnetic fields are required in order to perform momentum measurements of the charged particles. The tracks made by the charged particles are bent by

the magnetic field. Measuring the degree of curvature of the bend gives the momentum of the particle for a known field strength. The magnetic field strength provided by the magnet system allows a large range of particle momenta to be measured by the detector.

2.2.2 The Inner Detector

The inner detector is located within the solenoid magnet and is responsible for the tracking of charged particles produced in the collisions in the ATLAS detector. It is designed to achieve high-precision measurements to enable accurate momentum resolution and measurement of both primary and secondary vertices of the collisions in the range $|\eta| < 2.5$.

It is made up of both cylindrical sections (the barrel) and flat sections on the ends (the end-caps). The inner detector is made up of three independent subsystems, each having both barrel and end-cap sections. These are, in increasing distance from the beam pipe, the Pixel detector, the Semi-Conductor Tracker (SCT) and the Transition Radiation Tracker (TRT) as shown in Figure 2.5.

Pixel detector

The pixel detector is the closest part of the detector to the interaction point. As can be seen in Figure 2.5 the pixel detector is made up of four layers, the innermost of which was added for Run 2 and is known as the Insertable B-Layer (IBL). With the addition of the IBL the pixel detector allows tracking information at only 33.25 mm from the interaction point, allowing discrimination of primary and secondary vertices through very precise measurement of the origin of tracks. The intrinsic resolution of the IBL is 8×40 μm and the intrinsic resolution of the rest of the pixel is 10×115 μm. It is based on silicon semiconductor technology, which detects particles through the combination of two differently doped layers of silicon. When a potential is applied across the boundary a depletion region is formed in which there are no free charge carriers. A charged particle passing through this region can create a electron-hole pair which causes a detectable current. These semiconductor sensors are arranged in a grid in order to give very fine granularity position information.
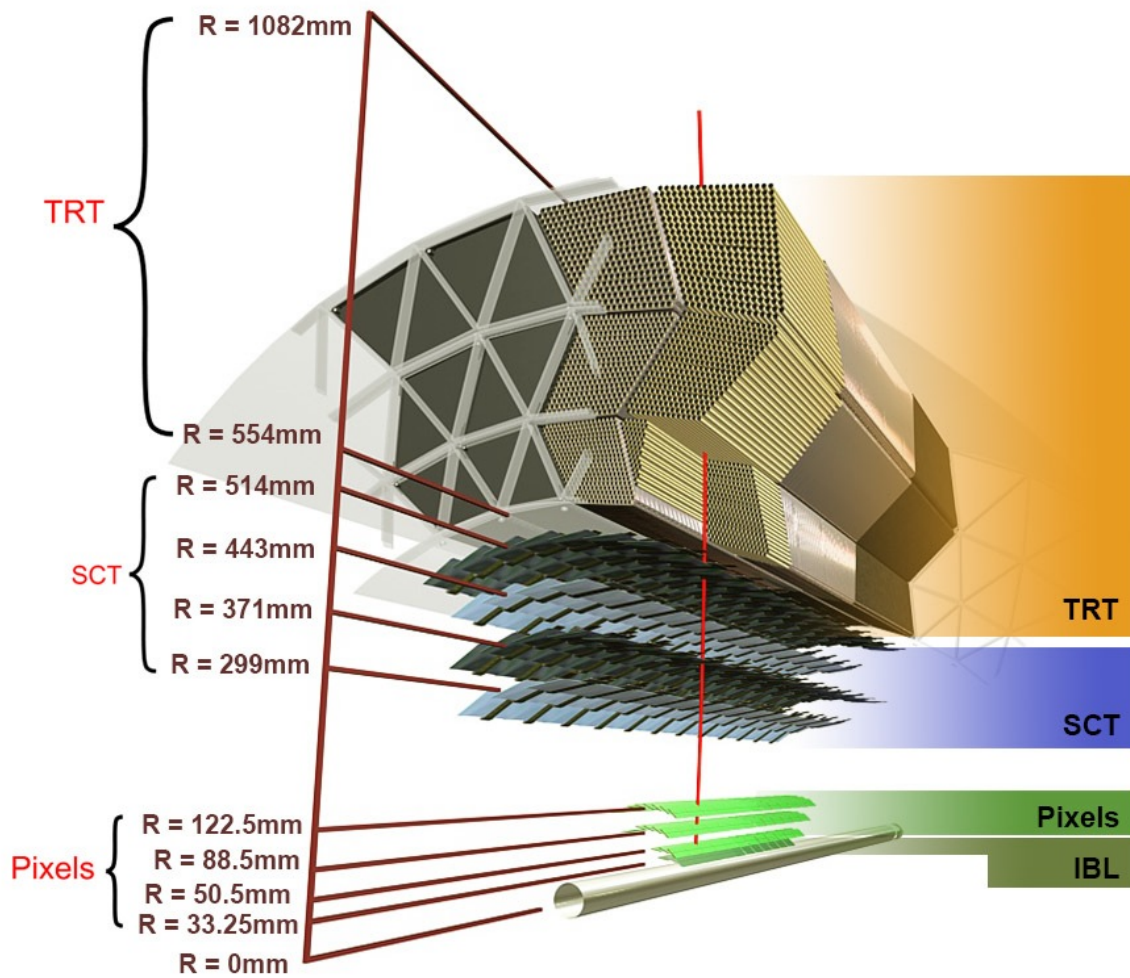
Figure 2.5: A drawing showing a charged particle with a transverse momentum of 10 GeV passing through the inner detector of ATLAS (from [33]).

Semi-Conductor Tracker

The SCT is the next closest detector to the beam-pipe starting at 299 mm from the interaction point. It is also a silicon based detector but in order to cover a large area economically is not pixel based, instead it is a strip based sensor. It detects charged particles though the same mechanism as the pixel detector just with lower granularity. Each strip is ≈80 μm wide, a value chosen to optimise the digitising precision, granularity, particle occupancy and noise performance. The layers of the SCT sensors are in pairs which have a 40 mrad relative rotation, allowing two dimensional measurement of particle location. This gives the SCT an intrinsic resolution of 17 μm. The arrangement of the modules ensure almost complete coverage with at least four precision space-point measurements in any direction covered by the inner detector.

Transition Radiation Tracker

The TRT is the furthest sensor from the beam-pipe in the inner detector starting at 554 mm from the interaction point. Unlike the inner two sensors it is not silicon based but instead is made up of drift tubes. The tubes are made of two multi-layered films attached back-to-back, designed to give the best electrical and mechanical properties while maintaining a very thin cross section. In the centre of the tubes is a thin gold plated tungsten wire, which together with the tubes makes a capacitor, with the wire forming the anode and the tube forming the cathode. The tubes are filled with a gas predominantly consisting of either Xe or Ar that is ionised when charged particles pass through; the electrons (ions) are attracted to the anode (cathode) creating a current in the wire. As the electric field in the tube is known, the distance from the wire can be calculated by using the time the electrons take to drift to the wire. This gives the TRT an intrinsic resolution of 130 μm. Typically between 30 and 40 hits are observed in the TRT when a charged particle traverses it.

The TRT also provides an ability to perform particle identification on the particles that pass through it. This is achieved through the detection of transition radiation photons emitted when a highly relativistic charged particle traverses through a boundary between two media with different dielectric constants. The TRT straws are interleaved with fibres (foils) in the barrel (end-caps) which provide many such boundaries to stimulate transition radiation emission. Typically the transition photons have an energy $\mathcal{O}(\mathrm{keV})$ which are absorbed by the gas, leaving a much larger signal than

the minimum-ionising charged particles. The amount of transition radiation produced is dependent on how relativistic the charged particle is and as such for a given energy particle is dependent on the mass of the particle. This means there is some separation between electrons and heavier charged pions[1].

Performance

Precise tracking is required to measure the properties of the jets and leptons expected in the final state of $t\bar{t}H(H \rightarrow b\bar{b})$ being searched for in this thesis. Furthermore, it is necessary to be able to precisely identify the interaction vertices of the event, including secondary vertices like those used to identify b-jets.

When measuring the transverse momentum of particles with the inner detector the three sub-detectors each provide a similar amount of information, the lack of precision in the TRT is compensated with the increased number of hits. Using information from all three the momentum resolution of the inner detector was found to be:

$$\frac{\sigma_{p_\mathrm{T}}}{p_\mathrm{T}} = 1.6 \pm 0.1\% \oplus \frac{(53 \pm 2) \times 10^{-5}}{\mathrm{GeV}} \times p_\mathrm{T}, \tag{2.1}$$

measured using cosmic muons before the addition of the IBL [34]. This equates to an inner detector momentum resolution of about 1.6% at low momenta (≈ 1 GeV) and of about 50% at 1 TeV.

2.2.3 The Calorimeters

The Calorimeters are situated just outside the solenoid magnet and lie next closest to the beam-pipe after the inner detector. The purpose of the calorimeter is to measure the energy of the particles. This is done through the use of materials which have a high probability of the particles interacting with them. This leads to many successive particle interactions, leaving a large number of low energy particles, known as a shower. The energy of these low energy particles is then measured, the sum of this energy gives the energy of the original particle.

ATLAS uses sampling calorimeters which are made of alternate layers of shower-inducing material and layers of active scintillators to detect the secondary particles.

---

[1]Pions are the bound state of a pair of up or down quarks, or a mixture of the two.
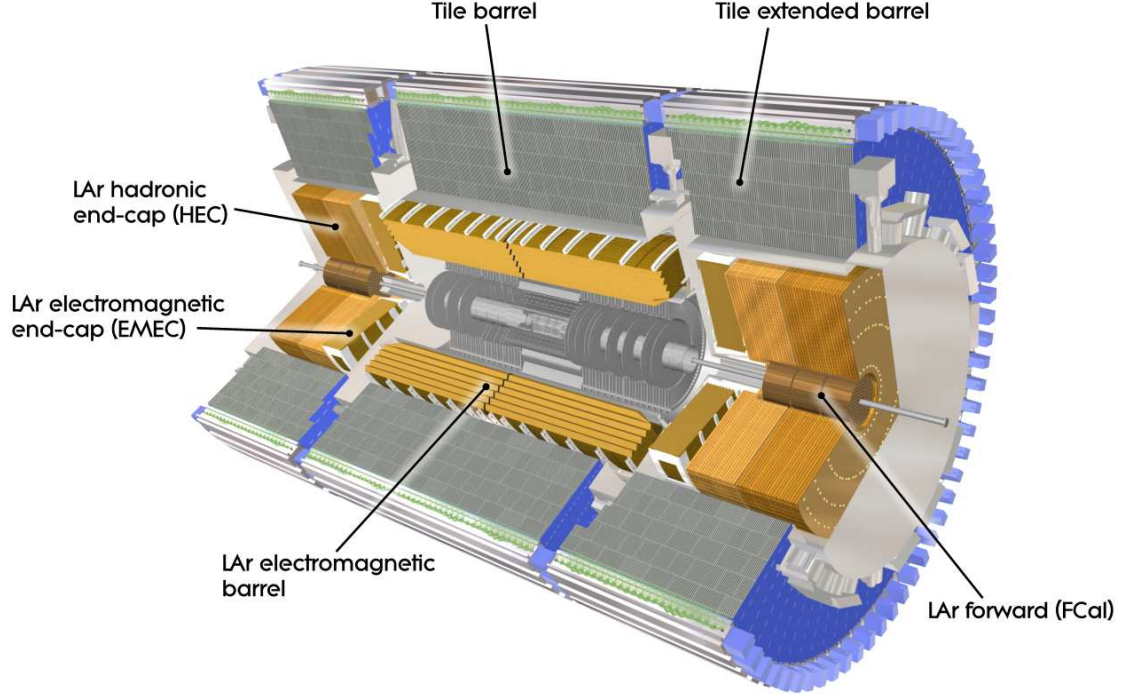
Figure 2.6: A diagram showing the layout of the calorimeters in ATLAS (from [33]).

The Calorimeters are split into the electromagnetic calorimeter primarily used to measure the energy of electrons and photons and the hadronic calorimeter used to measure the energy of hadronic particles. Over the range of the inner detector a fine granularity electromagnetic calorimeter is used for precise measurements of electrons and photons. Outside this range up to $|\eta| < 2.9$ a coarser granularity is used focussing on the ability to reconstruct jets in the detector and calculate the missing transverse energy in the collision.

The layout of the calorimeters can be seen in Figure 2.6. The calorimeters are separated into three cryostats, one for the barrel section and one for each end-cap. In the barrel section there are two types of calorimeter, a Liquid Argon (LAr) based electromagnetic calorimeter and the tile based hadronic calorimeter. In each end-cap there are three types of calorimeter: a LAr ElectroMagnetic End-cap Calorimeter (EMEC), a LAr Hadronic End-cap Calorimeter (HEC) and a LAr Forward Calorimeter (FCal).

An important design consideration when designing a calorimeter is ensuring that the particle showers are contained within the calorimeter to limit the energy lost to the surrounding muon detectors. When considering the containment of a calorimeter it is

(a)   **(b)**

(c)
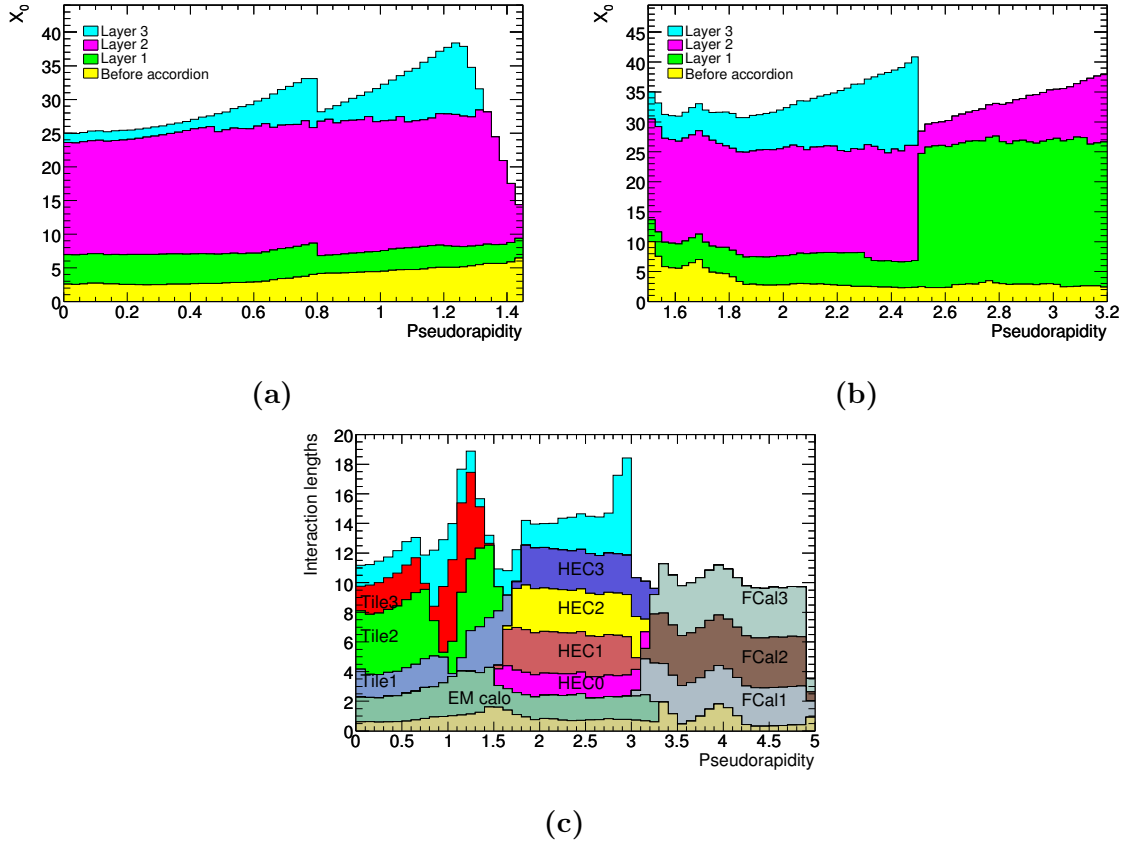
Figure 2.7: On the top, the cumulative distribution of thickness of the electromagnetic
calorimeter layers and the material inside them in units of radiation length for
(a) the barrel region and (b) the end-caps. On the bottom (c), the distribution
of the cumulative thickness of the detector in units of nuclear interaction length
(from [33]).

important to consider both the depth of the calorimeter material in terms of radiation
lengths (X_0) and in terms of nuclear interaction lengths (λ). A radiation length is
defined as the mean distance a charged particle has to travel through a material until
its energy falls to $1/e$ of its initial value due to electromagnetic interactions. A nuclear
interaction length is the mean length a particle has to travel through a medium before
undergoing an inelastic nuclear collision. It is also important to consider the amount
of material in the detector between the interaction point and the calorimeters as this
material leads to a loss of precision in the measurement of energy of particles. The
distribution of the thickness of the detector can be seen in Figure 2.7, where it can be
seen that the calorimeters are thick across the full pseudorapidity range to contain
showers and there is minimal material before them for the inner detector and solenoid
to ensure little loss of precision in measurement of energy.

Cells in Layer 3
$\Delta\varphi \times \Delta\eta = 0.0245 \times 0.05$

Trigger Tower
$\Delta\eta = 0.1$

$2X_0$

$\eta = 0$

470 mm

$16X_0$

Trigger Tower
$\Delta\varphi = 0.0982$

$4.3X_0$

1500 mm

$1.7X_0$

$\Delta\varphi = 0.0245 \times 4$
$36.8\text{mm} \times 4$
$=147.3\text{mm}$

Square cells in
Layer 2

$\Delta\varphi = 0.0245$

$\Delta\eta = 0.025$

φ

$37.5\text{mm}/8 = 4.69$ mm
$\Delta\eta = 0.0031$

Strip cells in Layer 1

η
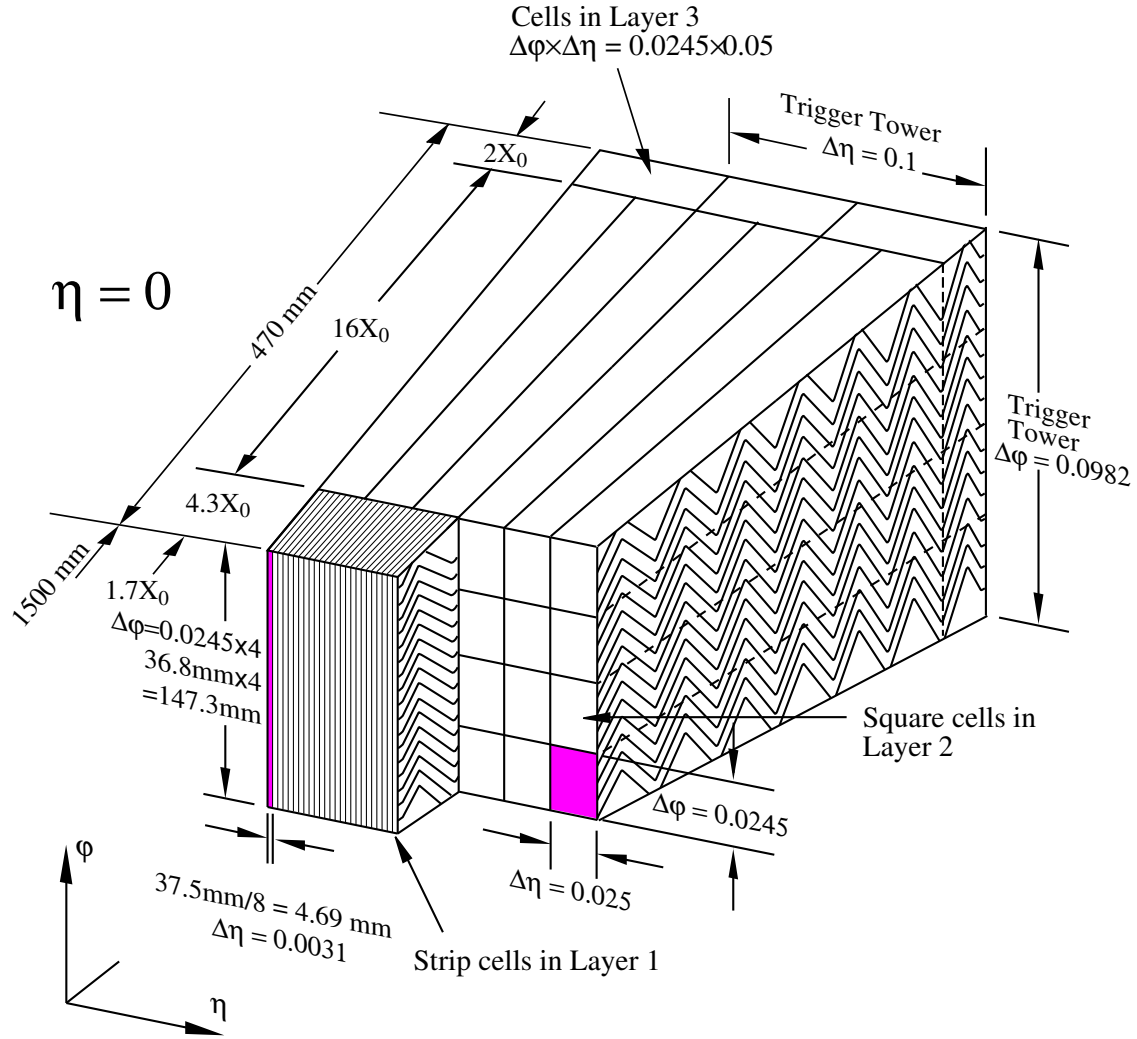
Figure 2.8: A sketch showing the layout of a module of the barrel electromagnetic calorimeter (from [33]).

The Electromagnetic Calorimeter

The electromagnetic calorimeter (ECAL) is a sampling detector made with liquid argon (LAr) as its active detecting layers and lead plates as the shower-inducing layers. LAr was chosen for its linear behaviour and its stability of response over time when exposed to large amounts of radiation. The two layers are arranged in an accordion shape oriented in a radial direction in order to ensure full coverage in ϕ with no cracks between modules.

In the barrel the ECAL is split into three layers radially from the interaction point optimised for different measurements, clearly visible in Figure 2.8. The inner-most

layer of the ECAL has the highest granularity of the three layers in the η direction such that when combined with the second layer the source of deposits can be accurately located in order to identify the primary vertex for photons which leave no tracks with which to derive this information. In the barrel region this layer has a mostly uniform thickness which is much thinner than that of the second layer, as can be seen in Figure 2.7a. The second layer is much thicker, making up the majority of the thickness of the ECAL. This layer is arranged in a square grid with edge length one quarter that of the strip length of the inner layer, aiding in the vertex finding. The final layer has the lowest granularity and is used primarily to distinguish between electromagnetic and hadronic showers and estimate the energy lost beyond the ECAL. In the central region ($|\eta| < 1.8$) there is a pre-sampler included in the 'Before accordion' category of Figures 2.7a and 2.7b, which is a LAr based detector that is used to estimate the energy loss that occurs before the calorimeter.

Each end-cap ECAL is comprised of two co-axial wheels separated by 3 mm at $|\eta| = 2.5$, matching the acceptance of the inner detector. The inner of the two wheels uses the same accordion shape as the barrel and are split into three layers matching the configuration of the barrel ECAL, each layer having a similar thickness as that of the barrel and fulfilling the same purpose. The outer of the two wheels does not have a third layer and the first layer provides the majority of the thickness of the calorimeter. As previously mentioned the pre-sampler covers the more central region of the end-cap ECAL, it is only required up to $|\eta| = 1.8$ as at higher $|\eta|$ there is less dead material within the calorimeter.

The Hadronic Calorimeter

There are three main sections that make up the hadronic calorimeter: the tile calorimeter, the hadronic end-cap calorimeter and the forward calorimeter. The tile calorimeter is the only hadronic calorimeter present in the central region. It is made up of a barrel in the region $|\eta| < 1.0$ and two extended barrels in the region $0.8 < |\eta| < 1.7$. As with the ECAL it is a sampling calorimeter. Unlike the ECAL, it uses steel as the shower-inducing material and plastic scintillating tiles as the active detecting layers. The scintillators are instrumented with wavelength-shifting fibres which direct light to photomultiplier tubes. It can be seen in Figure 2.7c that the tile calorimeter ensures that any leak of hadronic showers is small with over 9

nuclear interaction lengths of material in all but a small region between the barrel and extended barrels.

The hadronic end-cap calorimeter overlaps the tile calorimeter covering the region $1.5 < |\eta| < 3.2$. It is located directly behind the ECal end-caps within the same cryostat. Like the ECal it is a sampling calorimeter with liquid argon as its active material, however it uses copper instead of lead as the shower-inducing material as copper has a shorter nuclear interaction length. For each end-cap there are two independent wheels with the outside wheel having 50 mm copper plates, twice the thickness of the inner wheels. It has greater containment ability than the tile calorimeter with 12 nuclear interaction lengths of material before the muon spectrometer.

Also in the same cryostats is the forward calorimeter which provides coverage up to $|\eta| = 4.9$. The forward calorimeter is a combined electromagnetic and hadronic calorimeter. It is made up of three layers, each using liquid argon as the active detecting material. The first layer uses copper as its shower-inducing material and is optimised as an electromagnetic calorimeter. The second and third layers use tungsten as their shower-inducing material and primarily measure the energy of hadronic particles.

Performance

The performance of the calorimeter is important to get precise measurements of the jet and electron energies used in the analysis presented in this thesis. In particular the accurate position and energy measurement of the b-jets which decay from the Higgs boson allows for the Higgs boson's mass to be accurately reconstructed. This provides a powerful means of identifying events containing a Higgs boson.

The performance of the calorimeter modules has been assessed using test beam data. The experimental measurements have had noise subtracted and are then fit with the expression

$$\frac{\sigma(E)}{E} = \frac{a}{\sqrt{E[\text{GeV}]}} \oplus b, \tag{2.2}$$

where a is the stochastic term and b is the constant term reflecting local non-uniformities in the response of the calorimeter.

The ECAL performance in the barrel was assessed using test beam data with an electron beam fired at a spare electromagnetic barrel module, identical to those in

ATLAS with the same amount of dead material before the calorimeter. The fractional energy resolution obtained can be seen in Figure 2.9a alongside the prediction taken from GEANT (discussed in Section 4.1.2) in which good agreement can be seen. The fitted energy resolution is found to be $\frac{\sigma(E)}{E} = (10.0 \pm 0.4)\%/\sqrt{E} \oplus (0.4 \pm 0.1)\%$. The energy response to electrons is tested to be uniform for the entire coverage of the calorimeter with a variation of no more than 0.7%.

The performance of the calorimeter at detecting hadrons in the barrel was assessed using test beam data with a pion beam fired at a prototype detectors of the LAr electromagnetic and tile calorimeters. The fractional energy resolution obtained can be seen in Figure 2.9b and fitted to Equation (2.2) with an added term to account for electronic noise. The fitted energy resolution is found to be $\frac{\sigma(E)}{E} = (52.0 \pm 1.0)\%/\sqrt{E} \oplus (3.0 \pm 0.1)\% \oplus (1.6 \text{ GeV} \pm 0.1)/E$.

2.2.4 The Muon Spectrometer

The muon spectrometer forms the outermost part of the detector. Due to the containment provided by the calorimeters it is expected that almost no particles other than muons will reach the muon spectrometer[2]. The muon spectrometer is placed within the magnetic field of the three toroidal magnets which deflect the muons being detected to provide information on their charge and momentum. The muon spectrometer provides accurate momentum information for a large range of muon transverse momenta, from ≈ 3 GeV (limited by losses in the calorimeter) up to ≈ 3 TeV. The muon spectrometer has a large acceptance covering a region with $|\eta| < 2.7$.

It can be seen in Figure 2.10 that the muon spectrometer is made up of four technologies, excluding the magnet system. The primary technology for the momentum measurement is the Monitored Drift Tube (MDT), which works in a very similar way to the TRT in the inner detector. It is a collection of 30 mm diameter aluminium tubes containing a Tungsten-Rhenium wire surrounded by a non-flammable Ar-CH$_4$-N$_2$ mixture at a pressure of 3 bar. The resolution a single wire can give on the particle position is 80 μm but this is enhanced by each module having multiple layers of tubes (four for the inner modules and three for the middle and outer modules). Any mechanical deformations in the tubes are monitored by an in-plane optical system to ensure they can be accounted for and the precision maintained.

---

[2]Note invisible particles will also reach, and pass through, the muon spectrometer.
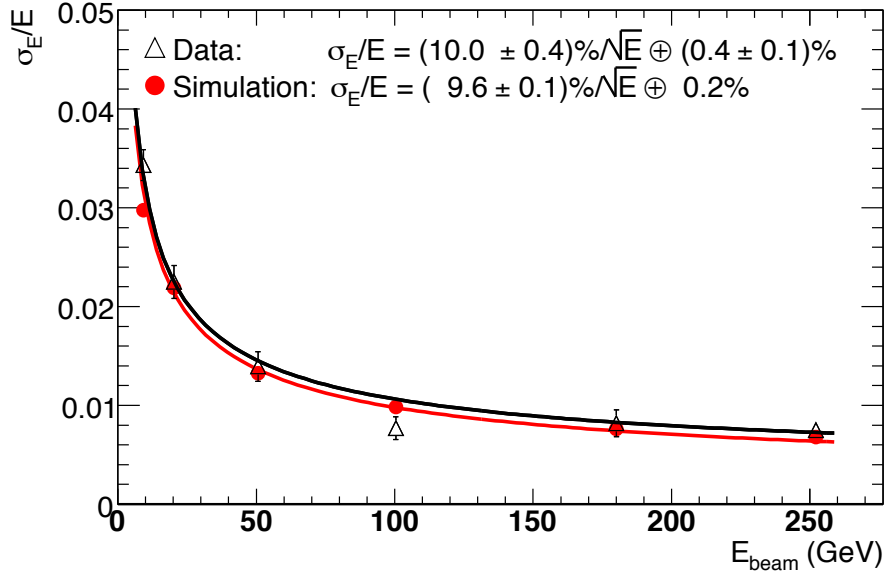
(a)
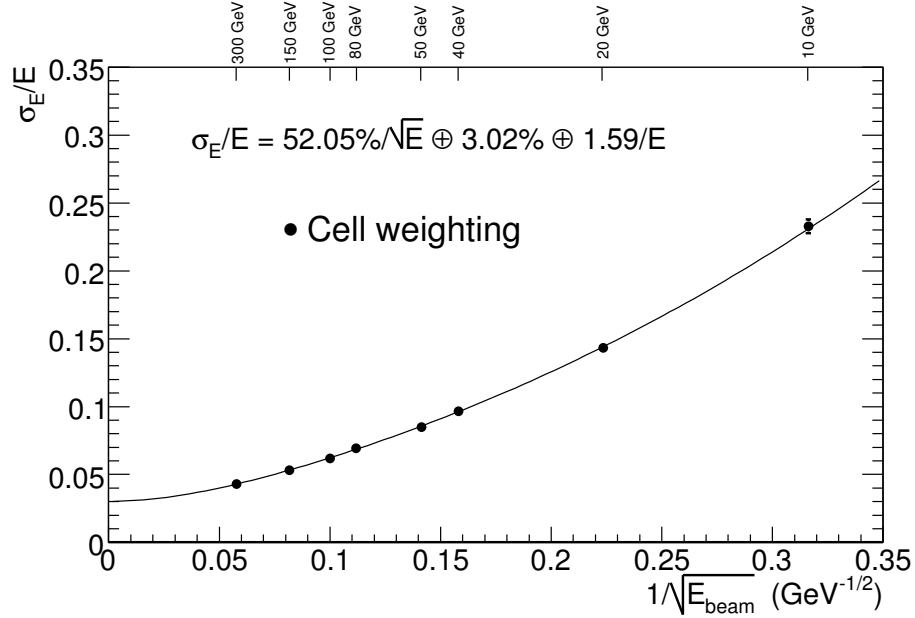
(b)

Figure 2.9: The fractional energy resolution as a function of the (a) electron beam energy for the LAr electromagnetic calorimeter and (b) the pion beam energy for the combined LAr and tile calorimetry. For the test 2.4 X_0 of upstream material was present consistent to the amount present in the ATLAS barrel with $|\eta| < 0.4$ (from [33]).
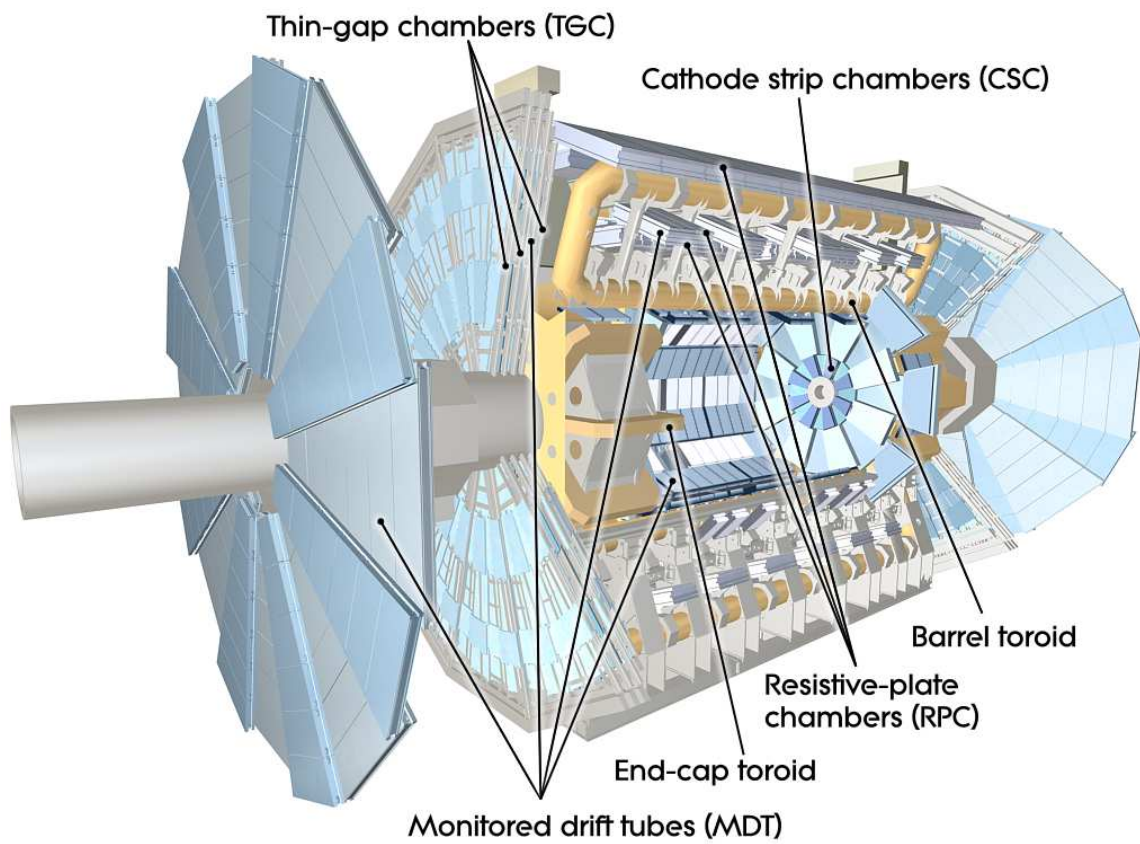
Figure 2.10: Diagram depicting the layout of the various systems that make up the muon spectrometer (from [33]).

In the higher flux regions of the detector (the innermost part of the end-cap and at angles close to the beam-pipe) momentum measurement is instead handled by the Cathode Strip Chambers (CSC) to provide finer granularity and to cope with the demanding rate and background conditions. The CSCs work on a similar principle as the TRT/MDT except instead of tubes there are cathode strips running above and below the anode wires, one set orthogonal to the wires for precision measurement and the other set parallel to the wires providing a measurement of the transverse coordinate. The volume between the strips and wires is filled with a non-flammable mixture of Ar-CO_2-CF_4.

Finally there are the detectors for triggering. These are Resistive Plate Chambers (RPC) in the barrel and Thin Gap Chambers (TGC) in the end-cap. The RPC is once more a gas based detector, however instead of a wire and tube the RPC has two parallel resistive plates held apart by insulating spacers. A uniform electric field causes a limited avalanche multiplication centred around the primary ionisation electron which is detected by aluminium strips separated from the plates by an insulating film. These provide good spacial and time resolution needed for fast space-time particle triggering.

The TGCs are very similar to the CSCs, however the spacing between anode wires is greater than the distance from the wires to the cathodes. The anode wires are placed parallel to the MDT wires and together with the orthogonal strips provide the trigger information. The TGC provides large signals very quickly making it ideal for triggering as the signals are large enough they do not need pre-amplification.

Performance

The precise measurement of muons is important in the analysis presented in this thesis as approximately half the events analysed contain muons in their final state. The resolution of the transverse momentum as a function of the transverse momentum of the muons can be seen in Figure 2.11. It can be seen in this plot that the muon spectrometer primarily improves the momentum resolution at high momenta giving significant improvement above ≈ 50 GeV.
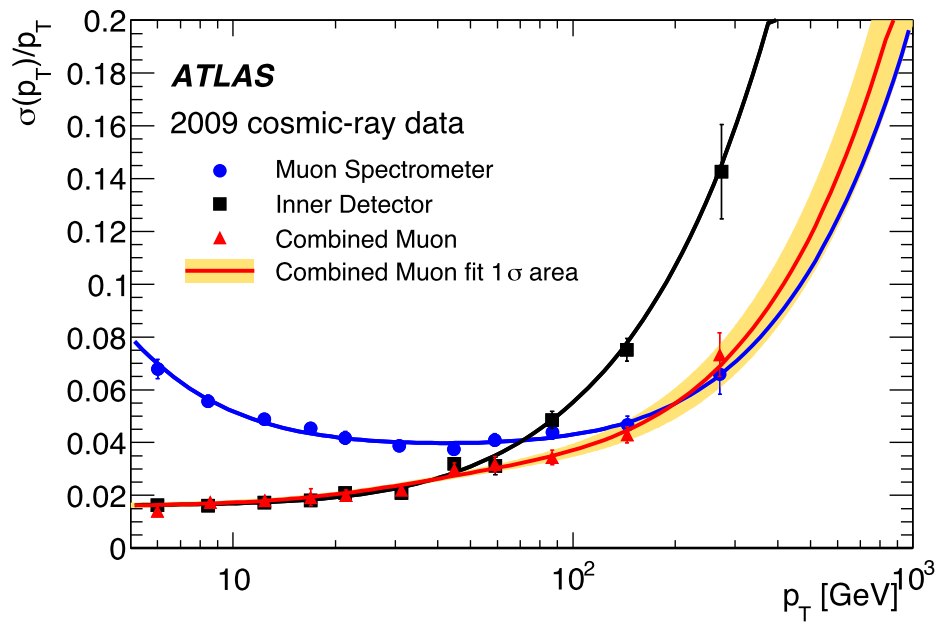
Figure 2.11: Transverse momentum resolution as a function of the transverse momentum for cosmic muons measured with the inner detector, muon spectrometer and combination of the two. The shaded region shows the $\pm 1\sigma$ region of the fit to the resolution curve for the combined tracks (from [34]).

Chapter 3

The ATLAS Trigger System

This chapter introduces the ATLAS trigger and a study of its performance. First, in Section 3.1, the need for a trigger system is described along with the details of the implementation of the trigger in ATLAS. Next, in Section 3.2, the algorithms used in the inner detector tracking trigger are detailed. Finally measurements of the performance of the low transverse momentum single lepton triggers are discussed in Section 3.3. These single lepton triggers are used in all the other work presented in this thesis.

3.1 Introduction

In 2016 the LHC exceeded its design luminosity of 1.0×10^{34} cm^{-2} s^{-1} delivered from proton-proton collisions with bunch crossings occurring at a rate of 40 MHz. Due to limitations in the read out system of ATLAS and in the amount of available storage media it is infeasible to store the detector state after every bunch crossing. As such it is necessary to choose the events to save in order to bring the rate down to a reasonable level. This needs to be done in such a way that will not hinder the physics goals of the experiment by not saving events that contain processes of interest. To achieve this, a real-time system has been implemented, utilising both hardware and software, to determine whether a bunch crossing contains an event of interest. This is known as the trigger system

In Run 2 the increased demand put on the trigger from the increase in collision energy, collision frequency and instantaneous luminosity meant the trigger had to be

upgraded. In both the Run 1 and the upgraded Run 2 triggers, multiple levels are used such that each subsequent level has longer to identify the events of interest.

The first stage, known as the level 1 (L1) trigger, is a pipelined hardware stage. It processes low granularity information from the calorimeter and muon spectrometer to make a decision on the bunch crossing. It receives the 40 MHz input from the collisions and reduces this rate down to a maximum of 100 kHz passed on to the next level of the trigger, with an average decision time less than 2.5 μs. The trigger also passes Regions of Interest (RoIs) generated during the decision process to the next level of the trigger in order to seed the future algorithms. While this was upgraded with respect to Run 1 the architecture of the L1 trigger is unchanged.

The rest of the trigger is made up of software running on a commercially available computer cluster and is known as the high level trigger (HLT). In Run 1 the HLT was split into two levels: the level 2 (L2) and event filter (EF) triggers. The L2 was custom written software which processed data at the full detector granularity within the RoIs from L1. It performed calorimeter reconstruction, the earliest available Fast Tracking, and track-cluster matching. It had a peak output of about 6.5 kHz with an average decision time of about 75 ms. The EF was an optimised version of the standard ATLAS reconstruction software which can run on the full granularity data from the entire detector. It performed the full reconstruction and precision tracking to make the final event selection. It had a peak output rate of about 700 Hz with an average decision time of about 1 s. Each of these stages ran separately with a new node in the computer cluster being assigned to the event between the L2 accepting the event and the event filter making a decision on the event.

In Run 2 the HLT has been merged into a single process running on a single HLT computing cluster node. This simplifies the data-flow removing the need for network communication between the L2 and EF triggers and removes the duplication in requesting data from the DAQ system. It also means the EF trigger doesn't have to first perform event building after the L2 accept as the event building can flexibly be placed as a step during the processing of the algorithms on the single HLT CPU node. The new combined trigger has a peak output rate of about 1 kHz and an average decision time of about 200 ms. A new hardware-based track preprocessor known as the Fast TracKer (FTK) [35] is planned to be added in Run 2. It will process events after the L1 trigger accept in order to seed the HLT algorithms.
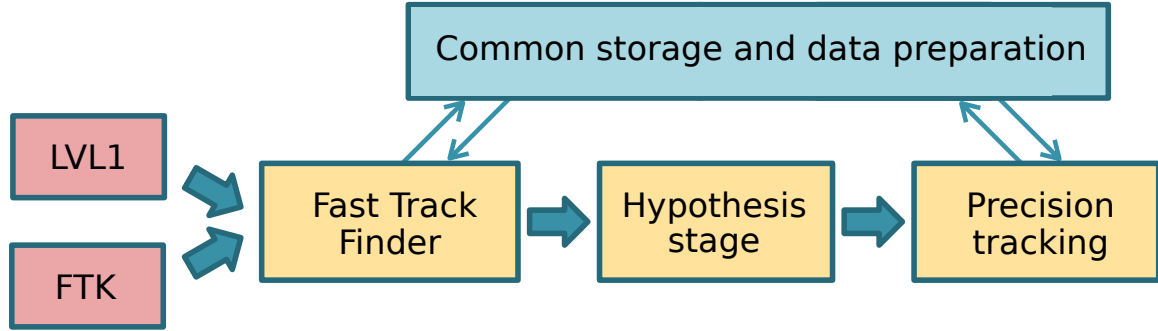
Figure 3.1: Layout of the inner detector tracking trigger in Run 2. Note the FTK is due to be added in 2017 (from [6]).

3.2 The Inner Detector Trigger

The inner detector trigger software has been rewritten to take advantage of the new HLT trigger framework. The same two step structure is retained as can be seen in Figure 3.1. The first step, as with Run 1, is a custom written fast tracking algorithm which performs pattern recognition and tracking on the hit data[1]. This step has been completely re-written with the FTK considered from the start, meaning tracks provided by the FTK can be integrated seamlessly into the system once the FTK is commissioned. This produces a hypothesis for the event which is passed to and used as a starting point for the second step. The second step is precision tracking, which utilises an optimised subset of the tracking algorithms used offline. This second step is slower than the first but does a more thorough job of identifying the objects constructed using the inner detector tracks (e.g. electron, muons, etc.). The new single node running allows for the two stages of the trigger to share the data preparation so detector information only needs to be read out once. Additionally, a single data format is used by both stages. The seeding of the precision tracking from the fast track finder eliminates the need to repeat the time-consuming pattern finding stage of the trigger algorithm.

3.3 Performance on First Data

The trigger underwent drastic improvement between Run 1 and Run 2 so it was essential the new trigger was commissioned and tested. The performance of the

---

[1]Hit data are silicon hits in the pixel and strip detectors, plus hits in the Transition Radiation Tracker.

triggers was assessed with 13 TeV data collected in July 2015 by the ATLAS detector. This data was collected using dedicated performance triggers which selected events regardless of results from the inner detector trigger processing. Efficiencies, residuals and resolutions are calculated relative to the tracks found by the offline reconstruction software. As such the efficiencies can be given by

$$\epsilon = \frac{N_{\mathrm{trigger}}}{N_{\mathrm{offline}}},\tag{3.1}$$

where $N_{\mathrm{trigger\,(offline)}}$ is the number of leptons reconstructed by the trigger (offline) algorithms.

Only good quality offline tracks with at least 2 pixel clusters and 6 silicon strip clusters are used, the tracks are also required to be in the region corresponding to the inner detector acceptance (with absolute pseudorapidity measured offline less than 2.5). The comparison between the trigger and offline tracks is done by associating the tracks to the closest track in (η, ϕ) space up to a maximum separation of $\Delta R = \sqrt{(\Delta\phi)^2 + (\Delta\eta)^2} = 0.05$.

3.3.1 Muons

The performance of the muon trigger at correctly selecting muon candidates with a minimum transverse momentum of 10 GeV is presented. Due to the 10 GeV threshold on the muon transverse momentum, the same requirement is applied to the offline tracks.

The efficiency of the HLT inner detector tracking algorithms on these events can be seen in the plots in Figure 3.2 as a function of the transverse momentum and the pseudorapidity. Track reconstruction efficiencies are found to be high across the full range, with no dependency on either of these track parameters.

The resolution of muons found with the HLT inner detector tracking algorithms has also been investigated both for the track pseudorapidity and the transverse impact parameter[2] as a function of pseudorapidity. These resolutions can be seen in Figure 3.3. The resolutions are very good over the full range of pseudorapidity. For both parameters the resolution is best at low absolute pseudorapidity, this is caused by the geometric limitations of the detector as the pseudorapidity increases. The

---

[2] The transverse impact parameter (d_0) is defined as the distance of closest approach in r-ϕ space.
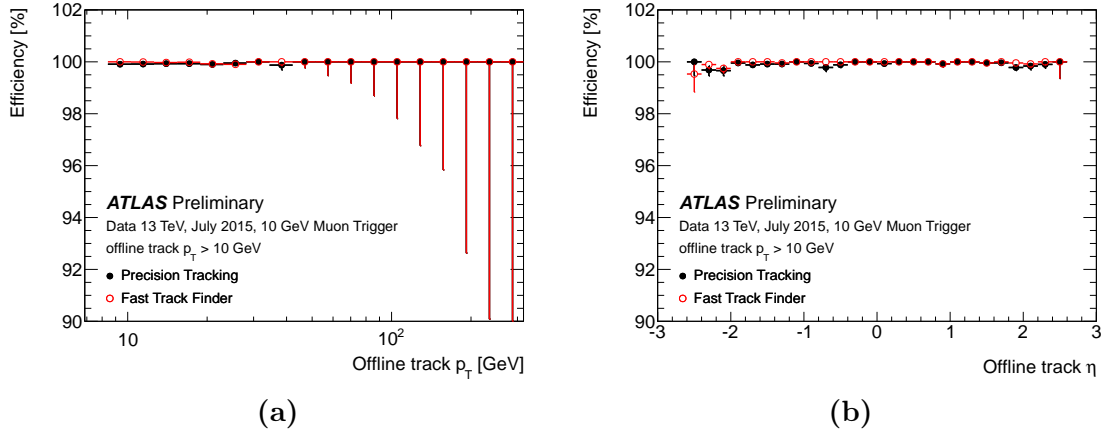
Figure 3.2: The efficiency of the HLT inner detector tracking algorithms for a 10 GeV muon trigger with respect to the offline track reconstruction as a function of (a) the transverse momentum and (b) the pseudorapidity (from [6]).
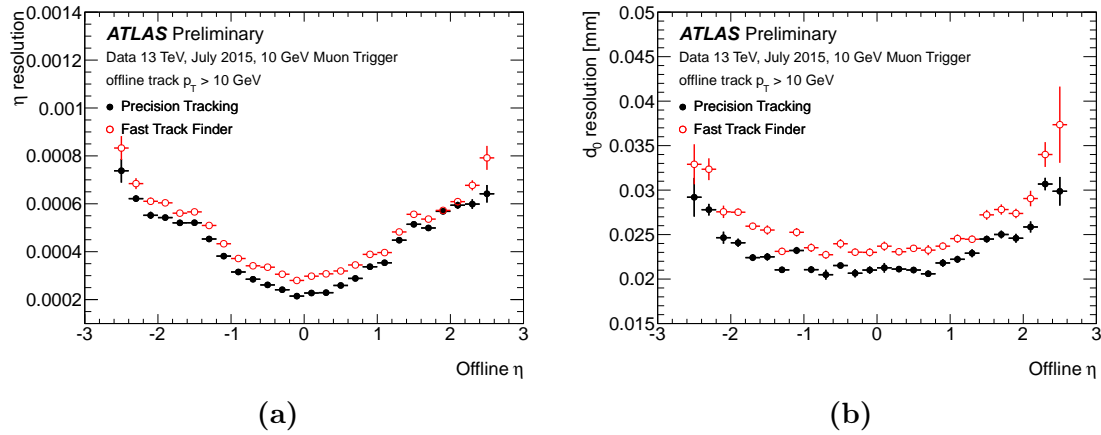
Figure 3.3: The resolution of (a) the pseudorapidity and (b) the transverse impact parameter of muons found with the HLT inner detector tracking algorithms for a 10 GeV muon trigger with respect to those found with the offline track reconstruction as a function of pseudorapidity (from [6]).

precision tracking stage of the trigger consistently improves the resolution over these parameters with respect to the fast track finder, as expected.

3.3.2 Electrons

When considering the performance of the electron triggers it is important to consider the difference in detecting electrons as opposed to muons. In Figure 3.4 the inverse transverse momentum residuals can be seen for both an electron and muon trigger. The inverse transverse momentum is used to measure the accuracy of momentum
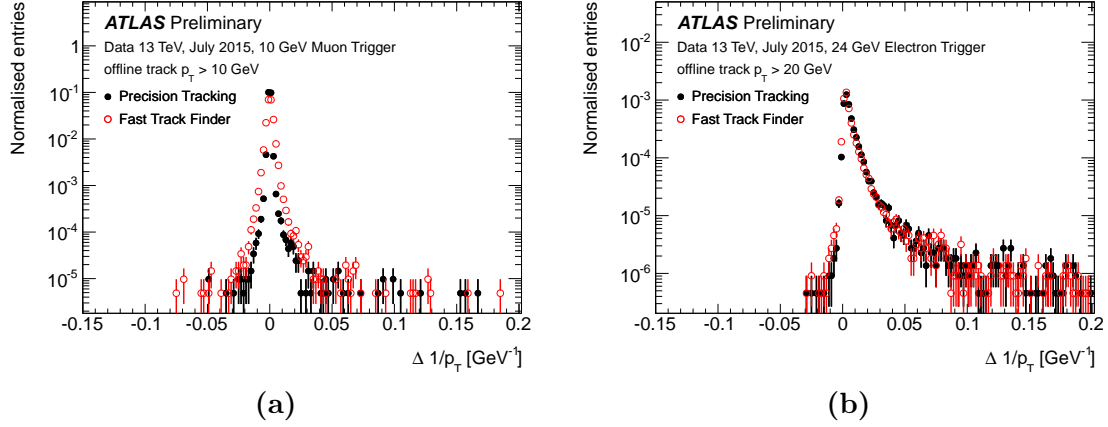
Figure 3.4: The inverse transverse momentum residuals for (a) muon trigger and (b) electron trigger with respect to the offline track reconstruction (from [6]).

measurement as momentum is measured by considering the curvature of the track and this is proportional to the inverse transverse momentum. In the muon case the distribution is nearly symmetrical with a narrow width. As with the resolutions for muons, the precision tracking has clearly improved resolution with a narrower width than the fast track finder. In the electron case this effect is less clear due to the larger spread in the difference in momentum. The spread for the electron trigger is very asymmetric with a large positive tail due to energy loss from the electrons undergoing bremsstrahlung in flight. This spread leads to a reduction in performance when compared to the muon trigger. In the full offline reconstruction there are more sophisticated corrections to account for this energy loss which are too slow to use in the trigger.

The performance of the electron trigger is studied using the same data as for the muon trigger but with a different selection. The chosen electron trigger has a threshold of 24 GeV for the transverse momentum of the electron, while the offline tracks are required to have a transverse momentum of at least 20 GeV.

The efficiencies for the HLT inner detector tracking algorithms run in this trigger can be seen in Figure 3.5 for the transverse momentum and the pseudorapidity. As was expected from the limitations inherent when detecting electrons the average efficiency is slightly lower than it was for muons. The efficiency does however appear flat with respect to transverse momentum. There is a small decrease in efficiency at large $|\eta|$, but it remains above 99% for the full range of tracks observed.
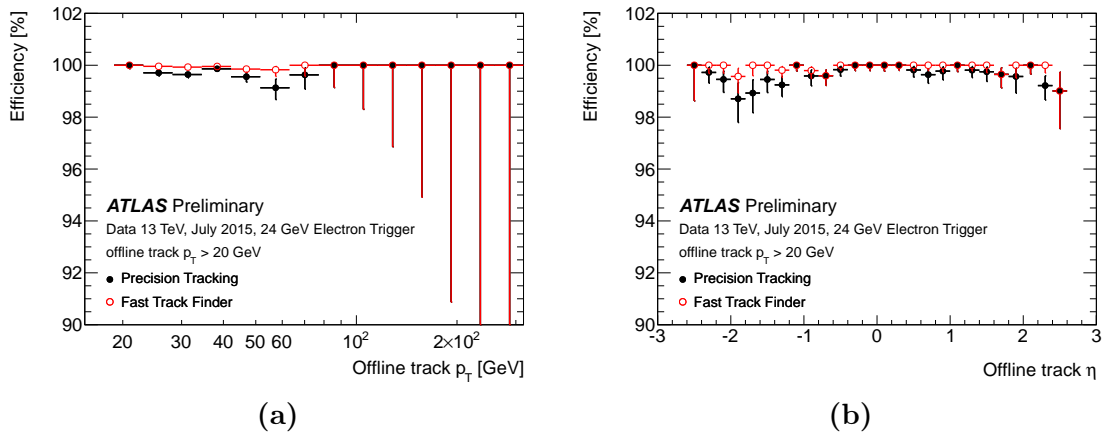
Figure 3.5: The efficiency of the HLT inner detector tracking algorithms for a 24 GeV electron trigger with respect to the offline track reconstruction as a function of (a) the transverse momentum and (b) the pseudorapidity (from [6]).

Chapter 4

Event Simulation and Object Reconstruction

This chapter describes the way in which events are simulated to provide theoretical predictions of the signals in the detector for a given process and the way ATLAS reconstructs objects from the signals in the detector. The simulation technology described in Section 4.1 is used extensively in the work presented in this thesis with the studies presented in Chapter 6 entirely being based on the simulation and the fit in Chapter 5 depending on high quality simulation being available. Then the reconstruction of the different objects that interact with the detector is described in Section 4.2, including the reconstruction of electrons, muons, jets and missing transverse energy along with the algorithms used to tag jets from b-quarks and the way objects sharing detector information is handled in this thesis.

4.1 Event Simulation

When conducting a search for new physical phenomena it is important to understand which events should be considered and to be able to identify if what is observed matches with our previous knowledge or if it is indicative of the new phenomena. Due to the complex nature of the Standard Model of particle physics, and the probabilistic nature of interaction of particles travelling through matter, it is not currently possible to derive analytical solutions for either the signature expected from a specific particle interaction or bulk distributions from many such interactions. In order then to get predictions of what is expected to be seen when conducting a search, simulations of

the particle interactions and the subsequent interactions of the resultant particles with matter are used. This simulation is carried out through the use of computer programs utilising Monte Carlo (MC) methods, the result being data that mirrors that collected by the experiment except with additional information on the theoretical process simulated simply known as MC data. Due to the large differences in the theories for different steps in the simulation it is broken up into two main processes run with different software tools chained together: the underlying event generation and the detector simulation.

4.1.1 Event Generation

Like overall MC data generation the event generation covers physics that is best described by different models, in this instance the differentiating factor is the energy scale at which the process happens. Due to the running of the strong coupling constant QCD can only be considered perturbative at large energy scales. This means the same algorithm is not appropriate to simulate both the high and low energy regimes so two different strategies are used for simulation.

First, the large energy scale process (also known as the hard scatter) is simulated. As high energy protons are made up of a large number of quarks and gluons it is necessary to identify which of these particles interact in the hard scatter. The relative abundance of the constituent particles and their share of the proton's energy is encoded in the parton density function (PDF), which is used to generate the colliding partons. The interaction between the colliding partons is simulated using a matrix element which is calculated to a fixed order in perturbation theory and provides the transition to the particles that enter into the low energy scale part of the simulation.

After the hard scatter is simulated any resultant partons with an energy more than a few GeV are decayed in what is known as the parton shower. The parton shower is used to simulate QCD interactions at a lower energy scale such that perturbative QCD no longer applies. It uses splitting probabilities to allow successive emission of quarks and gluons from both initial[1] and final state partons until the final state partons have an energy of ≈ 1 GeV at which hadronisation occurs. This splitting helps account for higher order QCD effects neglected by the fixed order calculation of the matrix element used in the hard scatter. It is only an approximation of what would be achieved if the

---

[1] When initial state partons decay in the parton shower the PDF has to be used to correct for the change in the decaying colliding parton.

calculation were performed at all orders as it assumes subsequent parton emissions are independent and does not account for additional virtual corrections.

The nature of QCD means that it is not physically possible to have free coloured particles. As such, at this stage of the simulation the remaining coloured particles need to be combined into bound states which are colour singlets. This is done through a process known as hadronisation, in which the quarks are grouped into mesons and baryons. Hadronisation is modelled through phenomenological models such as the cluster model [36] and the Lund string model [37]. There is then a further step in which short lived hadrons that would not survive to interact with the detector are decayed. The result is the collection of particles that will propagate into the detector. The next stage of the simulation covering this interaction is handled by the detector simulation.

This single hard scatter event is not the complete source of particles seen by the detector. The propagation of the remnants of the colliding protons, known as the underlying event, needs to be simulated and in a typical collision in the ATLAS detector multiple proton-proton interactions occur in the same bunch crossing (known as in-time pileup) which also need to be simulated. The underlying event also happens at small energy scales so cannot be modelled with perturbative QCD. Instead, phenomenological models are used to simulate this and the parameters are tuned with experimental data. The pileup events can be separately simulated and overlaid on the hard scatter event between the event generation and the detector simulation.

4.1.2 Detector Simulation

The detector simulation receives the resultant particles from the interaction that are long lived enough to reach the detector. It then propagates them through the detector simulating the interactions of the particles with the detector and the energy deposited in the detector as would be measured by the instrumentation. This simulation requires an exhaustive description of the entire detector including all the material making up the support and service infrastructure along with the active material. The software that performs this simulation is called GEANT4 [38–40] and the precision of its output has been validated and calibrated continuously through the detector operation. The output of this simulation is stored in an identical format to the processed data from the detector such that it can be further processed with the same reconstruction software to ensure consistency between the data and the MC.

The simulation of the detector is very costly in terms of CPU time with an average $t\bar{t}$ event taking 1990 s to simulate[2]. For comparison the average generation time for the event is 0.226 s and the average digitisation and reconstruction time is 76.5 s. The search conducted in this thesis is optimised for a small portion of the total $t\bar{t}$ production cross section. This means a large number of generated events are required to understand the process (millions of MC events are used). It is too costly for all the events used in the analysis to be simulated in this manner. A faster but less realistic simulation is used for some samples used to describe the uncertainty on the prediction as is explained in Section 5.7 called ATLFAST-II (AFII) [42]. AFII uses the same simulation as the full simulation for the inner detector and muon spectrometer. However, instead of fully simulating the propagation of particles in the calorimeters it simulates the energy deposited directly by using parametrizations of the energy profile. This is done separately in the direction of the particle's direction of travel and perpendicularly to it, taking into account the distributions of active and passive material in the calorimeter. This optimisation leads to a $20\times$ speed-up in simulation with an average running time for a $t\bar{t}$ event taking only 101 s.

4.2 Object Reconstruction

Any given physics process can be categorised by the particles resultant from the hard scatter. It is useful when searching for a specific process to identify events likely to have produced these particles in the hard scatter. It is not possible to directly detect all these particles with the ATLAS detector but each leaves a signature in the detector from which the presence of the particles can be inferred. The signatures of these particles are collections of signals from multiple parts of the detector. In the reconstruction software in ATLAS these signatures are searched for and if found are saved as objects for later analysis. The objects identified are: photon, electrons, muons, taus, jets and missing transverse energy. The search conducted in this thesis does not consider photons and taus[3] so their reconstruction will be omitted.

Broadly speaking all the reconstructed objects are made up of tracks and/or calorimeter clusters. All the objects use the same tracking techniques for the inner

---

[2]Timings are done normalising for processor speed so times are representative and should only be used to comparison between times not for the absolute value, see reference [41] for details.

[3]There is a tau veto applied in the selection to prevent overlap with a complimentary search but this is not optimised as part of this search so will not be covered in detail.

detector which is explained in Section 4.2.1. This section is based on information in [43], which contains further information on the tracking. Within this section the vertex finding is also explained because it is only dependent on the inner detector tracking, more detailed information can be found in [44]. Since calorimeter clusters are formed in different ways for the different objects they will be described for each object's reconstruction. First the reconstruction of the electrons, which are made of a single inner detector track connected to a cluster in the electromagnetic calorimeter, is described in Section 4.2.2. A more detailed description of the electron reconstruction can be found in [45]. Next the muon reconstruction is described in Section 2.2.4. Muons are made of an inner detector track linked to a muon spectrometer track, more information can be found in [46]. After this the reconstruction of hadronic jets is detailed in Section 4.2.4. Jets are reconstructed from information in the full calorimeter and have tracks from the inner detector associated with them, more information on jet reconstruction can be found in [47] and [48]. The identification of jets that originate from b-hadrons is explained in Section 4.2.5, more details on this procedure can be found in [49] and [50]. Once these objects have been constructed the missing energy is built from the information in the other objects plus a correction term, this is detailed in Section 4.2.6. More information on the missing energy calculation in ATLAS can be found in [51]. Finally the process in which the removal of objects which originate from the same signals in the detector is described in Section 4.2.7.

4.2.1 Tracks and Vertices

While tracks do not make up analysis objects themselves, they form a crucial part of the identification of the vertices and the objects described in the rest of this section. A track describes the path of a charged particle and can be found by connecting the signals made by the charged particle in the detector. Tracks can be described by five parameters: $d_0, z_0, \phi, \theta, q/p$, where d_0 and z_0 are the transverse and longitudinal impact parameters[4] respectively, ϕ and θ are the azimuthal and polar angles, respectively and q/p is the charge of the particle divided by its momentum. For vertex finding tracks are made only with information from the inner detector (see Section 2.2.2). The track finding happens in three stages, an inside-out track reconstruction, an outside-in track

---

[4]An impact parameter is defined as the perpendicular distance between the track and the collision point in the given direction.

reconstruction and a pattern recognition stage which finds vertices and kink objects[5] and their associated tracks [43].

Inside-out tracking starts with a pre-processing step in which the raw data from the pixel and strip detectors in the inner detector are clustered into hits. The hits are defined by their location in the three space dimensions. Also in this step is the creation of drift circles in the TRT, which are used instead of hit points as the TRT does not provide any information about the location of the hit along the straw dimension. Next, track seeds, which are made up of three hits, are formed from the hits coming from the pixel detector and the first layer of the strip detector. The seeds are then extended through successive layers of the silicon detector, each time reassessing the predicted path of the track in the next layer. Tracks are then refit with a more accurate reconstruction geometry and material information. The χ^2/ndf from the fit and information such as if the track traverses layers of the detector without leaving a signal is combined to build a quality score for each track. The quality score is used to remove poor quality tracks and to assign hits that are associated with multiple tracks to the track with the highest score. The surviving tracks are then extended into the TRT detector to find compatible measurements in the TRT. Once associated the complete tracks are refit to find the final track parameters.

After inside-out tracking, a second tracking strategy is used to ensure no tracks are missed such as those from decays in flight. This second strategy is called outside-in tracking due to the seeds being formed from the drift circles found in the TRT. These seeds only consider drift circles not previously associated to tracks found from the first strategy. The seeds are then extrapolated back to the silicon detectors to form complete tracks. As with the first strategy, ambiguities caused by multiple tracks utilising the same signals in the detector are resolved and a complete track fit is performed to find the final track parameters. There also exist TRT only tracks for high quality drift circles which do not match up with corresponding hits in the silicon detector.

Once the tracks finding is complete all the tracks are used to identify the primary and secondary vertices. Primary vertices are the points at which proton-proton interactions occurred and secondary vertices are points at which displaced secondary decays occurred, such as the decay of b-quarks. A vertex is found by considering the maximum of the z_0 distribution of the tracks. An adaptive vertex fitting algorithm

---

[5]Objects which have sudden change in their direction caused by interactions with the detector or emission of radiation e.g. bremsstrahlung radiation

[44] is utilised to constrain the location of the vertex, which is restricted to the region in which the proton beams crossed. The compatibility of tracks with the vertex is then assessed and tracks that are incompatible with the candidate vertex by more than seven standard deviations are used to form new vertices using the same procedure until all tracks are associated with vertices. Any vertex with fewer than two associated tracks is discarded.

Due to the high luminosity delivered by the LHC there are typically multiple primary vertices in a single bunch crossing. It is unlikely that more than one collision of interest occurs in a single crossing due to the low cross section of processes of interest compared to the total collision cross section. It is therefore important to identify the primary vertex associated with the hard scatter, assumed to be the vertex with the largest sum of squared transverse momenta of its associated tracks. From this point forward this vertex will simply be referred to as the primary vertex and all other primary vertices will be referred to as pile-up vertices.

4.2.2 Electrons

Electrons are charged objects that interact electromagnetically, so it is expected that their signature in the detector would be a track in the inner detector that leads to an energy deposit in the electromagnetic calorimeter with an energy equivalent to the track's momentum. The reconstruction is complicated by the electron's small mass which means they experience large energy losses in flight caused by bremsstrahlung radiation. This radiation leads to an increased error in measuring their momentum and an increased complexity in reconstructing their tracks.

As reconstructed electrons are made up of both a calorimeter deposit and an inner detector track there are a number of steps involved in their reconstruction. First the electron object is seeded by clusters of energy in the electromagnetic calorimeter. These are found using sliding window algorithm with a 3×5 calorimeter cell window, corresponding to a 0.075×0.125 window in $\eta \times \phi$ space. Windows with a total transverse energy above 2.5 GeV are used to seed the clusters using a clustering algorithm that allows for duplicates to be removed. The kinematics of the final cluster are determined with an extended window, the size of which varies depending on where in the detector it is located.

Next, track reconstruction is performed. An overview of the standard track finding in ATLAS can be found in Section 4.2.1. In this standard track finding it is assumed that the tracks are caused by pions when correcting the track hypothesis with regards to energy loss and interactions with the detector. To compensate for the loss of efficiency this would cause for electron reconstruction a further step in the tracking is added. Track seeds which fail to be extended to full tracks with a transverse momentum greater than 1 GeV and are close to calorimeter clusters found in the previous step of electron reconstruction are reconsidered allowing for additional energy loss as would fit the electron hypothesis. The parameters for these tracks are determined by fitting them assuming an electron hypothesis. Tracks which were reconstructed using the standard track finding but failed the standard fit are also refit with the assumption that they are caused by an electron.

The reconstructed tracks and calorimeter clusters then need to be associated to build electron objects. Coincidence between the tracks and clusters is searched for by extending the tracks to the middle layer of the calorimeter, taking into account energy loss due to bremsstrahlung and comparing the predicted location in (η, ϕ) space with the centres of the clusters. Tracks with a large number of silicon hits are once more refit, taking into account the non-linear bremsstrahlung effects. In the case of ambiguity caused by multiple tracks connecting to a single cluster a primary track is selected by assessing the quality of each track and how closely the track matches the cluster.

Objects which are reconstructed in this way still need to pass requirements based on their quality. This is done in order to remove objects that are caused by background processes, such as hadronic jets and converted photons. These requirements have been combined into a single selection based on a multivariate likelihood, built from a collection of distinguishing criteria. These criteria use information on both the track and cluster including details of the shower shape, information about the transition radiation measured, and other quantities outlined in [45]. For each quantity, probability density functions are derived for both signal and background processes using simulated data. These are then combined into the discriminant $d_{\mathcal{L}}$ given by

$$d_{\mathcal{L}} = \frac{\mathcal{L}_S}{\mathcal{L}_S + \mathcal{L}_B}, \qquad \mathcal{L}_{S(B)}(\vec{x}) = \prod_{i=1}^{n} P_{s(b),i}(x_i), \qquad (4.1)$$

where x_i denotes a discriminating variable and $P_{s(b),i}(x_i)$ denotes the probability of the variable taking the measured value under the signal (background) hypothesis.
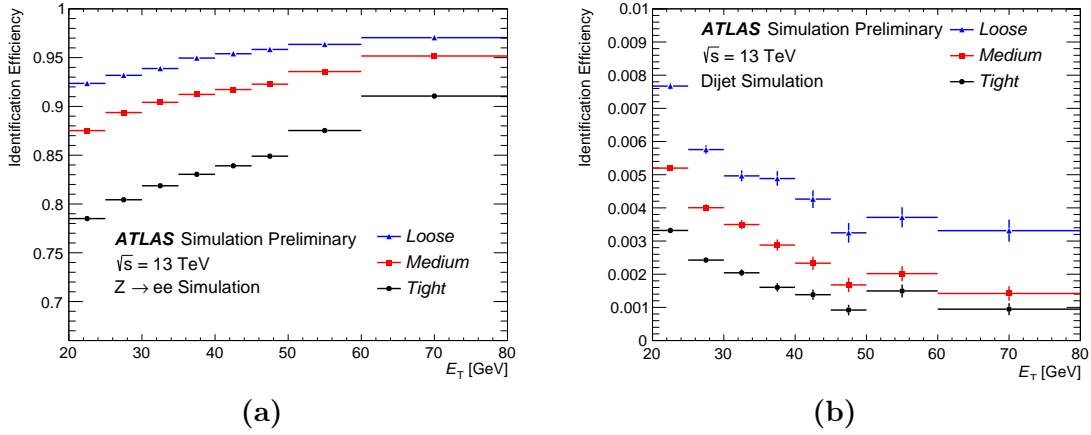
Figure 4.1: The efficiency of (a) electron identification calculated using Z → ee decays and (b) identification of hadrons as electrons calculated using dijet events. Both efficiencies are measured relative to reconstructed electrons and are obtained from Monte Carlo simulation. Only electrons matched to electrons in the truth record are used to measure the selection efficiency and objects matched to electrons are vetoed in the rejection efficiency. A jump in efficiency can be observed in the 50 GeV bin due to the previous bin being the last used to optimised the identification (from [45]).

Three operating points defined by different selection values of the likelihood distribution are defined. For each working point the identification efficiency and background rejection are verified as can be seen in Figure 4.1. For the analysis presented in this thesis the tight working point was used for which it can be seen an identification efficiency of over 80% and background rejection over 99.7% is achieved for electrons with transverse energy greater than 25 GeV.

4.2.3 Muons

Muons are massive charged particles. Due to their large mass they produce far lower amounts of bremsstrahlung radiation than electrons and as such have far lower energy loss while traversing the detector. Muons are expected to pass straight through the inner detector and calorimeter into the muon spectrometer. The calorimeter is designed to contain the showers of the other particles[6], however, some highly energetic particles can punch through the calorimeter and produce a signal in the muon spectrometer that can fake a muon.

---

[6]Excluding particles that only interact weakly like neutrinos in the Standard Model.

In order to reconstruct a muon, tracks are reconstructed separately in the inner detector and muon spectrometer and then later combined. The tracking used in the inner detector is the standard ATLAS tracking algorithm described in Section 4.2.1. In the muon spectrometer the tracking commences with track segment finding in the TGC, RPC and MDT subsystems through a road search using a Hough transform. Separately track segments are identified in the CSC subsystem through a combinatorial search in the η and ϕ detector planes in which clusters in the different CSC layers are combined and then fit with a constraint from the interaction point and combinations with a good fit are used as track segments.

These track segments are then combined into track candidates through a combinatorial search. Three steps are performed to reduce the possible combinations of track segments. First, super segments are constructed from segments in adjacent sectors that are consistent with being part of the same track. Next, all the track segments are ranked in terms of their quality and those with the highest quality are used as seeds for the track finding. Finally, the combinatorics are reduced by splitting the search into three regions: the barrel, endcap and overlap regions. The search starts with the seeds in the central layer before proceeding to those in the outer and then inner layers. Once track candidates have been formed, overlap removal is performed. During this process, to allow tracking of closely produced muons, multiple high quality track candidates that are well separated in at least one of the layers are allowed to share track segments. Finally, an overall track fit is performed to measure the track properties. During this process outlying hits can be removed and missed hits can be incorporated.

Once the tracking is complete in both the inner detector and the muon spectrometer then muon objects are constructed. The muon objects used in the studies in this thesis can be separated into two categories determined by which parts of the detector are used for reconstruction. Firstly there are combined muons, which are formed from the combination of aligning tracks in the inner detector and the muon spectrometer. The majority ($\approx 99.5\%$) of combined muons are formed using an outside-in extrapolation but inside-out extrapolation is also applied to ensure no loss in efficiency. Once the tracks are associated, a global fit is once more performed. At this step hits in the muon spectrometer can again be added or removed from the muon object.

The second type is the extrapolated muon for which there is only a track in the muon spectrometer. This type of muon is used to increase the acceptance region of muons from an η of 2.5 to 2.7, beyond the acceptance of the inner detector. These

muons are required to traverse three layers of the muon spectrometer. If a muon's spectrometer track is shared with a combined muon then preference is given to the muon with the best fit quality and number of hits used in the reconstruction.

In order for the reconstructed muons to be considered for the analysis they also have to satisfy some quality criteria. These criteria include a minimum number of hits in the various subdetectors, a maximum number of layers of the detector the muon traverses without producing a signal, any imbalance in the track charge and momentum in the inner detector and muon spectrometer and the quality of the global track fit. These identification criteria are chosen to minimise the systematic uncertainties associated with muon reconstruction and calibration.

This reconstruction has been validated using $t\bar{t}$ Monte Carlo ensuring prompt decays of W bosons are correctly reconstructed and decays of light hadrons are excluded. An efficiency of reconstructing the prompt muons was 95.5% for low transverse momentum muons[7] and 96.1% for high transverse momentum muons, and the light hadron rejection was 99.62% and 99.83% for low and high transverse momentum muons respectively [46]. This has also been validated with data using J/ψ and Z decays for the low and high momentum muons respectively, as can be seen in Figure 4.2. It can be seen that the efficiency is almost constant over a large range of transverse momentum and is very high throughout the range. The discrepancy between the data and the Monte Carlo prediction is used to correct the Monte Carlo samples used in this thesis, with the full error associated with this correction shown in the bottom plot.

4.2.4 Jets

As was described in Section 4.1.1 high energy partons which result from a hard scattering process undergo many decays resulting in a collection of collimated particles carrying the momentum of the original parton. The resultant particles undergo hadronisation leading to the hadrons which go on to interact with the detector. The distribution of energy carried by the different types of particles can be seen in Figure 4.3. As can be seen a large fraction of the energy in a jet is carried by charged particles which leave tracks in the inner detector before depositing their energy in the electromagnetic calorimeter. There are also photons and neutral hadrons which leave

---

[7]In this measurement low transverse momentum means $4 < p_T < 20$ GeV and high transverse momentum means $20 < p_T < 100$ GeV
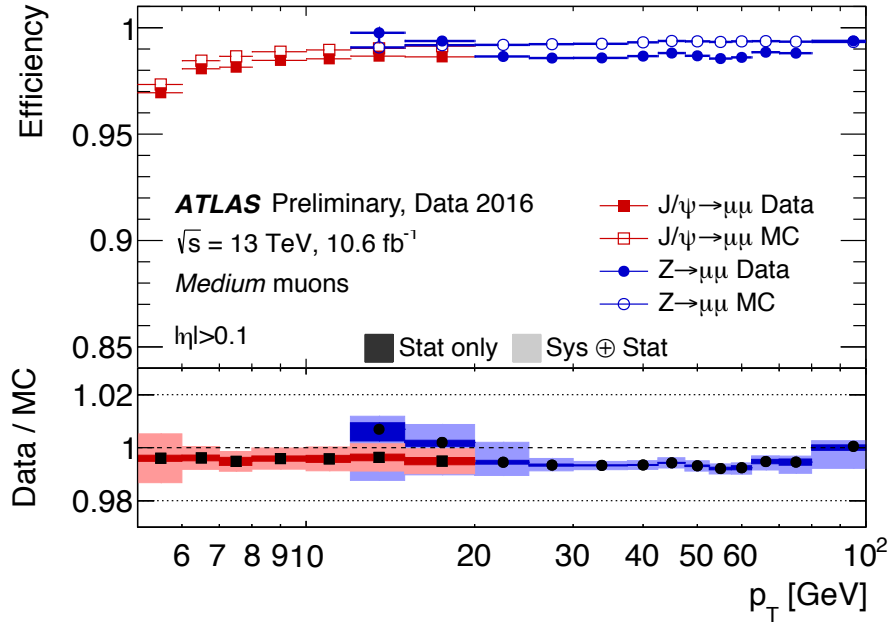
Figure 4.2: The efficiency of muon identification calculated using $Z \to \mu\mu$ and $J/\psi \to \mu\mu$ decays as a function of muon momentum. Prediction from Monte Carlo simulation is shown using hollow markers with data shown using solid markers. The top panel shows statistical errors only, whereas in the bottom panel the darker bands indicate statistical error and the lighter bands represent the total uncertainty. The values in the bottom panel represent the scale factors applied to Monte Carlo data to correct it to observation (from [52]).
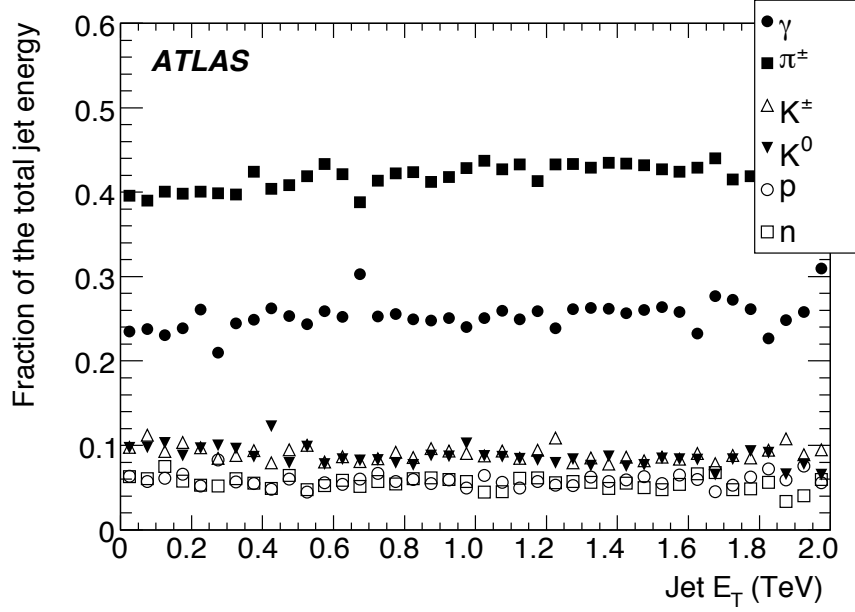
Figure 4.3: The fractional energy carried by the particle types found within a jet (from [53]).

only a signal in the calorimeters, both the electromagnetic calorimeter in the case of photons and the hadronic calorimeter in the case of neutral hadrons. This means a typical jet signature will be a collection of tracks leading to a deposit in both the electromagnetic and hadronic calorimeters.

Jets in the ATLAS detector are found by considering the signal in the calorimeters. In order to reduce noise from the calorimeters the calorimeter signal is not directly used but compound objects called topological clusters (topo-clusters) [54, 55] are used in jet finding. Topological clusters are three-dimensional irregularly shaped groups of calorimeter cells which have a high signal relative to the expected noise of the cells. They are designed to produce clusters that follow the shower development of particles, taking advantage of the fine segmentation of the ATLAS detector.

The noise (N) is defined as the root-mean-square of the energy distribution in the cell for randomly triggered events in which no collision takes place, combined with the expected noise from pile-up for the given luminosity. As such cells with a high relative signal are identified using the variable S/N, the number of standard deviations away the expected background the measurement falls assuming normally distributed noise.

Topo-clusters are initially made in three steps: first a seed cell is selected with $S/N > t_{\text{seed}}$, then adjacent cells with $S/N > t_{\text{neighbour}}$ are added to the cluster

iteratively, finally all adjacent cells to those found in the previous two steps are added when they have $S/N > t_{\text{cell}}$. Typically the three threshold values are set to: $t_{\text{seed}} = 4$, $t_{\text{neighbour}} = 2$ and $t_{\text{cell}} = 0$ but can be varied to change the efficiency of reconstruction and fake rate. This clustering can suffer from very large clusters forming in the detector for events with a very large energy deposit in the calorimeter. In order to prevent this a cluster splitting algorithm has been implemented which acts on the clusters formed in the previous steps. This searches for local maxima within the clusters defined by a cell with an energy measurement greater than 500 MeV and that of its neighbouring cells and with the number of neighbouring cells also within the cluster above some threshold (typically set to four). These local maxima are then used to split the cluster by iteratively adding all neighbouring cells to each sub-cluster which were also in the parent cluster in descending order of sub-cluster energy[8]. The sub-clusters along with any clusters without local maxima make up the final list of topo-clusters, which are defined with energy equal to the sum of their constituent cells and direction equal to the weighted average of its cells.

Once the topo-clusters have been constructed then the jets can be made from clusters of topo-clusters. In order for this clustering to be easily comparable to theory and to ensure the method of clustering is not highly sensitive to higher orders in the perturbation theory used to calculate the QCD contributions it is necessary for the algorithm used to be infrared and collinear safe. An infrared safe algorithm is not sensitive to extra soft radiation from partons and a collinear safe algorithm is not sensitive to any parton being split into two partons travelling in the same direction. The clustering algorithm used in this thesis is known as the anti-k_t algorithm [56] and it is one of a set of sequential recombination algorithms characterised by the distances defined as

$$d_{ij} = \min\left(k_{ti}^{2p}, k_{tj}^{2p}\right) \frac{\Delta_{ij}^2}{R^2}$$

$$d_{iB} = k_{ti}^{2p},$$

(4.2)

where $\Delta_{ij}^2 = (y_i - y_j)^2 - (\phi_i - \phi_j)^2$ and k_{ti}, y_i and ϕ_i are the transverse momentum, rapidity and azimuth of an entity i being clustered respectively. R is the jet radius parameter which suppresses large jet formation; a value of 0.4 is used for all jets used in this thesis. p is the parameter which defines the algorithm in the set; for the anti-k_t

---

[8] Cells assigned to more than one sub-cluster during the same iteration are shared by the two sub-clusters with its energy split between them
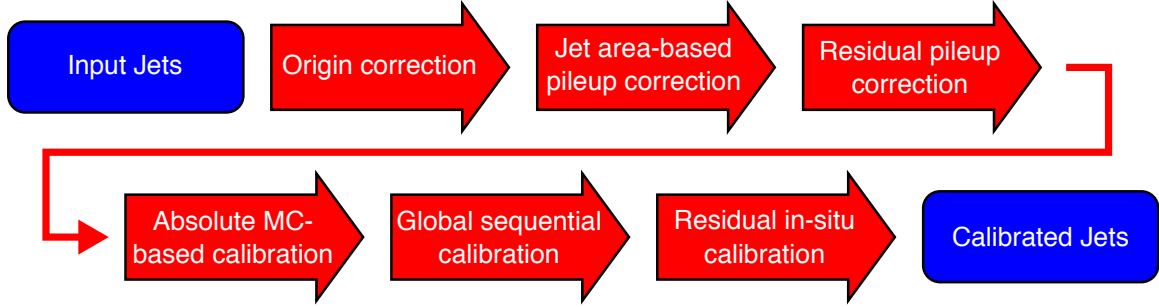
Figure 4.4: The steps taken to correct and calibrate reconstructed jets in ATLAS as detailed in [47].

algorithm this is set to -1. The anti-k_t algorithm is desirable as it produces cone-like jets for highly energetic isolated objects and is very resilient to soft radiation around the jet boundary.

Due to inefficiencies in measurement and the need to correct for factors such as pile-up, a series of corrections are applied to the reconstructed jets. The series of corrections that is applied to the jets is summarised in Figure 4.4. The first correction applied is the origin correction. When the jet object is constructed the direction of the jet is determined by the weighted average of the cells in the jet then finding the direction of that centre from the centre of the detector. The correction updates the assumption that the jet originates in the centre of the detector to the jet originating at the primary vertex of the event. The energy is unchanged in this correction. This correction significantly improves the resolution in η, with a $\approx 25\%$ improvement at low transverse momentum and up to $\approx 80\%$ improvement for high transverse momentum jets.

The next two corrections are in order to correct for pile-up effects, summarised as

$$p_{\mathrm{T}}^{\mathrm{corr}} = p_{\mathrm{T}} - \rho A - \alpha(p_{\mathrm{T}}, \eta) \left(N_{\mathrm{PV}} - 1 \right) - \beta(p_{\mathrm{T}}, \eta)\mu. \tag{4.3}$$

The first, given by the first correction term in the equation (ρA), subtracts pile-up effects utilising the jet area [57] to quantify the subtraction. The area of the jet is calculated by randomly inserting ghost tracks[9] uniformly across the detector volume and finding the number within the area of the reconstructed jet. This quantity is then multiplied by the pile-up energy density ρ, calculated by taking the median jet density of all the jets reconstructed in the central region ($|\eta| < 2.0$) of the detector, to

---

[9]Tracks with infinitesimal transverse momentum

give the correction. The pile-up energy density is calculated only in the centre of the detector to increase the sensitivity to soft radiation that is characteristic of that from pile-up events.

After this area based correction is applied it is observed that the measured jet transverse momentum is still dependent on pile-up so a further residual correction is applied. This correction, unlike the previous pile-up correction, is derived from Monte Carlo data by taking the difference between the reconstructed jet transverse momentum and that from matched truth jets[10]. It is described by the last two terms in Equation (4.3): the first term has a dependence on the number of primary vertices in the event (N_{PV}) in order to correct for in-time pile-up[11], whereas the second term has a dependence on the average number of primary vertices for an event (μ) in order to correct for the out-of-time pile-up[12]. The factors $\alpha(p_T, \eta)$ and $\beta(p_T, \eta)$ are found to be relatively independent and have a linear dependence on the transverse momentum of the jet and so are derived from a linear fit. The size of the pile-up corrections can be seen in Figure 4.5.

The next correction applied corrects the energy and pseudorapidity of the jets to that of truth jets. Here truth jets need to be matched such that the distance in (η, ϕ) space is less than 0.3 from the reconstructed jet, and to avoid ambiguities no other reconstructed jet can be within a distance of 1.0 and no other truth jets can be in a distance of 0.6 in (η, ϕ) from the reconstructed jet. The correction is calculated in bins of the energy of the truth jet and the uncorrected pseudorapidity of the reconstructed jet. The value is determined as the mean of a Gaussian fit to the distribution of the ratio of reconstructed jet's energy to the truth jet's energy. This correction leaves a residual bias in pseudorapidity due to jets overlapping areas of the detector where there are changes in calorimeter geometry or technology. This bias is also corrected as part of this step using Monte Carlo simulation.

The global sequential calibration step covers five corrections applied to the jets sequentially due to bias observed in a series of variables that are found to be independent

---

[10]Truth jets are jets clustered from the particles from the parton shower which have a lifetime greater than 30 ps, excluding muons and neutrinos. These are matched to reconstructed jets if the distance between them in η, ϕ space is less than the radius parameter used for the jet clustering.

[11]Energy in the calorimeter from other proton-proton collisions that occur during the same bunch crossing as the event.

[12]Energy in the calorimeter from other proton-proton collisions that occur during different bunch crossing to the event, typically those either side.
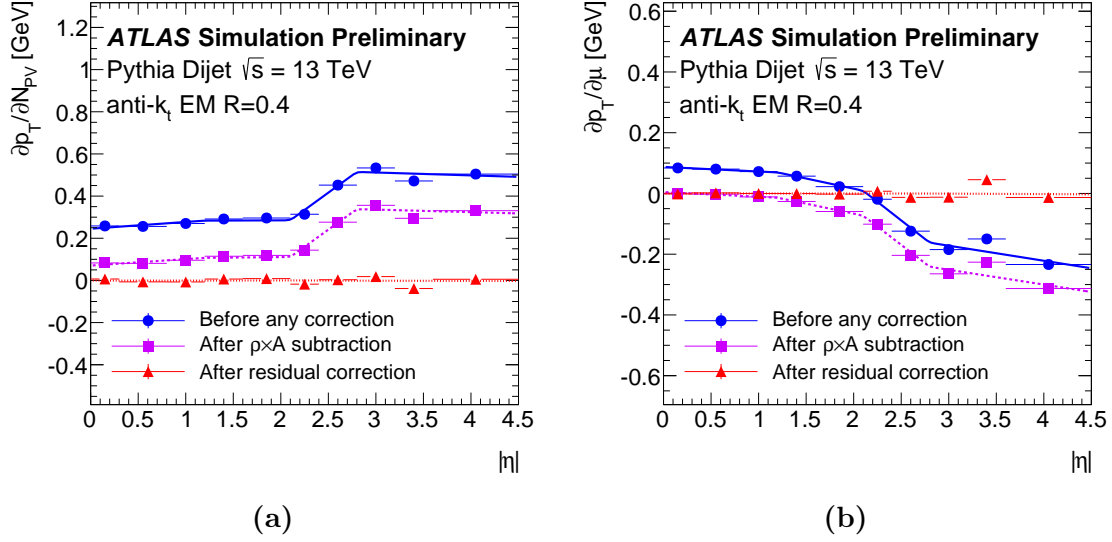
Figure 4.5: The dependence of jet transverse momentum on (a) in-time pile-up, (b) out-of-time pile-up as a function of the absolute value of the jet's pseudorapidity (from [48]).

of each other. The five variables that are used to derive correction in order of the correction being applied are:

1. the fraction of the jet energy deposited in the first layer of the tile calorimeter,

2. the fraction of the jet energy deposited in the third layer of the electromagnetic liquid argon calorimeter,

3. the number of tracks with transverse momentum greater than 1 GeV associated with the jet,

4. the width of the jet calculated with the tracks used in the previous correction, calculated weighted by the transverse momentum of the tracks,

5. the number of muon segments associated with the jet.

Finally, the jets are corrected with an in-situ calibration in order to compensate for limitations in the description of the detector used in the Monte Carlo simulation and any other limitations of the simulation. These corrections are derived by balancing the transverse momentum of well measured objects with jets. In the first correction the different sections of the calorimeter are calibrated to each other by balancing a dijet event. One of the jets in the event is in the central region and the other in the forward region. The correction is performed up to a jet transverse momentum of 1.2 TeV. Next

either a well measured photon or leptonically[13] decaying Z-boson is balanced against a recoiling jet in the central region, this is performed up to a transverse momentum of 944 GeV. Finally a multijet correction is applied in which a high transverse momentum jet $(300 < p_T < 2000 \text{ GeV})$ recoils off several low transverse momentum jets in the central region.

Once the properly reconstructed and calibrated jets have been found it is important to attempt to distinguish those jets from the hard scattering process and those from pile-up interactions. To achieve this a selection on the Jet Vertex Tagger (JVT) [58] has been employed. The JVT is a multivariate technique that uses various track based variables in order to distinguish pile-up jets from those from the hard scatter. A selection based on the JVT variable leads to stable efficiency in the correctly identifying jets from the hard scatter with variable numbers of in-time pile-up events reducing their effect on the analysis.

4.2.5 b-tagging

The analysis presented in this thesis is optimised for a final state containing a number of high energy b-quarks. These b-quarks will hadronise into b-hadrons which will decay in the detector producing a collimated collection of particles being measured in a jet. Due to the high mass of b-quarks it takes a greater amount of energy to produce them than lighter quarks such as charm, up, and down quarks, leading to a greater number of these lighter jets being produced. These lighter jets compromise a large proportion of the background for the analysis making it vital that they can be optimally distinguished in order to get the highest signal purity in the search and the best chance of discovering the process of interest. In order to distinguish jets which originate from b-hadrons in the ATLAS detector a multivariate classifier has been developed [49, 50]. As input to this classifier three classes of algorithm are used in order to distinguish b-quarks targeting information on the impact parameters from tracks, secondary vertex reconstruction and decay chain multi-vertex reconstruction.

Impact Parameter Algorithms

The first class of algorithm utilises information on the impact parameters of the tracks, the two algorithms of this type are called IP2D and IP3D. The IPxD algorithms take

---

[13]excluding tau leptons and neutrinos

advantage of the long lifetime of b-baryons caused by the Cabibbo suppression (see Section 1.1.1) on the decay of the b-quark. This suppression leads to a lifetime of ~ 1.5 ps, which for energetic baryons (those with a transverse momentum > 10 GeV) gives a flight path length $\mathcal{O}(\text{mm})$. The subsequent decay of the b-hadron produces a collection of particles originating from a point displaced form the primary interaction vertex. The tracks coming from this vertex will on average have a large distance of closest approach to the primary vertex than ones coming directly from this vertex, this distance is what is used in the IPxD algorithms.

The distance of closest approach is used parametrised as the transverse and longitudinal impact parameters. The transverse impact parameter (d_0) is defined as the distance of closest approach in r-ϕ space and the longitudinal impact parameter ($z_o \sin \theta$) is the distance in the longitudinal plane calculated at the same location as the transverse impact parameter. Along with the expected magnitude of the impact parameter being different for particles from the decay of b-hadrons the sign is also expected to be such that the secondary vertex is in front of the primary vertex relative to the jet's direction.

The likelihood of each track coming from a b-, c- or light-jet[14] is determined by using the distribution of the impact parameter significances[15] in Monte Carlo data in events with a pair of top quarks. This procedure is performed in a collection of categories, each treated separately, defined by the number of hits in the various layers of the tracker. For the IP2D tagger these likelihoods are derived using just the transverse impact parameter significance, whereas the IP3D tagger uses a two dimensional distribution of the two impact parameters ensuring correlations are accounted for.

The IPxD discriminants are then defined by the sum of the log-likelihood ratios of all the tracks within a given jet. The ratio of the b-jet likelihood with respect to the c- and light- jet likelihoods are calculated separately generating two discriminants for each of the IPxD algorithms, targeted at discriminating between the two types of jet respectively. The distributions for the two algorithms trained with the logarithm of the light-jet likelihood in the denominator of the sum can be seen in Figure 4.6.

---

[14]Where light-jets are those that are caused by u, d or s quarks or gluons.

[15]The impact parameter significances are defined as d_0/σ_{d_0} and $z_o \sin \theta/\sigma_{z_o \sin \theta}$ for the transverse and longitudinal impact parameters respectively.
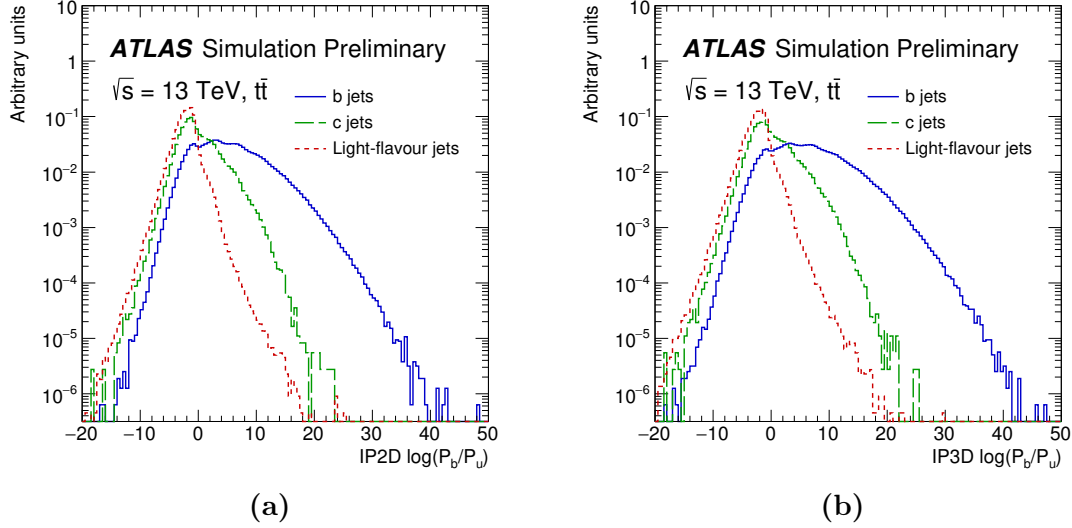
Figure 4.6: The distribution of the discriminants calculated using the (a) IP2D and (b) IP3D algorithms optimised against light-jets, showing the performance for b-, c- and light-jets separately (from [50]).

Secondary Vertex Finding Algorithm

The second algorithm used in b-tagging is the secondary vertex finding algorithm. In this algorithm a collection of secondary vertices is formed by considering all pairs of high quality tracks within the jet. The tracks considered are required to have a high number of hits in the tracker and have a good quality global track fit. In the case of high energy jets with a large number of tracks only the 25 highest transverse momentum tracks are considered. This is done to reduce the number of fake vertices and as a result of the high mass of b-hadrons preserves the majority of tracks of interest. Once all pairs of tracks are considered and only those pairs compatible with originating from a secondary vertex are retained any pairs which are likely to have originated from other long-lived particles (e.g. K_S^0 or Λ mesons), photon conversions or interactions with the detector material are removed.

These vertices are then fitted with all the tracks from the list of remaining vertices, removing the outlying tracks until a good quality fit is achieved. A number of properties of these new vertices are calculated and used in the later stages of b-tagging including the number of secondary vertices found, the reconstructed mass of the tracks in the secondary vertex, the distance between the secondary and primary vertices and others.

Decay Chain Multi-Vertex Algorithm

The decay chain multi-vertex algorithm is designed to find full weak decay paths of the b-hadrons to c-hadrons. This is achieved by searching for a common path of the b- and c-hadrons using the primary vertex, and the decay vertices of the two hadrons. To ensure no loss of efficiency decay vertices of the two hadrons are considered with only a single track emerging. Once such decay chains are found variables similar to those used from the secondary vertex finding algorithm are calculated for the decay chain in order to discriminate the jets originating from b-hadrons.

Multivariate Combination

The final discriminant used for the identification of jets originating from a b-hadron is done using a multivariate combination of variables derived using the three algorithms described above. The algorithm used to produce this classifier is a boosted decision tree and it is trained used Monte Carlo simulations of $t\bar{t}$ processes. The classifier is provided with jets associated with b-hadrons as a signal and jets associated with c-hadrons (7%) and light sources (93%) as background. Along with the variables from the three algorithms above the transverse momentum and pseudorapidity of the jets are provided in the training to allow the algorithm to exploit correlations between them and the other variables. In order to ensure these are not used directly for discrimination the jets associated with the b- and c hadrons are reweighted to have identical distributions in these two variables as the light jets. Finally any jets which fail all of the three algorithms above are given a weight of 10^{-6} to suppress their influence on the training procedure.

The distribution of discriminant shown for the three categories of jet considered in the training is shown in Figure 4.7. Clear separation is visible between the jets originating from a b-hadron and those from the other sources. It has not been possible in the study presented in this thesis to use this variable in the full continuous form due to difficulties in calibrating and validating the performance across the whole range of values. Instead a single working point is used such that jets with a value of the discriminant above a given value are considered to have originated from a b-hadron and those below the threshold are considered to be from other sources. The value chosen for use in this thesis is 0.8244 which corresponds to an efficiency in selecting jets from a b-hadron of 70%. This working point provides a rejection factor of 12 for
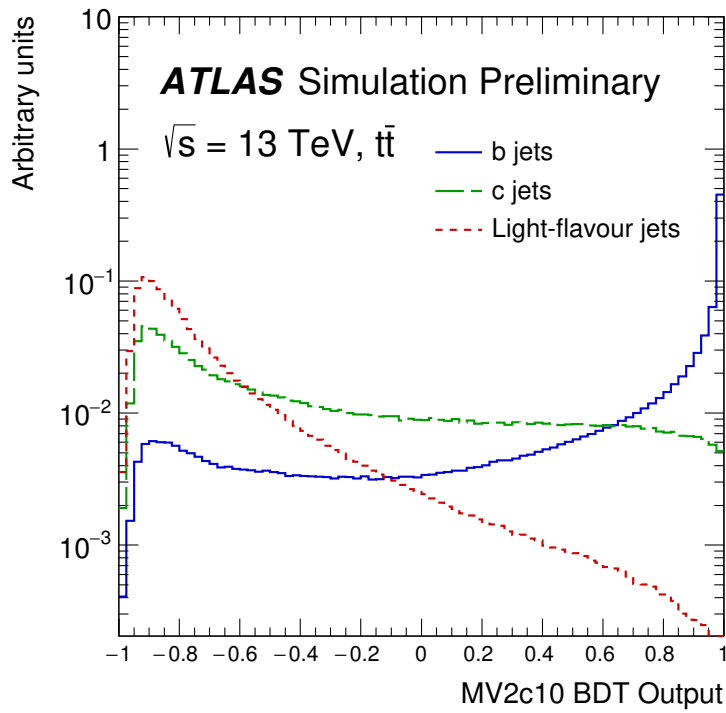
Figure 4.7: The distribution of the discriminant produced from the multivariate combination of the b-tagging algorithms for the different categories of jet. This output is known as MV2c10 as it is a MultiVariate algorithm with 7% of the background used in training comprising of c-jets (the name is kept from the legacy of using 10%) (from [50]).

jets originating from a c-hadron and a rejection factor of 381 for jets originating from light sources.

4.2.6 Missing Transverse Energy

The analysis presented in this thesis searches for a process in which it is expected that neutrinos will be created. Neutrinos only interact weakly and are as such not expected to interact with the detector so can not be observed directly. They can, however, be indirectly inferred through the consideration of missing transverse energy. Missing transverse energy ($E_{\mathrm{T}}^{\mathrm{miss}}$) is defined as equal in magnitude to the sum of transverse energy of the particles measured in an event but with a direction defined as opposite to the direction in which the particles are made, weighted by their energy. This definition is as a consequence of the conservation of momentum in physical systems. The colliding protons have negligible momentum in the transverse plane and as such the sum of the resultant particles of the collision must also have negligible transverse momentum, any mismatch being caused by particles which were not measured by the detector.

In ATLAS $E_{\mathrm{T}}^{\mathrm{miss}}$ is calculated through considering first the momentum of fully reconstructed and calibrated physics objects such as those discussed in the previous sections in this chapter and then a correction term to account for detector signals not associated to any reconstructed object [51]. This is summarised as

$$E_{x(y)}^{\mathrm{miss}} = E_{x(y)}^{\mathrm{miss,e}} + E_{x(y)}^{\mathrm{miss},\gamma} + E_{x(y)}^{\mathrm{miss},\tau} + E_{x(y)}^{\mathrm{miss,jets}} + E_{x(y)}^{\mathrm{miss},\mu} + E_{x(y)}^{\mathrm{miss,soft}}, \qquad (4.4)$$

where each term corresponds to the negative vectorial sum of the momenta of the objects considered in the $x(y)$ direction. The soft term ($E_{x(y)}^{\mathrm{miss,soft}}$) is calculated by considering tracks in the inner detector that are not associated with any of the objects in the previous terms but are consistent with the primary vertex of the collision.

4.2.7 Overlap Removal

Once all the objects are reconstructed as described in the other sections in this chapter it is important to ensure that no two objects are the result of the same signal in the detector. In order to do this an overlap removal procedure is followed with a defined precedence of certain objects. The precedence is chosen such that objects more

Table 4.1: A table summarising the rules for removing overlapping reconstructed objects, rules are applied from top to bottom so objects removed by earlier rules will be considered in the future rules. The ΔR conditions are between the two considered objects.

Object to keep	Object to remove	Condition for removal
Electron	Tau	$\Delta R < 0.2$
Muon	Tau	$\Delta R < 0.2$
Muon	Electron	Shared ID track
Electron	Jet	$\Delta R < 0.2$
Jet	Electron	$\Delta R < 0.4$
Muon	Jet	Jet has ≤ 2 associated tracks and either ($\Delta R < 0.2$) or (Shared ID track)
Jet	Muon	$\Delta R < 0.4$
Tau	Jet	$\Delta R < 0.2$

likely to result from background processes are removed while maintaining efficiency of reconstruction of the objects of interest. Objects are determined to be overlapping by considering their spatial separation in the detector defined as $\Delta R = \sqrt{(\Delta\phi)^2 + (\Delta\eta)^2}$. The rules for the removal of overlapping objects are summarised in Table 4.1.

Chapter 5

Search for dileptonic $t\bar{t}H(H \rightarrow b\bar{b})$

This chapter details an analysis performed searching for $t\bar{t}H(H \rightarrow b\bar{b})$ with leptonically decaying top quarks using 13.2 fb^{-1} of proton-proton collision data collected in 2015 and 2016 by the ATLAS detector at the LHC. The overall strategy used for the search is described in Section 5.1 followed by the statistical procedure used to quantify the result in Section 5.2. Then the data used in the analysis is described in Section 5.3 followed by the simulated samples used and any modifications made to them in Section 5.4. The procedure to deal with events with fake leptons in them is described in Section 5.6 detailing the sources of fake leptons and the method for estimating the number of them. The sources of uncertainty on the result caused by the analysis procedure are described in Section 5.7 along with the method used to quantify them. Finally the results of the analysis are presented in Section 5.8.

5.1 Analysis Strategy

The search for the Higgs boson produced in association with top quarks is divided in ATLAS into various separate analyses performed simultaneously and combined to produce a single limit on the production cross-section of the process. In order for these different analyses to be performed simultaneously in an efficient manner and to allow ease of combination they are defined to be orthogonal and are carried out by separate analysers. The analyses are primarily categorised by the decay of the Higgs Boson they target forming three groups: $b\bar{b}$, multilepton (targeting WW^*, $\tau\tau$, ZZ^*) and $\gamma\gamma$. Primarily orthogonality is ensured through a non-overlapping selection using commonly defined reconstructed leptons discussed in Chapter 4. The
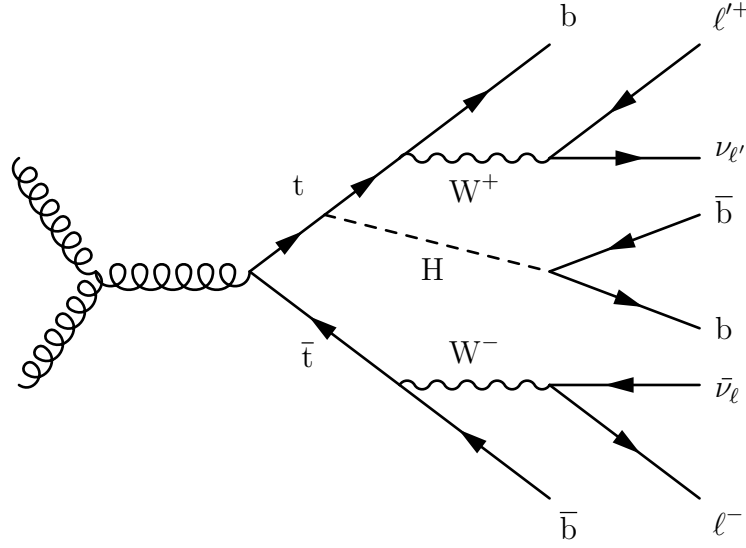
Figure 5.1: Illustrative leading-order Feynman diagram of the signal process being searched for in this thesis, dileptonic $t\bar{t}H(H \to b\bar{b})$.

$b\bar{b}$ analysis considers events with either exactly one lepton in the final state or exactly two opposite-sign leptons in the final state. For this decay the term lepton is used only to describe electrons and muons, not taus and neutrinos. Throughout this chapter the term lepton is used only to describe these two. The multilepton analysis has a variety of other selections on the leptons (including selections on taus) which define the regions, none of which coincide with the two previously mentioned. The $\gamma\gamma$ analysis does overlap with the above definitions but with the added requirement of two photons the overlap is found to be negligible.

This thesis focusses on an analysis targeting the Higgs boson decaying into a pair of b-quarks. This process is split into the two lepton categorisations which are again analysed separately in parallel. The single-lepton analysis accepts events with exactly one lepton in the final state, targeted to correspond to one of the top quarks decaying leptonically and the other hadronically. The dilepton analysis, the subject of this thesis, requires two, opposite-sign leptons in the final state, targeted to correspond to both top quarks decaying leptonically. This means that the final state of the hard scatter, excluding soft radiation, for the targeted process is expected to contain four b-quarks and two opposite-sign leptons. An example Feynman diagram of this process can be seen in Figure 5.1.

In order to constrain the uncertainty on the production of processes which do not contain a Higgs boson which give rise to similar or identical signals in the detector (the background to the search), events are separated into five analysis regions based
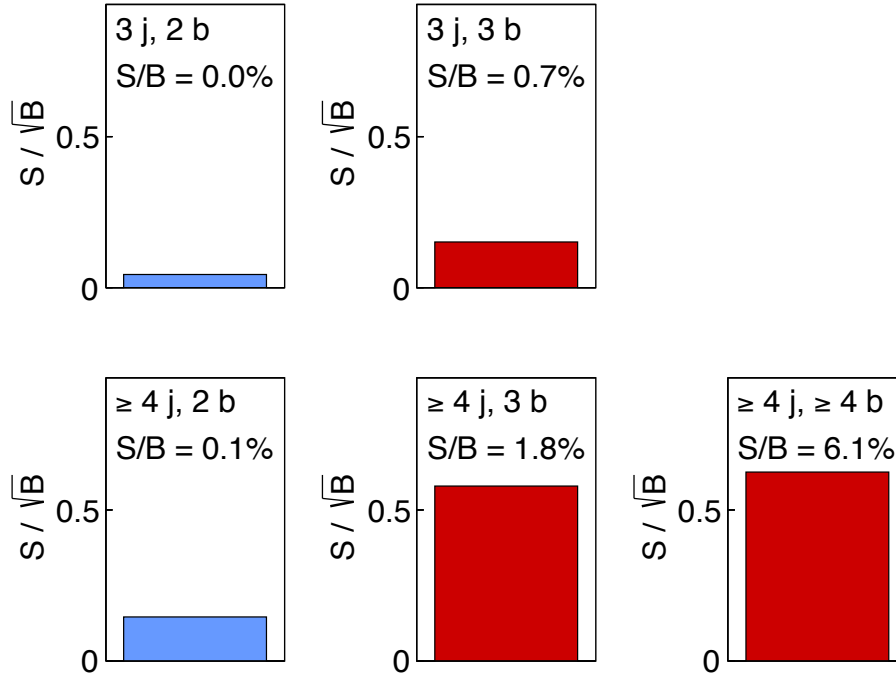
Figure 5.2: The signal purity shown for each analysis region used in the analysis, arranged with increasing number of jets towards the bottom and increasing number of b-tags towards the right. Regions treated as control regions are shown in blue, whereas regions treated as signal-enriched regions are shown in red (from [7]).
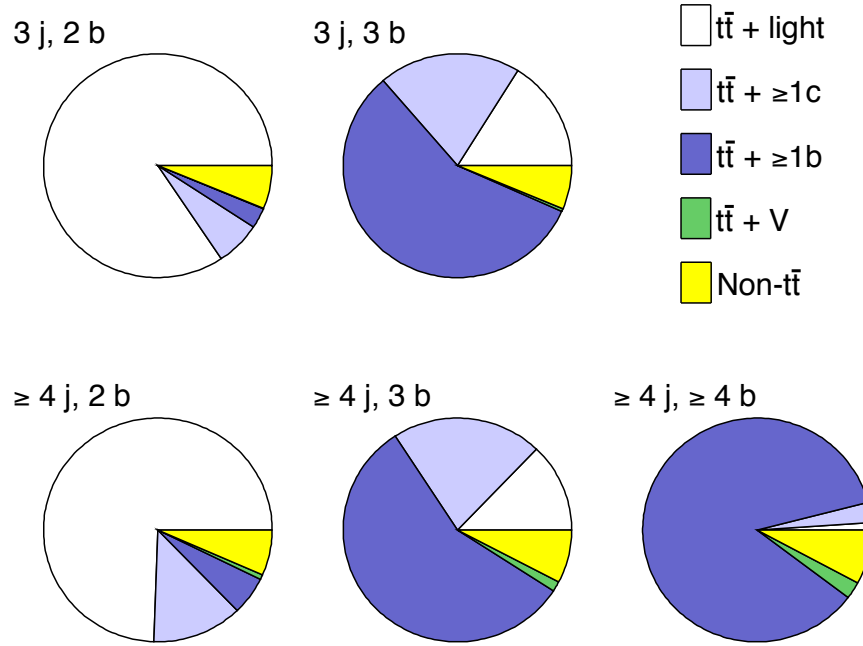
Figure 5.3: The background composition of each analysis region, arranged with increasing number of jets towards the bottom and increasing number of b-tags towards the right (from [7]).

on the number of reconstructed jets in the final state and the number of those jets that pass the b-tagging requirement. The choice of jet and b-tag multiplicities for the definition of the analysis regions is motivated by its simplicity and effectiveness at separating the events into signal enriched regions and signal depleted regions as can be seen in Figure 5.2. S/$\sqrt{\text{B}}$ is chosen to evaluate the region selection in the figure because it gives a measure of how significant a deviation from the background the signal is expected to produce in each region since the number of events measured is Poisson distributed. The analysis regions shall be referred to by the jet and b-tag requirement in the form (nj, mb) where n and m correspond to the number of jets and number of b-tags respectively. The analysis regions require the exact number of jets and tags specified unless it is indicated otherwise with a $\geq$ symbol.

A summary of the backgrounds present in each of the analysis regions can be seen in Figure 5.3 where it can be seen the majority of the expected background is comprised of t$\bar{\text{t}}$ produced with additional radiation with t$\bar{\text{t}}$ produced with additional

b-quarks dominating the signal enriched regions. Note the background $t\bar{t} + \geq 1b$ is defined by the particles present in the truth record of the Monte Carlo such that there are b-hadrons produced separate from the top decays (explained in detail in Section 5.4.2), as opposed to the region definition in which the number of b's is used to denote the number of b-tagged jets. The yields obtained in data and the prediction of each background process can be seen for each of these regions in Table 5.1 before the fit is performed. The agreement between data and prediction is good, but an increasing discrepancy can be seen in regions with a large contribution from $t\bar{t} + HF$[1] processes.

The analysis regions contribute to the search through a cross region profiled likelihood fit detailed in Section 5.2. A distribution over a single variable from each region is provided to the fit, split into the different background sources described in Section 5.4. The distributions of these variables can be seen before and after the fit is applied in Section 5.8.

In the signal depleted regions no attempt is made to separate the signal processes from the background in the input to the fit. Instead the regions are provided to help constrain the uncertainties on the background processes. As such the scalar sum of the transverse momentum of the reconstructed jets and leptons in the event, $H_{\mathrm{T}}^{\mathrm{all}}$, is used in these regions. In Figure 5.4 the comparison between the data and prediction can be seen in one of these regions. These plots show good agreement with most bins within the statistical error.

The signal enriched regions use the output of a multivariate classification algorithm as the variable contributed towards the fit. This classifier is trained to distinguish $t\bar{t}H$ processes from the inclusive $t\bar{t}$ background in order to maximise signal sensitivity in these regions. The $(3j, 3b)$ analysis region uses a neural network algorithm to separate the signal from the background, differing from the more pure signal regions.

The two regions with the highest signal purity, the $(\geq 4j, 3b)$ and $(\geq 4j, \geq 4b)$ regions, use a combination of two multivariate techniques to achieve the maximal separation of signal processes from the background. The first is a multivariate reconstruction algorithm in which a classifier is trained to distinguish the correct assignment of reconstructed jets to the b quarks in the final state in $t\bar{t}H$ events from the incorrect assignment. Two trainings of this algorithm are performed, one trained

---

[1] $t\bar{t} + HF$ is $t\bar{t}$ with additional heavy flavour radiation, where heavy flavour refers to c and b type quarks. This is the combination of the $t\bar{t} + \geq 1c$ and $t\bar{t} + \geq 1b$ categories used in the analysis.

Table 5.1: Event yields in the analysis regions. The quoted uncertainties are the sum in quadrature of statistical and systematic uncertainties on the yields not including any uncertainty on the t$\bar{\text{t}}$ + $\geq$1b or t$\bar{\text{t}}$ + $\geq$1c normalisation. For the t$\bar{\text{t}}$H signal, the yield values correspond to the theoretical prediction and corresponding uncertainties (from [7]).

	(3j, 2b)	(3j, 3b)	
t$\bar{\text{t}}$ + light	19200 ± 3600	76 ± 34	
t$\bar{\text{t}}$ + $\geq$1c	1460 ± 380	94 ± 37	
t$\bar{\text{t}}$ + $\geq$1b	660 ± 130	270 ± 90	
t$\bar{\text{t}}$ + V	44.3 ± 4.9	2.11 ± 0.69	
Single top	690 ± 230	14.8 ± 6.4	
Z + Jets	460 ± 160	5.4 ± 3.0	
Diboson	52 ± 30	4.5 ± 4.3	
Fake Lepton	210 ± 110	3.1 ± 1.8	
tH	0.76 ± 0.17	0.251 ± 0.077	
Total background	22800 ± 3800	470 ± 110	
t$\bar{\text{t}}$H	8.5 ± 1.4	3.37 ± 0.76	
Total	22800 ± 3800	470 ± 110	
Data	23772	691	
	($\geq$4j, 2b)	($\geq$4j, 3b)	($\geq$4j, $\geq$4b)
t$\bar{\text{t}}$ + light	12300 ± 4000	132 ± 67	1.11 ± 0.69
t$\bar{\text{t}}$ + $\geq$1c	2120 ± 600	218 ± 76	3.1 ± 1.7
t$\bar{\text{t}}$ + $\geq$1b	920 ± 160	580 ± 110	92 ± 32
t$\bar{\text{t}}$ + V	116 ± 13	15.1 ± 2.1	2.61 ± 0.75
Single top	450 ± 160	26 ± 14	1.72 ± 1.11
Z + Jets	340 ± 130	22 ± 11	0.37 ± 0.37
Diboson	52 ± 29	8.7 ± 8.3	4.0 ± 4.0
Fake Lepton	230 ± 120	16.9 ± 9.0	1.20 ± 0.70
tH	2.05 ± 0.47	0.71 ± 0.20	0.172 ± 0.053
Total background	16600 ± 4300	1020 ± 200	107 ± 33
t$\bar{\text{t}}$H	42.9 ± 4.9	20.6 ± 4.2	6.6 ± 2.0
Total	16600 ± 4300	1040 ± 200	113 ± 34
Data	17901	1467	154
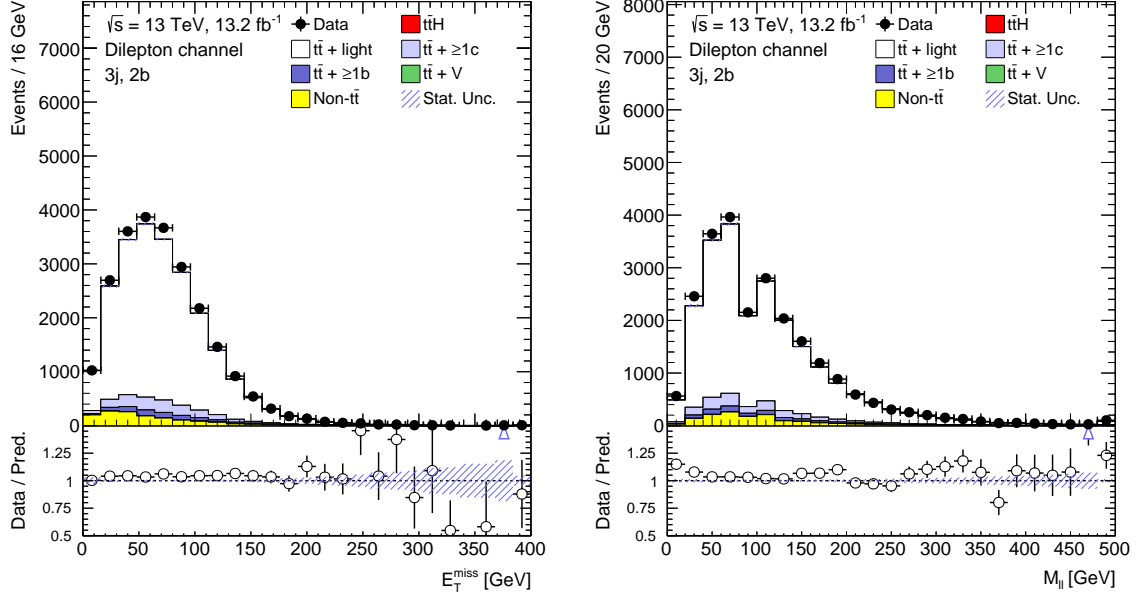
Figure 5.4: Comparison between data and prediction in the (3j, 2b) region. Note the errors displayed are statistical only, systematic errors dominate the expected error before the fit.

using only information related to the jets originating from the top quarks and one using information related to both the jets originating from the top quark and the Higgs boson. From these reconstructions, variables related to the correct assignment of the jets are used as input to the classification along with variables related to how signal-like the classifier determined the correct and incorrect assignments to be. This information along with other event information is passed to a classification algorithm utilising a boosted decision tree which produces the distribution passed to the fit. The exact variables used in each of the trainings of the classification algorithms can be seen in Tables 5.2 and 5.3.

Comparisons of the data and prediction for the most sensitive variables in the (3j, 3b) and (≥4j, ≥4b) regions can be seen in Figures 5.5 and 5.6. A consistent under-prediction is seen in the signal rich regions due to the poor t$\bar{t}$ + ≥1b modelling, this is addressed by not constraining the t$\bar{t}$ + ≥1b cross section in the fit discussed in Section 5.4.2. The low number of expected events in these regions causes the errors on the distributions to be large, also the systematic errors in these regions are large (not shown in the figures). These large errors mean while the central values of the data/MC ratio vary by a large amount the distributions are still consistent with being flat.

Table 5.2: Definition of the variables used in the multivariate classification algorithms not from the reconstruction algorithms (from [7]).

Variable	Definition	$(\geq 4j, \geq 4b)$	$(\geq 4j, 3b)$	$(3j, 3b)$
$\Delta\eta_{bb}^{avg}$	Average $|\Delta\eta|$ among pairs of b-jets	✓	−	−
$\Delta\eta_{bb}^{max}$	Maximum $\Delta\eta$ between any two b-jets	−	✓	✓
$\Delta\eta_{jj}^{avg}$	Average $\Delta\eta$ among jet pairs	−	✓	−
$\Delta R_{bb}^{max\ p_T}$	ΔR between the two b-tagged jets with the largest vector sum p_T	✓	✓	✓
ΔR_{bb}^{Higgs}	ΔR between the two b-tagged jets with mass closest to the Higgs boson mass	✓	−	−
$\Delta R_{bb}^{max\ m}$	ΔR between the two b-jets with the largest invariant mass	✓	✓	✓
$m_{bb}^{max\ p_T}$	Mass of the two b-tagged jets with the largest vector sum p_T	−	−	✓
m_{bb}^{Higgs}	Mass of the two b-tagged jets closest to the Higgs boson mass	✓	✓	✓
m_{bb}^{min}	Minimum mass of two b-tagged jets	−	−	✓
$m_{bb}^{min\ \Delta R}$	Mass of the combination of the two b-tagged jets with the smallest ΔR	✓	✓	✓
$p_{T,b}^{min}$	Minimum b-tagged jet p_T	−	−	✓
H_T^{all}	Scalar p_T sum of all leptons and jets	−	✓	✓
$N_{bb}^{Higgs\ 30}$	Number of b-jet pairs with invariant mass within 30 GeV of the Higgs boson mass	✓	−	✓
$N_{jj}^{Higgs\ 30}$	Number of jet pairs with invariant mass within 30 GeV of the Higgs boson mass	−	✓	−
Aplanarity	$1.5\lambda_2$, where λ_2 is the second eigenvalue of the momentum tensor [59] built with all jets	✓	✓	✓
Centrality	Sum of the p_T divided by sum of the E for all jets and both leptons	✓	−	✓
$H2_{jets}$	Third Fox–Wolfram moment computed using all jets	−	✓	−
$H4_{all}$	Fifth Fox–Wolfram moment computed using all jets and leptons	−	−	✓

Table 5.3: Definition of the variables used in the multivariate classification algorithm used in each signal region derived from the multivariate reconstruction algorithms (from [7]).

Variable	Definition	$(\geq 4j, \geq 4b)$	$(\geq 4j, 3b)$	$(3j, 3b)$
Variables from multivariate reconstruction not utilising Higgs information				
$m_{\mathrm{H}}^{\mathrm{reco}}$	Higgs boson mass	✓	✓	–
$\Delta\eta_{\mathrm{H},\ell}^{\mathrm{min}}$	Minimum $\Delta\eta$ between the Higgs boson and a lepton	–	✓	–
$\Delta\eta_{\mathrm{H},\ell}^{\mathrm{max}}$	Maximum $\Delta\eta$ between the Higgs boson and a lepton	–	✓	–
Variables from multivariate reconstruction utilising Higgs information				
$L_{t\bar{t}\mathrm{H}}$	The reconstruction algorithm output for the chosen object configuration	✓	✓	–
$m_{\mathrm{H}}^{\mathrm{reco}}$	Higgs boson mass	✓	✓	–
$\Delta\eta_{\mathrm{H},\ell}^{\mathrm{min}}$	Minimum $\Delta\eta$ between the Higgs boson and a lepton	✓	–	–
$\Delta\eta_{\mathrm{H},\ell}^{\mathrm{max}}$	Maximum $\Delta\eta$ between the Higgs boson and a lepton	✓	–	–
$\Delta\eta_{\mathrm{H},b}^{\mathrm{min}}$	Minimum $\Delta\eta$ between the Higgs boson and a b-jet	✓	–	–
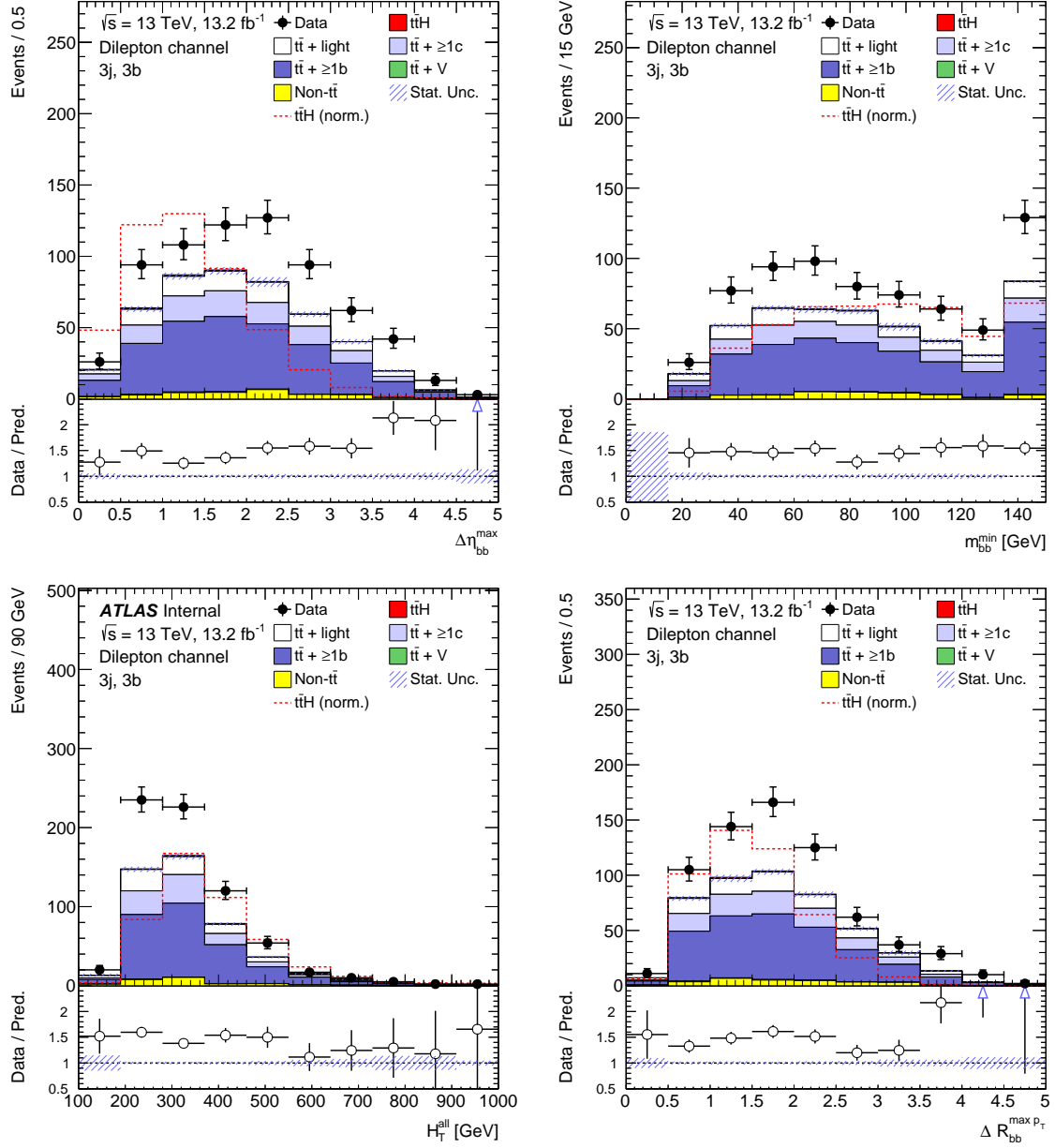
Figure 5.5: Comparison between data and prediction for the four most separating variables used as input to the multivariate classifier in the (3j, 3b) region. Note the errors displayed are statistical only, systematic errors dominate the expected error before the fit.
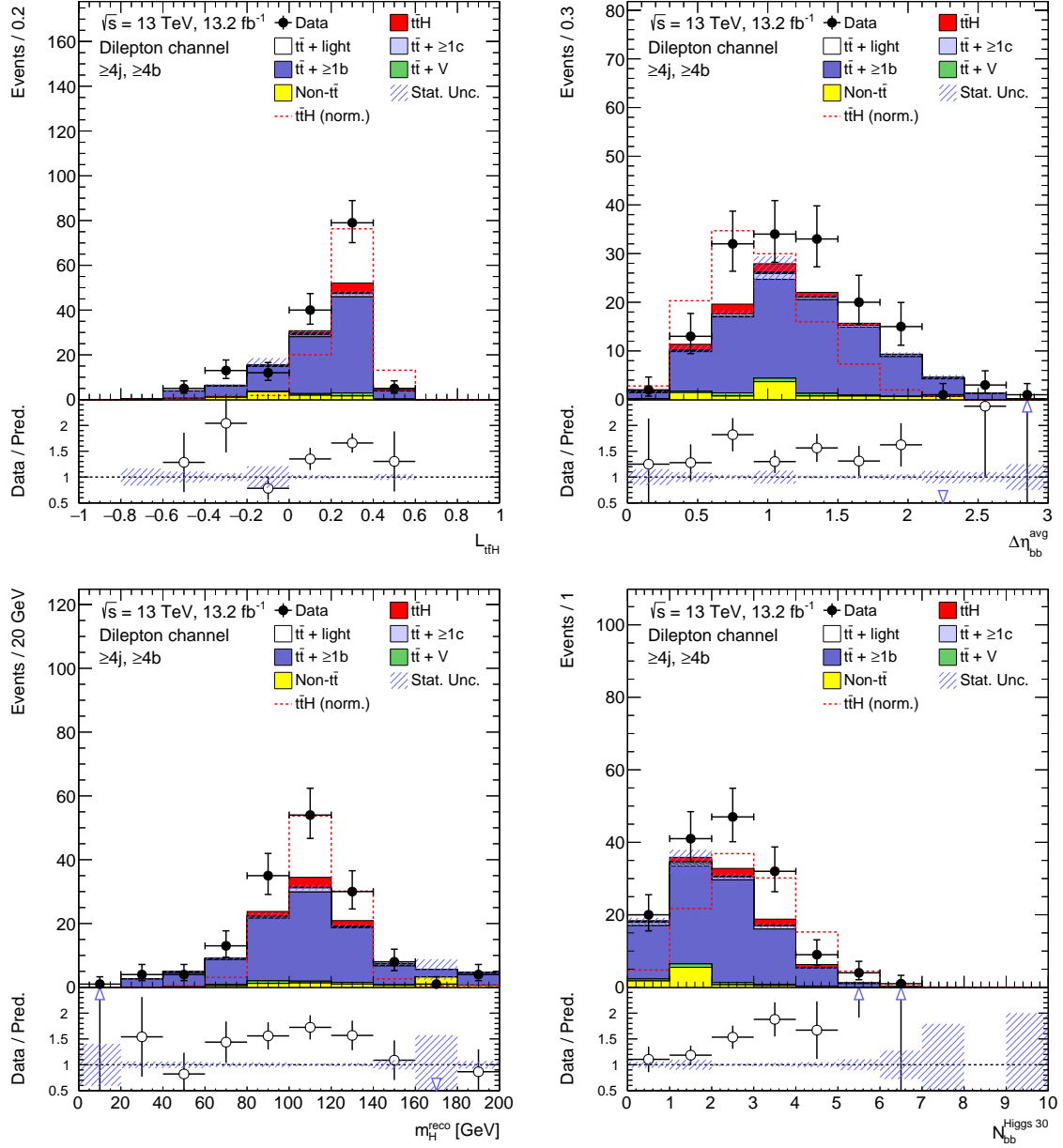
Figure 5.6: Comparison between data and prediction for the four most separating variables used as input to the multivariate classifier in the (≥4j, ≥4b) region. Note the errors displayed are statistical only, systematic errors dominate the expected error before the fit.

5.2 Statistical Procedure

The analysis is optimised to search for t$\bar{\text{t}}$H(H $\rightarrow$ b$\bar{\text{b}}$). The result of this search is quantified by considering the signal strength parameter denoted by μ. The signal strength parameter is the ratio of the observed cross-section of t$\bar{\text{t}}$H production normalised to the Standard Model expectation. This is defined such that a value of $\mu = 1$ would indicate t$\bar{\text{t}}$H production happens at precisely the Standard Model predicted rate and a value of $\mu = 0$ would indicate that t$\bar{\text{t}}$H production does not occur. This parameter is measured through a binned profiled likelihood fit along with a collection of nuisance parameters, denoted by $\vec{\theta}$. These nuisance parameters represent the uncertainty on the prediction, the specific sources of which are discussed in Section 5.7. Through the simultaneous fit of the parameter of interest and the nuisance parameters the uncertainties on the prediction can be reduced due to constraints imposed by the observed data.

In the likelihood all regions are treated equally with no distinction between the signal enriched and signal depleted regions in the fit. The exact form of the likelihood function (L) used is

$$L\left(\mu, \vec{\theta}\right) = \prod_{r \in \text{region}} \left[\prod_{i \in \text{bin}} \text{Pois}\left(n_i | \nu_i\left(\mu, \vec{\theta}\right)\right) \right] \cdot \prod_{j \in \text{systematic}} f_j(t_j | \theta_j), \qquad (5.1)$$

where $\vec{n}$ is the set of the number of measured events, $\vec{\nu}(\mu, \vec{\theta})$ is the set of the expected number of events, Pois is the Poisson probability such that $\text{Pois}(x | \lambda) = \lambda^x e^{-\lambda}/x!$ and $\vec{f}$ is the set of functions used to constrain the nuisance parameters dependent on $\vec{t}$, the set of values of the nuisance parameters from auxiliary measurements [60]. The set of functions constraining the nuisance parameters are either Gaussian functions or log-normal functions with the central value dictated by the current value of the nuisance parameter and the width of the distribution being defined by the known uncertainty on the auxiliary measurement of the nuisance parameter.

From this likelihood a test statistic q_μ can be defined proportional to a ratio of likelihoods as

$$q_\mu = -2 \ln \left(\frac{L\left(\mu, \hat{\hat{\vec{\theta}}}\right)}{L\left(\hat{\mu}, \hat{\vec{\theta}}\right)} \right), \qquad (5.2)$$

where $\hat{\mu}$ and $\hat{\hat{\theta}}$ are the values which maximise the likelihood when $\hat{\mu}$ is constrained to be greater than zero and less than μ and $\hat{\hat{\theta}}$ are the values of the nuisance parameters which maximise the likelihood function for the given value of μ. The test statistic can be used to determine the compatibility of the observed data with respect to the background-only hypothesis ($\mu = 0$ hypothesis) and an upper limit on the value of μ using the CL_s method [61, 62].

5.3 Data Samples

The analysis presented in this thesis uses $\sqrt{s} = 13$ TeV proton-proton collision data collected by the ATLAS experiment in 2015 and 2016. The combined integrated luminosity for the two years is 13207.69 pb^{-1} with 3212.96 pb^{-1} collected in 2015 and 9994.73 pb^{-1} collected in 2016. Data is only considered if all subsystems in the detector are fully operational to ensure the event, and all object contained within it can be fully reconstructed.

5.4 Signal and Background Modelling

Due to the large number of expected background processes contributing to the data in the analysis regions, a large amount of Monte Carlo generated events are used to model them. The simulation of each process has been optimised separately within the ATLAS collaboration with the help of expertise in other experiments, from theorists and from the authors of the Monte Carlo generators. A summary of the generators and the Parton Distribution Functions (PDF) used to generate each process is given in Table 5.4. As part of the process of optimising the Monte Carlo samples the internal parameters of each of the Parton Shower (PS) models was set to best replicate data. These parameter sets, known as tunes, are used consistently throughout for each PS except where otherwise noted and are summarised in Table 5.5. Throughout all the event simulation a top mass of 172.5 GeV is used. Decays of b and c hadrons are simulated with EvtGen v1.2.0 [63], except in samples simulated in Sherpa. All Monte Carlo used are also run through the full detector simulation with the exception of some samples used for quantifying the uncertainties on modelling (more detail on

Table 5.4: A table summarising the different Monte Carlo generators used for the different samples in the analysis. MadGraph5_aMC@NLO has been abbreviated to MG5_aMC for brevity.

Process	Matrix Element	Parton Shower	ME PDF	PS PDF
t$\bar{t}$H	MG5_aMC	Pythia 8.2.10	NNPDF3.0NLO	NNPDF2.3LO
t$\bar{t}$	Powheg-Box v2	Pythia 6.4.28	CT10nlo	CTEQ6L1
t$\bar{t}$ + V	MG5_aMC	Pythia 8.2.10	NNPDF3.0NLO	NNPDF2.3LO
t (t-channel)	Powheg-Box v1	Pythia 6.4.28	CT10f4	CTEQ6L1
t (s-channel)	Powheg-Box v2	Pythia 6.4.28	CT10nlo	CTEQ6L1
t (Wt-channel)	Powheg-Box v2	Pythia 6.4.28	CT10nlo	CTEQ6L1
W + Jets	Sherpa 2.1.1		CT10nlo	
Z + Jets	Sherpa 2.1.1		CT10nlo	
Diboson	Sherpa 2.1.1		CT10nlo	
tHbj	MG5_aMC[†]	Herwig++ 2.7.1	CT10f4	CTEQ6L1
tWH	MG5_aMC	Herwig++ 2.7.1	CT10f4	CTEQ6L1

[†]For this sample MadGraph5_aMC@NLO was used in LO mode.

Table 5.5: A table summarising the different tunes used for the parton shower generators.

Parton Shower	Tune
Pythia 6.4.28	Perugia 2012 [64]
Pythia 8.2.10	A14 [65]
Sherpa	Sherpa Author's Tune
Herwig++ 2.7.1	UE-EE5

which samples can be found in Section 5.7); these processes are simulated using fast simulation as discussed in Section 4.1.2.

5.4.1 Signal Modelling

Monte Carlo data simulating t$\bar{t}$H events are generated inclusively with the mass of the Higgs boson taken to be 125 GeV at next-to-leading order (NLO) in the ME calculation [66]. The ME calculation is carried out using MadGraph5_aMC@NLO [67] version 2.3.2, during which the NNPDF3.0NLO PDF set [68] is used. Spin correlations are considered in both the production and decay of particles in the ME using Madspin

[69], with the exception of the decay of the Higgs boson which handled by the PS allowing for all possible decays of the Higgs. The results of the ME are then input to Pythia 8.2.10 [70] PS model using the NNPDF2.3LO PDF set [71]. Within the PS model the factorisation and normalisation scales are both set to $\mu_F = \mu_R = H_T/2$, here H_T is defined as the scalar sum of the transverse energies ($\sqrt{p_T^2 + m^2}$) of all final state particles. The Standard Model predicted cross-section of the process is taken from NLO calculations [72–76].

5.4.2 $t\bar{t}$ Modelling

$t\bar{t}$ backgrounds comprise over 90% of the background to the search presented in this thesis in all analysis regions, as can be seen in Figure 5.3. It can also be seen in this figure that this background is split up into four categories ($t\bar{t} + \geq 1b$, $t\bar{t} + \geq 1c$, $t\bar{t} + $ light and $t\bar{t} + V$) defined by what is produced in the event alongside the top quark pair. The first three categories, collectively known as $t\bar{t} + $ Jets, are for events in which extra jets are produced. They are separated by considering the proximity of heavy flavour hadrons with truth jets reconstructed in the event. The final category is used when an additional vector boson is produced alongside the top quark pair.

Truth jets are those reconstructed directly from stable particles (excluding muons and neutrinos) produced in the parton shower reconstructed with the same algorithm as that used in reconstructed jets. To be considered in the classification the jets are required to have a transverse momentum greater than 15 GeV and an absolute pseudorapidity less than 2.5. These are then matched to hadrons containing b and c quarks (excluding those that originate from top or W-boson decays to ensure they are not from the top decay) close by in η, ϕ space ($\Delta R < 0.4$). There are two classifications of jet for each flavour of hadron in the vicinity based on the number of hadrons. The jets are classed as b or c jets if they are close to a single hadron of the respective flavour with a transverse momentum greater than 5 GeV, where c-hadrons are ignored if a b-hadron that passes the selection is close to the jet. They are instead classified with a capital letter (B or C) if additional hadrons of the same flavour are found near the jet, no transverse momentum requirement is placed on these additional hadrons. This truth jet classification nomenclature is summarised in Table 5.6.

This classification scheme leads to the three categories of $t\bar{t}$ with additional jets mentioned earlier. Jets with at least one b or B type jet are classified as $t\bar{t} + \geq 1b$, jets not falling into the previous category and having at least one c or C type jet are

Table 5.6: A table summarising the classification of truth jets depending on the presence of nearby hadrons containing b and c quarks.

Jet Label	Number of nearby b-hadrons		Number of nearby c-hadrons	
	$p_{\text{T}} \geq 0$ GeV	$p_{\text{T}} \geq 5$ GeV	$p_{\text{T}} \geq 0$ GeV	$p_{\text{T}} \geq 5$ GeV
b	$= 1$	$= 1$	≥ 0	≥ 0
B	≥ 2	≥ 1	≥ 0	≥ 0
c	$= 0$	$= 0$	$= 1$	$= 1$
C	$= 0$	$= 0$	≥ 2	≥ 1

classified as t$\bar{\text{t}}$ + ≥1c and jets satisfying neither of these categories are classified as t$\bar{\text{t}}$ + light. An extended classification scheme is used to compare Monte Carlo event generators, to derive event weights for the different generators to ensure they have the same distribution of events in each category and to derive uncertainties on the modelling of these processes. The extended classification scheme has the categories: t$\bar{\text{t}}$ + b, t$\bar{\text{t}}$ + B, t$\bar{\text{t}}$ + b$\bar{\text{b}}$ and t$\bar{\text{t}}$ + ≥3b where t$\bar{\text{t}}$ + b$\bar{\text{b}}$ is equivalent to t$\bar{\text{t}}$ + 2b and b can mean b or B in the last two definitions as with the simpler categories.

Monte Carlo data simulating t$\bar{\text{t}}$ with additional jets are generated [77] in four regions of phase space which are combined into a single sample. This is done to ensure a sufficient number of simulated events are generated for final states with small cross-sections ensuring the event distributions are correctly modelled in these areas. The regions are defined first by those with at least one leptonic top decay, and those with two leptonic top decays. The four regions are defined by further splitting those regions into those produced inclusively and those produced with at least one b-hadron alongside the top quark pair at the event generation step.

The ME calculation is performed using the Powheg-Box v2 NLO generator [78–81], during which the NLO CT10 Parton Distribution Function (PDF) set [82] is used. The h_{damp} parameter, which controls the transverse momentum of the first additional emission beyond the Born configuration, is set to the mass of the top quark. The main effect of this is to regulate the high transverse momentum emission against which the t$\bar{\text{t}}$ system recoils. The results of this are then input to Pythia 6.4.28 [83] PS model using the leading-order CTEQ6L1 PDF set [84]. This sample is normalised to the Top++2.0 [85] cross-section calculated at next-to-next-to-leading order (NNLO) in QCD that includes resummation of next-to-next-to-leading logarithmic soft gluon terms [86–90] with a value of 832^{+46}_{-51} pb.

Corrections are applied to the different $t\bar{t}$ with additional jets categories through the use of event weights. These corrections are also applied to alternative samples used to derive uncertainties on the prediction detailed in Section 5.7. The first correction corrects the shape of the distribution of the transverse momentum of the top quark and $t\bar{t}$ system to the NNLO prediction [91, 92]. The corrections to the two objects are done sequentially and are applied to the $t\bar{t}$ + light and $t\bar{t} + \geq$1c regions.

The $t\bar{t} + \geq$1b background is also corrected, with the correction derived from a dedicated $t\bar{t} + b\bar{b}$ production at NLO in both the ME and PS [93]. This sample is generated with Sherpa+OpenLoops [94, 95] for both steps of the event generation and uses the CT10 four-flavour (4F) scheme[2] PDF set. The correction is derived separated in each of the extended jet categories discussed previously such that the relative normalisations of the different categories and the corrected distributions within each category matches the Sherpa prediction. The individual category corrections are performed over a two-dimensional distribution of the transverse momentum of the top quark and $t\bar{t}$ system. In addition to this there is a further category dependent correction. In the $t\bar{t} + \geq$3b and $t\bar{t} + b\bar{b}$ categories the two-dimensional distribution of the distance between the b-jets and the transverse momentum of the b-jets is corrected. In the $t\bar{t} + B$ ($t\bar{t} + b$) category the two-dimensional distribution of the B(b)-jet transverse momentum and pseudorapidity is corrected. Events in which the additional truth b-jet is produced from multi-parton interactions or final-state radiation are not included in the NLO calculation so are not corrected in this manner and are used uncorrected. The size of the relative normalisation correction introduced by this procedure can be seen in Figure 5.7 along with the samples used for systematic uncertainties discussed in Section 5.7.

Monte Carlo data simulating $t\bar{t}$ with an additional vector boson are generated inclusively at NLO in the ME calculation [66]. The ME calculation is performed using the MadGraph5_aMC@NLO NLO generator, during which the NNPDF3.0NLO PDF set is used. The top quark and vector bosons are decayed using MadSpin to ensure spin correlations are properly propagated. The results of this are then input to Pythia 8.2.10 PS model using the leading-order NNPDF2.3LO PDF set.

---

[2]Four-flavour scheme refers to the number of flavours of quark which are considered to be massless when deriving the PDF, so in this instance u, d, s and c quarks are considered massless. It is more typical to also treat the b quark as massless in these calculations as in all other PDF sets used which use the five-flavour scheme.
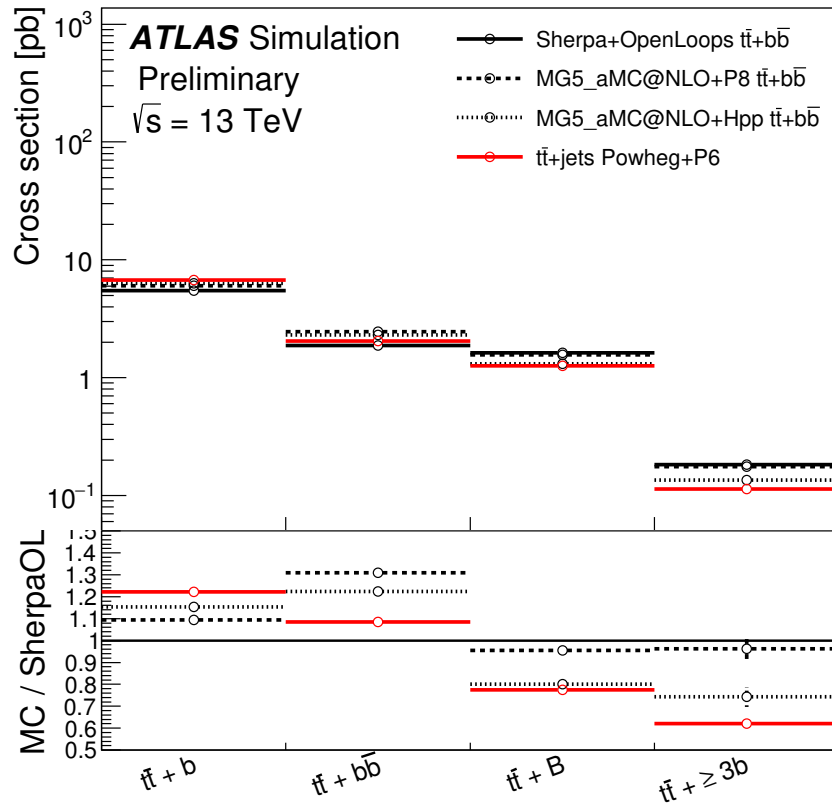
Figure 5.7: The predicted cross sections for extended categories in t$\bar{t}$ + ≥1b compared with the distribution produced by Sherpa+OpenLoops before the correction is applied (from [7]).

5.4.3 Other Backgrounds

Single Top

Single top events are simulated in three separate channels, the s, t and Wt channels based on the production mode that contributes. Of the three channels only the Wt channel contributes to the analysis selection, the other two channels are used only for the fake lepton estimation (discussed in Section 5.6). Monte Carlo data simulating single top processes produced in the s and Wt channels are produced with the same generators and settings as the default inclusive t$\bar{t}$ production [77]. At NLO accuracy there is non-trivial interference between the t$\bar{t}$ production and the single top production in the Wt-channel. In order to account for this interference a diagram removal scheme [96] is used.

Monte Carlo data simulating single top processes produced in the t channel are produced using the four-flavour scheme for the NLO ME calculation. The ME calculation is performed using the Powheg-Box v1 generator, during which the fixed four-flavour PDF set CT10f4 is used. The top quark is decayed using MadSpin to ensure spin correlations are properly propagated. The results of this are then input to Pythia 6.4.28 PS model using the leading-order CTEQ6L1 PDF set.

The cross-section for the single top production is corrected to the approximate NNLO (NLO+NNLL) theoretical cross-sections [97–99].

W/Z + Jets and Diboson

Monte Carlo data simulating W/Z production with additional jets are generated at NLO for lower jet multiplicities and LO at higher jet multiplicities in the ME calculation [100]. Note the W + Jets production does not provide any events to the analysis through the typical selection and is used only for the fake lepton estimation (discussed in Section 5.6). The ME calculation is performed using the Comix [101] and OpenLoops ME generators giving NLO predictions for up to two additional jets and LO predictions for 3 and 4 additional jets. Predictions at higher jet multiplicities are simulated using the PS. The ME calculation is then merged with the Sherpa PS using the ME+PS@NLO prescription [102], the Sherpa settings are left as those recommended by the package authors. The NLO CT10 PDF set is used throughout. The cross-section of the processes are corrected to the NNLO cross-sections [103, 104].

A correction to the Z + Jets production rate is derived to replicate the event yield seen in data with a dilepton mass close to that of the Z-boson. This leads to a factor of 1.09 applied to Z + Jets events with exactly one heavy flavour truth jet and a factor of 0.95 is applied to events with at least two heavy flavour truth jets.

Monte Carlo data simulating diboson production are generated using the same generation tools as with W/Z + Jets [105]. In the case of diboson production the ME predicts the process at NLO for up to one additional parton and LO for up to three additional partons. The cross-section for this process is used directly from the Monte Carlo prediction so is at NLO accuracy in QCD.

tH

Monte Carlo data simulating tH are generated separately in two final states, tHbj and tWH. tHbj is generated at LO using the MadGraph5_aMC@NLO generator configured to calculate in the four-flavour scheme with the top quark decayed using MadSpin to ensure spin correlations are properly propagated. The results of this are then input to the Herwig++ 2.7.1 PS model. The cross-section is corrected to the NLO value.

tWH uses the same generators but the ME is calculated at NLO in the five-flavour scheme and MadSpin is not utilised for this sample. The cross-section for this process is taken directly from the Monte Carlo prediction so is at NLO accuracy in QCD.

5.5 Event Selection

Before events are separated into the different analysis regions discussed in Section 5.1 a selection is made to remove events which are not well modelled or calibrated and to remove as many events from background processes as possible while maintaining a high signal efficiency. These selections are applied identically to both data and Monte Carlo events to ensure the prediction matches the data as closely as possible. The selection happens on reconstructed objects after overlap removal has taken place, as described in Section 4.2.7. The events are separated into three channels based on the flavour of the leptons present as electrons and muons are calibrated to different transverse momenta and the triggers differ for the two flavours: the three channels are electron-electron (ee), electron-muon (eμ) and muon-muon ($\mu\mu$).

A single primary vertex is required and must be associated with two or more tracks with transverse momenta above 0.4 GeV. In the case where multiple primary vertices are found the vertex with the highest sum of the squared transverse momenta of its associated tracks is used as the primary vertex, the other primary vertices are known as pile-up vertices. Monte Carlo data is simulated with different numbers of pile-up vertices and event weights are used to ensure the distribution of the number of pile-up vertices in Monte Carlo matches the data distribution.

The events are required to have been triggered by one of the single-lepton triggers used during the data taking period. The triggers changed between the 2015 and 2016 runs so there are different requirements for each group of events. To ensure the Monte Carlo matches the data events, they are randomly assigned a year such that the number of events in each year is proportional to the integrated luminosity collected for that year. For both the electron and muon trigger a logical OR of multiple triggers is used with differing transverse momentum, identification criteria and isolation requirements where the higher transverse momentum triggers have looser requirements on the other properties allowing high efficiency selection of high transverse momentum leptons. The triggers used are summarised in Table 5.7. The ee channel requires the event to have been triggered by any of the electron triggers, the $\mu\mu$ channel requires the event to have been triggered by any of the muon triggers and the eμ channel requires the event to have been triggered by any of the electron or muon triggers.

Events that pass these selections next have a requirement on the transverse momentum of the reconstructed leptons. In the case of the higher transverse momentum lepton (known as the leading lepton) the threshold is set such that the lepton is in the range where the trigger's efficiency is flat. In the case of the lower transverse momentum lepton (known as the subleading lepton) the threshold is set to where leptons can reliably be reconstructed and accurately measured. The leading lepton is required to have a transverse momentum of at least 25 GeV and the subleading lepton is required to have a transverse momentum of 10 GeV (15 GeV for the ee channel), there is no flavour requirement on the leading lepton in the eμ channel.

The leptons are also required to be within the range of the inner detector for efficient tracking ($|\eta| < 2.5$) and the region between the barrel and endcap calorimeters ($1.36 < |\eta_{\mathrm{cluster}}| < 1.52$) is removed for electrons. The tracks must be associated with the primary vertex such that the longitudinal impact parameter z_0 satisfies $|z_0 \sin\theta| < 0.5$ mm. Also the transverse impact parameter significance, $d_0/\sigma(d_0)$ must be less than 5 for electrons or 3 for muons. There is also an isolation requirement in

Table 5.7: Summary of the settings of the triggers used in the analysis. Note the electron identification criteria are based on a likelihood distribution and the var in the muon isolation indicates a variable sized cone is used for the isolation requirement.

Lepton	Year	Requirements for selection		
		Transverse Momentum	Identification	Isolation
Electron	2015	> 24 GeV	medium	none
		> 60 GeV	medium	none
		> 120 GeV	loose	none
	2016	> 24 GeV	tight	loose
		> 60 GeV	medium	none
		> 140 GeV	loose	none
Muon	2015	> 20 GeV	-	loose
		> 50 GeV	-	none
	2016	> 24 GeV	-	var medium
		> 50 GeV	-	none

order to reduce the background from leptons produced from hadronic decays. The Gradient isolation working point is used as documented in reference [45] for electrons and reference [46] for muons, which has an efficiency of 90%(99%) for leptons with a transverse momentum of 25 GeV(60 GeV). At least one of the leptons must be matched to a lepton candidate from the trigger that was selected for that event. The two leptons are required to be of opposite sign so they are consistent with coming from a top and anti-top decay. Finally in the two same flavour channels (ee and $\mu\mu$) there is a requirement on the invariant mass of the two lepton system to be greater than 15 GeV and not within 8 GeV of the Z-boson mass (taken to be exactly 91 GeV for this purpose) to remove the t$\bar{t}$ + Z background.

The jets in the event are built using the anti-kt algorithm using a distance parameter of 0.4. All jets are required to pass a jet quality selection with working point BadLoose as described in reference [106]. An exception to this requirement is made for jets with a transverse momentum less than 60 GeV in the central detector region ($|\eta| < 2.4$) which are marked as pileup jets through the consideration of their JVT. Furthermore all jets are required to have a transverse momentum greater than 25 GeV and should be within the region of the inner detector ($|\eta| < 2.5$). The number of jets and the number of these jets which are b-tagged is defined by the analysis regions discussed in Section 5.1.

Table 5.8: The predicted yields with 13.2 fb^{-1} of data for the various sources of fake leptons in events with two opposite sign reconstructed leptons which pass the analysis selection from all the Monte Carlo samples used, excluding systematic samples.

Source	Electron Yield	Muon Yield
Lepton from photon conversion	174 ± 7.00	0.00 ± 0.00
Lepton from hadron decay	50.4 ± 2.61	145 ± 4.94
Hadron reconstructed as a lepton	10.3 ± 1.28	0.875 ± 0.324
Muon reconstructed as an electron	7.90 ± 3.01	n/a
Lepton from tau decay	4.66 ± 1.09	4.52 ± 1.04
No truth match	0.113 ± 0.113	37.6 ± 2.42
Other	1.84 ± 0.385	0.0321 ± 0.00970
Total	249 ± 8.24	188 ± 5.61

5.6 Fake Lepton Estimation

Alongside the background processes described in Section 5.4 the search has a background in which the reconstructed leptons are faked. Events containing these leptons are known as fake lepton events. Fake leptons can originate in two ways: from mis-reconstructed leptons and from non-prompt leptons. In this instance the use of the term mis-reconstructed leptons is used to refer to signals in the detector from non-leptonic sources that pass the lepton reconstruction criteria and should not be confused with a lepton being mis-reconstructed as some other object. Non-prompt leptons are those not produced as a direct result of the hard scatter but from the decay of particles either resulting from the hard scatter or those not from the hard scatter, such as particles from pile-up collisions. A summary of the sources of fake leptons can be seen in Table 5.8. The numbers in this table, along with the following yields are produced using the method outlined in Section 5.6.2.

5.6.1 Sources of Fakes

Electrons

In Table 5.8 it can be seen that the largest contribution to the electron fakes is due to real electrons produced from a photon conversion in which a photon decays into an electron positron pair. Photons in the ATLAS detector convert to electrons within the

Table 5.9: The predicted yields with 13.2 fb^{-1} of data for the various sources of photons which convert into fake electrons in events with two opposite sign reconstructed leptons which pass the analysis selection from all the Monte Carlo samples used, excluding systematic samples.

Source	Yield
Unknown Origin	76.5 ± 6.02
Final State Radiation	70.6 ± 3.01
Bremsstrahlung	13.5 ± 1.34
Initial State Radiation	3.83 ± 0.893
Other	9.51 ± 1.03
Total	174 ± 7.00
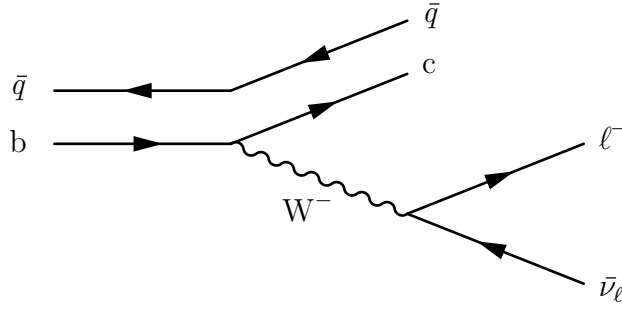
Figure 5.8: Feynman diagram of a leptonic b decay within a meson.

inner detector between 20% and 60% of the time depending on their pseudorapidity [53]. This leads to a large number of electrons from converted photons, some of which are incorrectly reconstructed as primary electrons. The distribution of the source of these converted photons can be seen in Table 5.9, where unknown origin indicates it was not possible to identify the source of the photon from the information provided by the Monte Carlo generator. Note that converted photons which arise from a hard bremsstrahlung of a lepton from the hard scatter are not considered to be fake leptons. The next largest contribution to the fake electrons is from leptonic decays of hadrons, predominately comprised of decays of b-quarks in mesons as can be seen in Figure 5.8. These first two sources are both classed as non-prompt production of fakes.

The next two largest contributing sources of fake electrons are from hadrons and muons being incorrectly reconstructed as electrons, both being classed as mis-reconstructed electrons. Note that very few fake electrons are seen in the analysis and very few of those are in the category of mis-reconstructed electrons due to the strict requirements on electron reconstruction and the high performance of the reconstruction

algorithms. A hadronic jet can fake an electron if during the parton shower the hadron predominantly decays into neutral pions with very few, or even a single, charged pion leaving a track in the inner detector. The neutral pions typically decay to photons before reaching the calorimeter which would give a similar signal in the electromagnetic calorimeter to an electron. If sufficiently high energy the inferred mass measurement from the track will have a large enough error it can be reconstructed as the track for an electron. This can then lead to the combination of the track and calorimeter deposit being reconstructed as an electron. Muons can fake electrons through the combination of the track left by the muon and an energy deposit in the calorimeter left by a photon emitted from the muon via bremsstrahlung radiation. In order for this to occur the muon left after the bremsstrahlung must not be reconstructed as a muon, either because it travels through a gap in the muon spectrometer or the reconstruction fails, otherwise the electron would be removed during overlap removal.

Muons

In Table 5.8 it can be seen the largest contribution to muon fakes is muons produced from the decay of hadrons, making up approximately 77% of fake muons. These are classified as non-prompt muons. The yields of fake muons from the different hadrons from which these muons are produced can be seen in Table 5.10. The yields are produced for opposite sign leptons in the object selection and the primary source of fake leptons in the analysis is from t$\bar{\text{t}}$ events leading to a large number of charm meson decays producing fake muons. This is caused by the charge correlation of the two W-bosons from the top quark decays, one of which decays into a lepton with the same charge as the W and the other decays into quarks predominantly either a u-, d-quark pair or a c-, s-quark pair[3]. Of these the charm quark is the only quark with an expected lifetime short enough to decay and have the decay product be reconstructed as originating at the primary vertex leading to a large number of fake muons from charm decays. The next most prevalent hadron source is bottom mesons, which are formed from the b-quark from the t-quark decays. The rate at which these occur is smaller than the charm mesons due to the higher energy in the b-quarks. This means it is less likely for an isolated muon to be produced.

---

[3]The decays have one quark and one anti-quark in each pair, which flavour is the quark is dependent on the charge of the W-boson.

Table 5.10: The predicted yields with 13.2 fb^{-1} of data for the various types of hadron which produce fake muons in events with two opposite sign reconstructed leptons which pass the analysis selection from all the Monte Carlo samples used, excluding systematic samples.

Source	Yield
Charm meson	78.5 ± 3.88
Bottom meson	46.3 ± 2.49
Pion	10.3 ± 1.31
Baryons	5.02 ± 0.767
Kaon	3.94 ± 0.868
Other Mesons	1.21 ± 0.265
Total	145 ± 4.94

A small number of fake muons are from hadrons reconstructed as muons, categorised as mis-reconstructed muons. Hadrons can give a signal that appears to be a muon either by having a sufficiently long lifetime such that they pass through the calorimeter without decaying then leaving a track in the muon spectrometer or having sufficiently high enough energy to 'punch through' the calorimeter and leave a track in the muons spectrometer. As with electrons there are very few of this type of fake muon due to the strict requirement on the muon reconstruction and the high performance of the reconstruction algorithms.

5.6.2 Method for Estimation

Identification of Fakes

In ATLAS there have been many techniques developed for the estimation of fake backgrounds including the estimation of fake lepton backgrounds in t$\bar{\text{t}}$ events [107]. The majority of these techniques are data driven techniques with Monte Carlo only being used to remove the expected number of "real" events from the distributions to isolate the fake leptons.

One such technique known as the matrix method was used by the analysis targeting the single-lepton final state, which was combined with this analysis in the search for t$\bar{\text{t}}$H. This technique relies on the definition of a fake enriched region alongside a fake depleted region. It uses the yields from these two regions alongside separately

measured efficiencies for fake rejection in each to derive the expected number of fake lepton events in the analysis regions. This technique requires a high yield in both the looser and tighter regions and accurate measurement of efficiencies in order to be effective.

Due to the increasing instantaneous luminosity provided by the LHC the triggers used have had to have stricter requirements on events to be selected, leading to a reduction in the number of recorded data events classified into the fake enriched region. This reduction, alongside improvements in the lepton reconstruction algorithms providing excellent fake rejection have made a measurement of this sort more challenging and subject to more uncertainty. Furthermore to use this technique in a dilepton analysis an extra two regions need to be defined to allow for either of the two leptons recorded to be fake, or both be fake. Finally the analysis regions most sensitive to the t$\bar{\text{t}}$H process are in high jet and b-tag multiplicities in which far fewer events are produced meaning dedicated fake measurements of this sort are not able to be applied directly in the most sensitive regions but must be extrapolated from lower jet and b-tag multiplicities. For these reasons a different approach to calculating fakes has been pursued in this analysis.

In the case of fakes in a dilepton final state the rate of having a single fake lepton is at around 1% of selected events. The rate of having both the isolated leptons being fake then becomes vanishingly small and as such is neglected. The consequence of neglecting events with two fake leptons is that Monte Carlo simulation of processes containing a single lepton can be used alongside those containing two leptons to estimate the quantity and distribution of fake events in the analysis. This is important as in the case of events with no prompt leptons only jets are expected, some of which are b-tagged. This background is influenced heavily by our understanding of QCD which prevents generating Monte Carlo events of this type to a high accuracy. It is also for this reason that the single-lepton analysis must use a data driven approach to estimating the fake lepton background when in the dilepton analysis Monte Carlo simulation can be used.

In order to categorise the events in Monte Carlo as containing fake leptons or not, the reconstructed leptons need to be matched to particles in the truth record produced by the simulation. This is performed by considering the inner detector tracks for electrons and combined tracks for muons and comparing the hits from these tracks to those from truth tracks to find the matching truth particle. The truth track is then verified by checking it is close to the reconstructed lepton. This is done by requiring

$\Delta R < 0.2$ if there are at least three silicon hits for the track else it is required that $\Delta\phi < 0.2$ to take into account the lack of ϕ measurement from the TRT. In the case these checks fail the lepton is not matched to a truth track and it is considered fake, with its origin set to 'unknown'.

Once the truth track is identified the leptons can be classified as 'real' or fake. In order to be classified as 'real' the truth particle's parents are investigated using the information provided by the generator. If the lepton is from the direct decay of a W, Z, t or H then it is considered to be a 'real' prompt lepton, else it is considered to be a fake lepton. There is also recovery of electrons that are the result of a 'real' lepton classified in the above manner undergoing a bremsstrahlung emission in which a large proportion of the electron's energy is transferred to the bremsstrahlung photon, which subsequently undergoes photon conversion and an electron is reconstructed as a result. The composition of the fake leptons as measured using this truth information from Monte Carlo events with two reconstructed, opposite-sign leptons is discussed in Section 5.6.1.

This process of identifying fakes is carried out in all Monte Carlo samples as described in Section 5.4 with the exception of the t$\bar{\text{t}}$H sample. These are excluded because all the events in this sample are signal events regardless of whether the leptons contained within are from fake sources or not. Note some of the samples described previously will only contribute events to this category as there is only one 'real' prompt lepton produced in those processes such as some diboson samples, s- and t-channel single top production and W + Jets.

Corrections

In order to verify that the Monte Carlo does an effective job at describing the distribution of fakes the predicted number and distribution of fakes with a same-sign selection is compared to data. From this comparison a correction factor is derived which is applied to the fakes obtained from Monte Carlo with the normal analysis selection. Same sign data is used as it is expected to provide a much purer sample of fake lepton events due to the much smaller rate of known processes which occur giving the final state. Due to this small number of expected events the same sign data is considered with an inclusive two jet selection with at least two jets b-tagged. This includes all analysis regions and provides sufficient events to verify the shape and normalisation of the fake lepton events. With the exception of the requirement

Table 5.11: Yields with the same-sign selection in the (≥2j, ≥2b) region with 13.2 fb^{-1} of data. Errors are statistical only.

Channel	Data	Prompt MC	Fake MC	Correction Factor
Subleading e	287	178 ± 6.56	94.1 ± 3.42	1.16
Subleading μ	299	129 ± 5.84	92.7 ± 3.53	1.83

that the leptons have the same charge instead of opposite charges all other aspects of the analysis flow remain identical, the exact same software infrastructure is used.

Due to the very different sources of fakes for electrons and muons the events are separated into two channels with the goal of having all the fake electrons in one and all the fake muons in the other. The two channels used are defined by the flavour of the lepton with the smaller transverse momentum: the subleading e and subleading μ channels. This splitting selects over 98% of fake muons into the subleading μ and about 80% of fake electrons into the subleading e channel.

The yields found in these channels with the full dataset used in the analysis and for prompt and fake Monte Carlo data can be seen in Table 5.11. We can clearly see that the prediction shows the same sign region has far more fakes relative to the number of prompt events allowing us to correct our prediction. The difference in yield between data and prediction is quite large so a correction factor is derived as

$$\text{Correction Factor} = \frac{N_{\text{Data}} - N_{\text{Prompt MC}}}{N_{\text{Fake MC}}}. \tag{5.3}$$

This factor is used as an event weight for fakes in the opposite sign Monte Carlo when it is used in the rest of the analysis.

The distribution of the same sign data and predictions can be seen in Figure 5.9. It can be seen that the Monte Carlo appears to do a good job of modelling the distribution of fakes seen in the same sign region. The ratio between the data with prompt Monte Carlo subtracted and the number of fakes expected is consistent with being flat; as such no correction to the shape of the distribution is applied to the opposite sign prediction.

This correction to the fake leptons is considered to be sufficient to quantify the fake leptons in the analysis. The expected fake lepton yield is very low with only about 1% of the expected background events being fakes across all analysis regions,
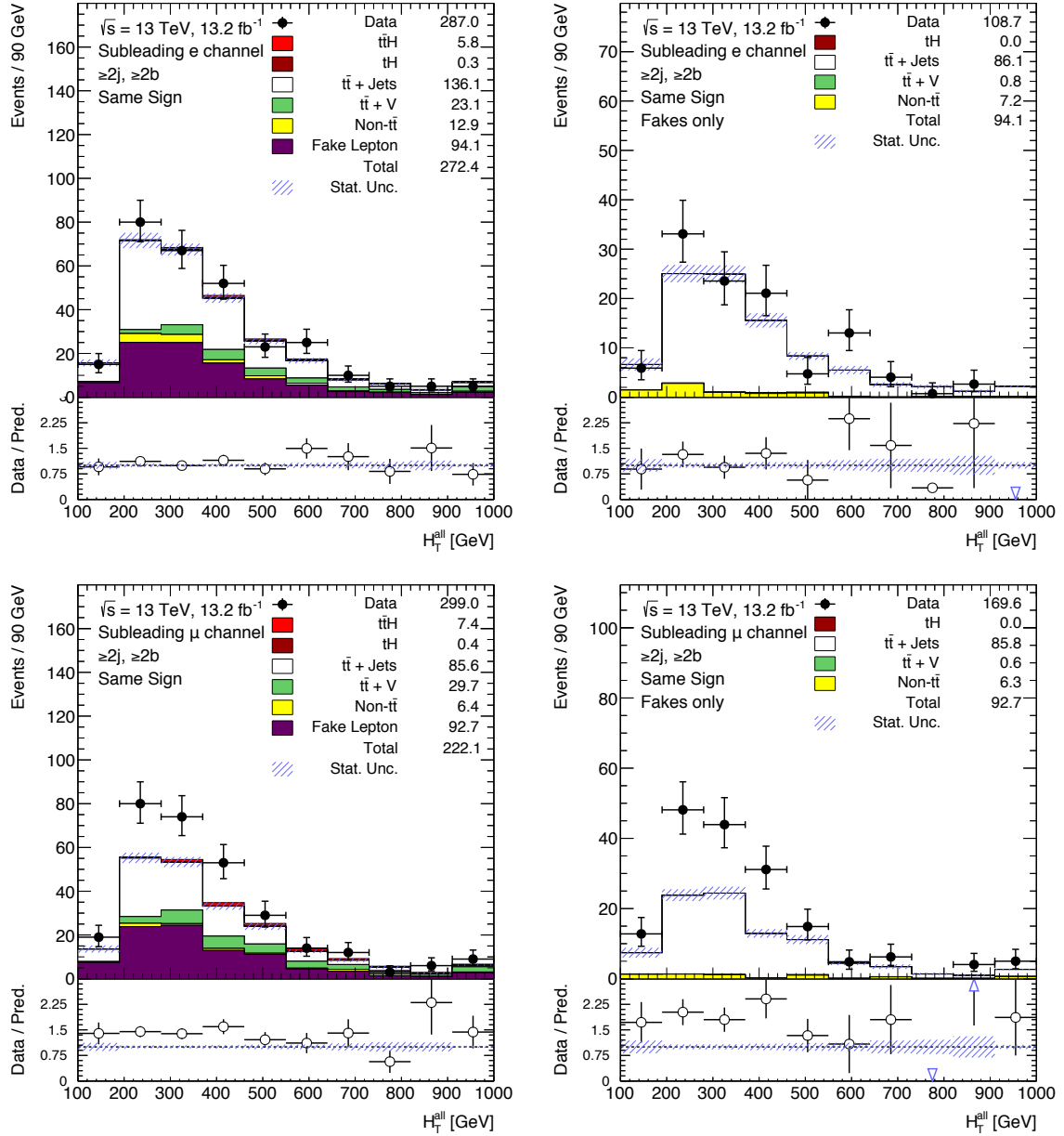
Figure 5.9: Comparison between same sign data and prediction over the scalar sum of jet and lepton transverse momenta ($H_{\text{T}}^{\text{all}}$) for the subleading e (top) and subleading μ (bottom) channels. On the left is the comparison of data with all simulated samples. On the right is the comparison of data with prompt Monte Carlo subtracted and the fake lepton backgrounds separated into the different sources.

as can be seen in Table 5.1. Furthermore an uncertainty is added to the fake lepton background yield which is larger than the correction applied, discussed in Section 5.7.2. The value of the nuisance parameter in the fit associated with this uncertainty is not pulled and the error on the value after the fit is equivalent to that before the fit. The effect of this systematic on the signal sensitivity has been checked and it is found to be negligible compared to the other uncertainties in the analysis.

5.7 Systematic Uncertainties

In a complex data acquisition and analysis chain there are many procedures involved, each of which have an associated uncertainty. These uncertainties are taken into account in the analysis on the global fit in the form of variations in either the normalisation or shape and normalisation of distributions, each of which has an associated nuisance parameter as explained in Section 5.2. A summary of the sources of the uncertainties in this analysis and the number of nuisance parameters associated to them in the fit is given in Table 5.12. Unless otherwise stated all the uncertainties are considered to be independent and fully correlated across all the analysis regions.

5.7.1 Experimental Uncertainties

One set of uncertainties contributing to the analysis are those resulting from the way the data was acquired and is processed, these are collectively known as the experimental uncertainties. As a result of the way signals in the detector are reconstructed into objects before being used in the analysis these uncertainties are separated not into uncertainties caused by parts of the physical detector but into the uncertainties on the information inferred from the detector in the object reconstruction discussed in Section 4.2.

Luminosity

The first uncertainty is not part of the object reconstruction chain but is in the measurement of the number of collisions delivered to the ATLAS detector: the luminosity measurement. A single uncertainty is used, with the value taken to be 2.9% and is applied to the combined 2015 and 2016 data set and affects all predictions based

Table 5.12: The sources of uncertainties considered along with the number of nuisance parameters (NPs) associated with them. The uncertainties are classified as either being normalisation-only (N) uncertainties or both shape and normalisation (SN) uncertainties.

Source of Uncertainty	Type	Number of NPs
Experimental Uncertainties		
Luminosity	N	1
Pileup modelling	SN	1
Electron trigger and reconstruction	SN	6
Muon trigger and reconstruction	SN	11
Jet reconstruction	SN	21
Missing transverse energy	SN	3
Jet flavour tagging	SN	25
Modelling Uncertainties		
t$\bar{\text{t}}$H cross section and branching ratios	N	5
t$\bar{\text{t}}$H modelling	SN	4
t$\bar{\text{t}}$ + Jets cross section	N	1
t$\bar{\text{t}}$ + light modelling	SN	5
t$\bar{\text{t}}$ + $\geq$1c normalisation	N	1
t$\bar{\text{t}}$ + $\geq$1c modelling	SN	6
t$\bar{\text{t}}$ + $\geq$1b normalisation	N	1
t$\bar{\text{t}}$ + $\geq$1b modelling	SN	13
t$\bar{\text{t}}$ + V cross section	N	4
t$\bar{\text{t}}$ + V modelling	SN	2
Single top cross section	N	1
Single top modelling	SN	3
Z + Jets cross section	N	5
Diboson cross section	N	1
tH cross section	N	4
Fake lepton normalisation	N	1

on Monte Carlo data. The procedure to measure this follows a similar methodology to those used in 2007 and 2008 detailed in [108, 109] which incorporates data collected during van der Meer scans [110] performed in August 2015 and May 2016. During these scans each beam in turn is displaced in the x and then the y plane such that at each extreme no collisions occur. The shape of the distribution of luminosity versus beam position is used to calibrate the luminosity measurement.

Pileup Modelling

Due to the fact that the exact distribution of pileup that will be delivered by the LHC is not known until the data has been collected, and the process to generate all the Monte Carlo simulations including the simulation of the interactions with the detector is a lengthy process, it is implausible to generate events with the correct distribution of pileup vertices. A best guess is made for the distribution of pileup that will be delivered by the LHC and an event weight is applied to the Monte Carlo to ensure the distribution of pileup vertices matches that in the collected data. This process introduces some uncertainty on the exact shape and normalisation of the predictions. This uncertainty is quantified in a single shape and normalisation variation for all simulated samples.

Electron Trigger and Reconstruction

Uncertainties on the electrons arise from the identification, isolation, reconstruction, and trigger efficiencies, along with the energy resolution and scale. In the case of the four efficiencies, a difference in the distributions of predicted and data events is observed. Scale factors are derived by using tag-and-probe techniques on Z → ee events in data and simulation and applied to the leptons to correct these distributions to those in data. For each of the measurements from which the four scale factors are derived an uncertainty is derived as a correction to the event weight and is applied to all samples in the analysis.

The uncertainties on the energy resolution and scale are estimated through a procedure developed in Run 1 and updated for Run 2 accounting for more than 70 independent systematic variations [111]. These are reduced down to a simplified model of the uncertainty by summing all of the sources of uncertainty to a single systematic variation for the resolution and another for the scale. This gives a conservative estimate

for the uncertainty which is used due to the low sensitivity of this search to this uncertainty.

Muon Trigger and Reconstruction

Uncertainties on the muons arise from the identification, isolation, track-to-vertex-association, and trigger efficiencies, along with the energy resolution and scale. As with the electron efficiency uncertainties, the four uncertainties are defined by variations in the scale factors derived to correct each efficiency. However, in the case of the muons the statistical and systematic uncertainties in the four efficiency measurements are separated into two uncorrelated uncertainties in this analysis, leading to eight uncertainties based on these efficiencies.

The uncertainties on the energy resolution and scale are estimated using J/$\psi \rightarrow \mu\mu$ and Z $\rightarrow \mu\mu$ decays [46]. These are represented by a single uncertainty on the energy scale and two independent uncertainties on the energy resolution in the inner detector and the muon spectrometer.

Jet Reconstruction

Uncertainties on the jets arise from the jet energy scale and resolution calibrations, and from the jet vertex tagger. The uncertainty on the jet energy resolution and jet vertex tagger are each quantified as a single uncertainty.

A large number of uncertainties on the jet energy scale are introduced in the jet calibration procedure detailed in Section 4.2.4. If these were used without any simplification 65 uncertainties would need to be implemented in the analysis [47]. In order to simplify this the total covariance matrix for the uncertainties is constructed and diagonalised to give a set of independent uncertainties from the eigenvectors and eigenvalues of the matrix. An approximation of this matrix is taken by keeping the five uncertainties with the largest eigenvalues and combining the remaining uncertainties into residual uncertainty. In addition to this are 13 uncertainties on the energy scale: three from the eta intercalibration procedure, one from the behaviour of high transverse momentum jets, four from the pile-up modelling of jets, and five uncertainties related to the flavour and topology uncertainties.

Missing Transverse Energy

The missing transverse energy is made from the vector sum of all reconstructed objects in the event along with a soft term. While each of the terms in this sum will introduce systematic uncertainties on the energy resolution and momentum scale, the uncertainties due to the measurement of the reconstructed objects is already accounted for in their own dedicated uncertainties which are propagated into the corresponding change in the missing transverse energy. This leaves the uncertainties on the soft term which are evaluated by considering the momentum balance in J/$\psi \rightarrow \mu\mu$ events in which no missing transverse energy is expected.

In events with no expected missing transverse energy the soft term should cancel out the vector sum of transverse energy from the reconstructed objects. The uncertainties are separated into terms which are parallel to this sum and terms that are perpendicular. The size of the systematic uncertainty is then evaluated by performing a fit of the soft term separately in the two directions using the prediction from Monte Carlo convoluted with a Gaussian function. In the case of the parallel term the mean of the fitted Gaussian function is used to specify the momentum scale uncertainty and the width is used as one of the two energy resolution terms. The other energy resolution term arises from the width of the Gaussian in the fit in the perpendicular plane. In this plane the mean of the Gaussian function is defined as zero because the hadronic recoil only affects the perpendicular component of the soft term [112].

Jet Flavour Tagging

Uncertainties arise from the measurement of the flavour tagging efficiencies. The efficiencies are measured separately when considering the behaviour of light, c and b-tagged jets. Each is performed with an enriched sample of the respective jets. A sample enriched with b-jets is made by considering the likelihood the jet is derived from a b-meson in dileptonic t$\bar{\text{t}}$ events. The likelihood is determined using correlated information from multiple jets in the event [113]. The c jets enriched sample is made by reconstructing D*-meson decays within jets, and the light jet enriched sample is attained by considering jets with an impact parameter consistent with the particle having a negative lifetime [114].

Each of these efficiency calculations leads to a large number of uncertainties. As with the case with the jet energy scale the uncertainties are reduced by diagonalising the

matrix of uncertainties and taking the eigenvectors with the largest eigenvalues along with a residual uncertainty as separate uncorrelated uncertainties. This process leads to five uncertainties from the b-jet efficiencies, four uncertainties from the c-jet efficiencies and fourteen uncertainties from the light-jet efficiencies. These measurements are only valid up to about 300 GeV and are extrapolated beyond this to correct all jets. An extra uncertainty is included to account for this extrapolation. Finally due to the complication with measuring these efficiencies only the b-jet efficiency has been remeasured with Run 2 data, the other two use extrapolated measurements from Run 1. An uncertainty is also introduced to cover this extrapolation from Run 1 to Run 2.

5.7.2 Modelling Uncertainties

The other set of uncertainties is the errors related to the theoretical modelling of the processes involved in the search. This includes both the modelling of the signal process and of the background processes. As the search is performed through a template likelihood fit and the majority of the shape and normalisation information which is used as input to this fit comes from the modelling of the processes in Monte Carlo these uncertainties can have a large effect on the sensitivity of the analysis.

t$\bar{\text{t}}$H Uncertainties

Two uncertainties on the normalisation of the t$\bar{\text{t}}$H signal are introduced to the fit derived during the calculation of the NLO theoretical cross section [72–76]. The two uncertainties are those from the scale and the PDF and are treated as uncorrelated. The combined uncertainty on the cross section from these two uncertainties is $^{+6.8\%}_{-9.9\%}$. Furthermore three uncertainties are introduced due to the uncertainty on the Higgs branching ratios, split into those from the uncertainty on the branching ratio of H $\rightarrow$ b$\bar{\text{b}}$, H $\rightarrow$ WW and H $\rightarrow$ others. Due to the purity of the selection of H $\rightarrow$ b$\bar{\text{b}}$ this is the dominant of the three uncertainties with a value of $^{+1.2\%}_{-1.3\%}$.

There are also four uncertainties introduced to account for the choice of Monte Carlo generator. Three of these are from the choice of parton shower and hadronisation model split into the three Higgs boson decay modes mentioned before. This uncertainty is derived from the comparison of the predicted distributions from the default Monte Carlo generation used as discussed in Section 5.4 (MadGraph5_aMC@NLO interfaced to Pythia 8.2.10) with the prediction from MadGraph5_aMC@NLO interfaced with

Herwig++. The fourth of these uncertainties comes from the variation of the QCD scale chosen in the default simulation derived by varying the renormalisation and factorisation scales simultaneously to half their value and double their value for the down and up variations provided to the fit, respectively.

t$\bar{\text{t}}$ + Jets Uncertainties

The t$\bar{\text{t}}$ + Jets background dominates the number of expected events in the most signal rich regions. As such, great care has been taken to ensure the best possible modelling of this background is achieved and the uncertainties on it are properly quantified. The resulting set of uncertainties is comprised of three normalisation uncertainties and 24 shape and normalisation uncertainties across all three samples in t$\bar{\text{t}}$ + Jets.

Four sources of uncertainty are applied across all three samples: the cross section uncertainty and three sources of uncertainty due to the selection of Monte Carlo generator. The cross section uncertainty comes from the theoretical cross section calculated at NNLO+NNLL which is assumed to have a value of $^{+6\%}_{-6\%}$, accounting for all sources of uncertainty in the calculation. This uncertainty is fully correlated across all three samples. The next three sources of uncertainty are fully uncorrelated across the three samples meaning there are nine nuisance parameters associated with the three uncertainties. The settings used for the generation of the samples used for these comparisons is summarised in Table 5.13. The three sources of uncertainty are: the uncertainty on the event generation, quantified by comparing the Powheg-Box interfaced to Herwig++ sample with the MadGraph5_aMC@NLO interfaced to Pythia 6.4.28 sample; the uncertainty on the parton shower and hadronisation model used, quantified by comparing the default sample (Powheg-Box interfaced to Pythia 6.4.28) with the Powheg-Box interfaced to Herwig++ sample; and the uncertainty on the choice of radiation settings in the parton shower, quantified by comparing the default sample with samples with adjusted renormalisation scale, factorisation scale, h_{damp} parameter, and the parton shower tune as can be seen in the table.

In the case of the t$\bar{\text{t}}$ + ≥1b sample the alternate Monte Carlo samples are corrected to the NLO Sherpa prediction in the same way the default sample is corrected before the comparison is made. The comparisons evaluating the uncertainty on the event generation, and parton shower and hadronisation model used use Monte Carlo samples utilising the fast simulation of the ATLAS detector. Also due to the low cross section in signal rich regions a technique called Tag Rate Function (TRF) is used to help

Table 5.13: Summary of the settings used for the simulation of the inclusive t$\bar{\text{t}}$ samples. For the renormalisation and factorisation scales, $p_{\text{T,t}}$ ($p_{\text{T},\bar{\text{t}}}$) denotes the transverse momentum of the top (anti-top) quark in the t$\bar{\text{t}}$ centre-of-mass reference frame and m_{t} denotes the top mass. All samples use the CT10 PDF set for the ME and the CTEQ6L1 PDF set for the PS [7].

Generator	Renormalisation scale	Factorisation scale	h_{damp}	Tune
Powheg-Box Pythia 6.4.28	$\sqrt{m_{\text{t}}^2 + p_{\text{T,t}}^2}$	$\sqrt{m_{\text{t}}^2 + p_{\text{T,t}}^2}$	m_{t}	P2012
Powheg-Box Herwig++	$\sqrt{m_{\text{t}}^2 + p_{\text{T,t}}^2}$	$\sqrt{m_{\text{t}}^2 + p_{\text{T,t}}^2}$	m_{t}	UE-EE5
MG5_aMC Herwig++	$\sqrt{m_{\text{t}}^2 + \frac{1}{2}(p_{\text{T,t}}^2 + p_{\text{T},\bar{\text{t}}}^2)}$	$\sqrt{m_{\text{t}}^2 + \frac{1}{2}(p_{\text{T,t}}^2 + p_{\text{T},\bar{\text{t}}}^2)}$	–	UE-EE5
Powheg-Box Pythia 6.4.28	$\frac{1}{2} \cdot \sqrt{m_{\text{t}}^2 + p_{\text{T,t}}^2}$	$\frac{1}{2} \cdot \sqrt{m_{\text{t}}^2 + p_{\text{T,t}}^2}$	$2 \cdot m_{\text{t}}$	P2012 radHi
Powheg-Box Pythia 6.4.28	$2 \cdot \sqrt{m_{\text{t}}^2 + p_{\text{T,t}}^2}$	$2 \cdot \sqrt{m_{\text{t}}^2 + p_{\text{T,t}}^2}$	m_{t}	P2012 radLo

prevent excessive statistical fluctuations with a moderately sized sample of simulated events. TRF is a technique in which events are no longer categorised by the number of b-tags they have. Instead, weights are applied depending on which category is currently being considered. The weights are defined based on the kinematics of the jets and the value of the multivariate classifier used to tag them. The weight gives the probability of the event to contain the desired number of b-jets.

The next two sources of uncertainty considered are the uncertainties due to the correction of the t$\bar{\text{t}}$ + light and t$\bar{\text{t}}$ + $\geq$1c events to the NNLO prediction discussed in Section 5.4.2. These uncertainties are quantified by taking the largest difference between the NNLO prediction for these two distributions and the predictions from the Monte Carlo generators detailed in Table 5.13. These uncertainties are taken as fully decorrelated across the two samples meaning these uncertainties introduced four nuisance parameters between them.

A final uncertainty on the t$\bar{\text{t}}$ + $\geq$1c background is considered due to the use of the parton shower model for producing the additional c-quarks as opposed to them being produced directly in the matrix element calculation. To quantify this uncertainty a dedicated NLO Monte Carlo sample was generated using MadGraph5_aMC@NLO interfaced to Herwig++ with the extra c-quarks generated in the matrix element

calculation. This was then compared to an inclusive t$\bar{\text{t}}$ sample produced with the same Monte Carlo generator and the difference is taken as the uncertainty.

The treatment of the t$\bar{\text{t}}$ + ≥1b background is more complex than the other samples in t$\bar{\text{t}}$ + Jets and as such there are another ten sources of uncertainty considered for the t$\bar{\text{t}}$ + ≥1b background. A collection of uncertainties related to the NLO prediction are considered. Three separate variations of the renormalisation, factorisation and resummation scales are compared to the default generator. An uncertainty on the choice of underlying event tune in the Sherpa sample is quantified by varying parameters in the event tune up and down. The uncertainties from the choice of parton distribution function are quantified by comparing the default CT10 with predictions from NNPDF and MSTW [115]. The uncertainty from the choice of shower recoil scheme is quantified by comparing the default prediction with that from an alternate scheme. The uncertainty from the choice of NLO generator is quantified by comparing the prediction from Sherpa with that from MadGraph5_aMC@NLO interfaced to Pythia 8.2.10. The uncertainty from the choice of parton shower and hadronisation model is quantified by the comparison of MadGraph5_aMC@NLO interfaced to either Pythia 8.2.10 or Herwig++. Finally an uncertainty on the prediction of the production from multi-parton interactions, which is not included in the Sherpa prediction is considered with a normalisation uncertainty of ±50%.

In Table 5.1 it can be seen that there is a deficit in the production of t$\bar{\text{t}}$ + HF events which heavily influences the signal enriched regions. This observation is compatible with the prediction given the large uncertainties associated with the production [116, 117]. This observation could bias the fit by using the previously described uncertainties to artificially increase the rate of production of the t$\bar{\text{t}}$ + HF processes and in the process change the shape of the distributions used. To prevent this two normalisation uncertainties are introduced, one for the t$\bar{\text{t}}$ + ≥1c sample and one for the t$\bar{\text{t}}$ + ≥1b sample. These uncertainties are unlike all the other uncertainties in the analysis in that no constraint is associated with the nuisance parameter in the definition of the likelihood (described in Section 5.2), meaning they are free to take the value which gives the best agreement between data and prediction.

t$\bar{\text{t}}$ + V Uncertainties

As with the signal modelling the uncertainties from the t$\bar{\text{t}}$ + V background come from both the theoretical calculation of the cross section and from the choice of the Monte

Carlo generator used for the default sample. For each of these uncertainties there are separate uncertainties for t$\bar{\text{t}}$ + W and t$\bar{\text{t}}$ + Z which are treated as uncorrelated.

The cross section uncertainty for each process is taken from its NLO theoretical cross section and, as with the signal cross section uncertainty, is separated into the uncertainty due to the scale choice and that due to the use of PDF, which are treated as uncorrelated. The uncertainties due to the scale choice has a value of $^{+12.9\%}_{-11.5\%}$ for t$\bar{\text{t}}$ + W and $^{+9.6\%}_{-11.3\%}$ for t$\bar{\text{t}}$ + Z and the uncertainty due to the PDF scale has a value of $^{+3.4\%}_{-3.4\%}$ for t$\bar{\text{t}}$ + W and $^{+4.0\%}_{-4.0\%}$ for t$\bar{\text{t}}$ + Z.

The uncertainty due to the choice of Monte Carlo generator is evaluated by comparing the default sample used with the output of using Monte Carlo data generated with MadGraph5_aMC@NLO in leading order mode with the same choice of parton shower and hadronisation model of Pythia 8.2.10.

Single top Uncertainties

The only single top channel which contributes 'real' events to the analysis is the Wt channel so only systematics related to this sample are considered. Uncertainties are introduced on the cross section of the sample, the use of the diagram removal scheme and the choice of Monte Carlo generator. The cross section uncertainty is taken to be $^{+5\%}_{-5\%}$, estimated from the uncertainty on the theoretical measurement [97–99].

The uncertainty on the use of the diagram removal scheme is assessed by comparing the prediction using this scheme with the prediction from the use of the diagram subtraction scheme [96].

The uncertainties from the choice of Monte Carlo generator are handled as two uncertainties, one on the choice of parton shower and hadronisation model and the other from the choice of the radiation settings in the default parton shower model. The uncertainty caused by the choice of parton shower and hadronisation is evaluated by comparing the default prediction (Powheg-Box interfaced to Pythia 6.4.28) to that generated using Powheg-Box interfaced to Herwig++. The uncertainty caused by the choice of radiation settings in the parton shower is evaluated by comparing two dedicated simulation samples produced with changed parameters designed to decrease and increase the amount of initial and final state radiation respectively. The settings for the three Monte Carlo samples used for these systematics are produced in the same way as their corresponding t$\bar{\text{t}}$ samples, the settings of which are shown in Table 5.13.

The detector simulation used for these three samples is the fast simulation, to ensure a fair comparison with the default sample a dedicated version of the default sample is produced using the fast simulation.

Z + Jets Uncertainties

The uncertainties on the Z + Jets channel are all normalisation based uncertainties. There are two from the Z + Jets cross section and three from the correction based on the number of heavy flavour truth jets observed in the event. The uncertainty on the cross section is decorrelated in regions with different numbers of reconstructed jets leading to two uncertainties (3 jets and $\geq$ 4 jets), each with a value of $^{+30\%}_{-30\%}$. This value is based on variations of the scales and matching parameters in the Sherpa Monte Carlo.

Similarly the uncertainty from the correction based on the number of heavy flavour truth jets observed in the event is decorrelated in regions with different numbers of b-tags (2, 3 and $\geq$ 4 b-tagged jets), and is quantified by taking the difference between the events seen with the correction to those without. This systematic is implemented as having a shape as the Z + Jets sample is not separated into the different number of heavy flavour truth jet categories but is intended only as a simultaneous normalisation correction on each category.

Diboson Uncertainties

Only one uncertainty on the diboson production is considered from the cross section of the process. This uncertainty includes the inclusive cross-section uncertainty and that on additional jet production, the value used is $^{+50\%}_{-50\%}$.

tH Uncertainties

Two uncertainties are considered for each of the two tH production mechanisms arising from the choice of the scale and the PDF in the cross-section calculation. For the tHbj channel the combination of the two uncertainties gives a total $^{+7.5\%}_{-15\%}$ uncertainty on the cross section. For the tWH channel each uncertainty is taken to be $^{+20\%}_{-20\%}$.

Fake Lepton Uncertainties

A correction on the yield in the fake lepton background is evaluated by comparing the fake lepton prediction with data with same sign leptons as described in Section 5.6.2. An uncertainty is introduced on the yield such that the uncorrected yield is within the value of the uncertainty. As such a $^{+50\%}_{-50\%}$ uncertainty is used for the normalisation.

5.8 Results

The fit is performed first on the dilepton channel and then a combined fit is performed with the single-lepton channel including both analyses analysis regions in the likelihood. The single-lepton analysis follows a very similar approach to the dilepton analysis using nine equivalently defined analysis regions. The only significant difference in the analyses other than the difference in final state considered, is the treatment of the fake lepton background. It is estimated from a purely data driven method in the single lepton analysis; details of this analysis can be found in [7]. In the combined fit all experimental and modelling systematics which affect both the single-lepton and dilepton fit are correlated and share nuisance parameters.

The input distributions to the fit, along with the distributions after the combined single-lepton and dilepton fit has been performed showing the effect of the fit on the different samples in the different regions, can be seen in Figures 5.10 to 5.12. It can be seen that the agreement between the prediction and data is much improved by the fit and the uncertainties on the prediction are greatly reduced. The fitted value for the t$\bar{\text{t}}$ + $\geq$1b normalisation is $1.33^{+0.18\%}_{-0.17\%}$ and the fitted value for the t$\bar{\text{t}}$ + $\geq$1c normalisation is $1.31^{+0.53\%}_{-0.40\%}$. A summary of all these regions, along with all the regions in the single-lepton analysis is presented in Figure 5.13 in which all bins which enter the combined fit are ordered by the logarithm of the ratio of signal to background predicted for that bin.

The sources of systematic uncertainties are listed in the order of their influence on the uncertainty on the signal strength parameter in Table 5.14. These sources are each groups of many nuisance parameters separated into groups with similar sources. This table gives insight into the main limitations on the sensitivity of the search showing that already with the limited dataset available at the start of Run 2 the systematic uncertainty is larger than the statistical uncertainty which indicates improvements in

Figure 5.10: Comparison of the data and prediction before (left) and after (right) performing the combined single-lepton and dilepton fit. Shown are the H_T^{all} distributions in the $(3j, 2b)$ (top) and $(3j, 3b)$ (bottom) analysis regions which entered the fit. The t$\bar{\text{t}}$H distribution (solid) is normalised to the SM predicted cross section before the fit and to the best-fit cross section after the fit (from [7]).
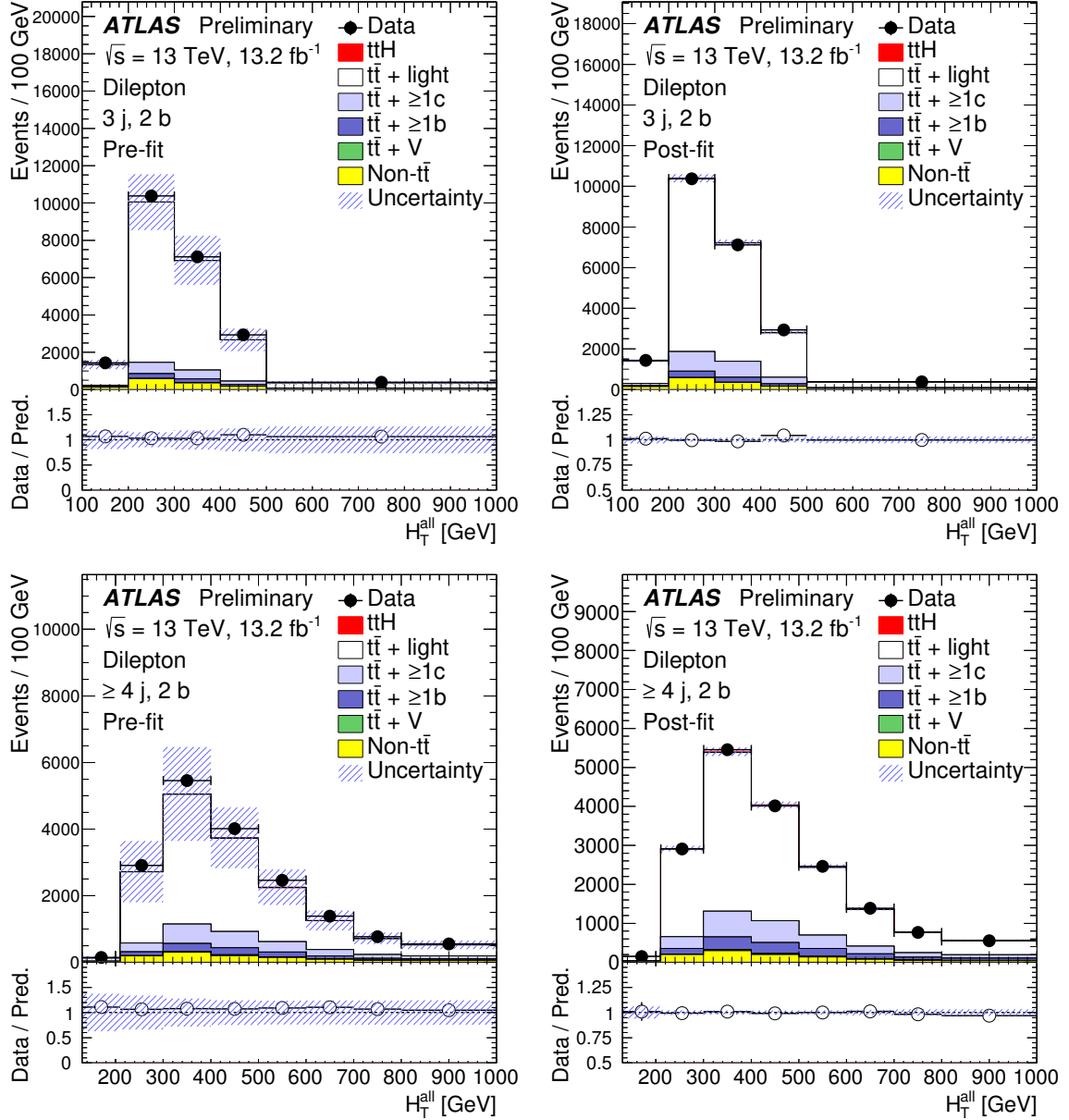
Figure 5.11: Comparison of the data and prediction before (left) and after (right) performing the combined single-lepton and dilepton fit. Shown is the neural network output in the (3j, 3b) analysis region (top), and the boosted decision tree output in the (≥4j, 3b) analysis region (bottom), which both entered the fit. The t̄tH distribution (solid) is normalised to the SM predicted cross section before the fit and to the best-fit cross section after the fit. The dashed line shows the t̄tH distribution normalised to the total yield (from [7]).
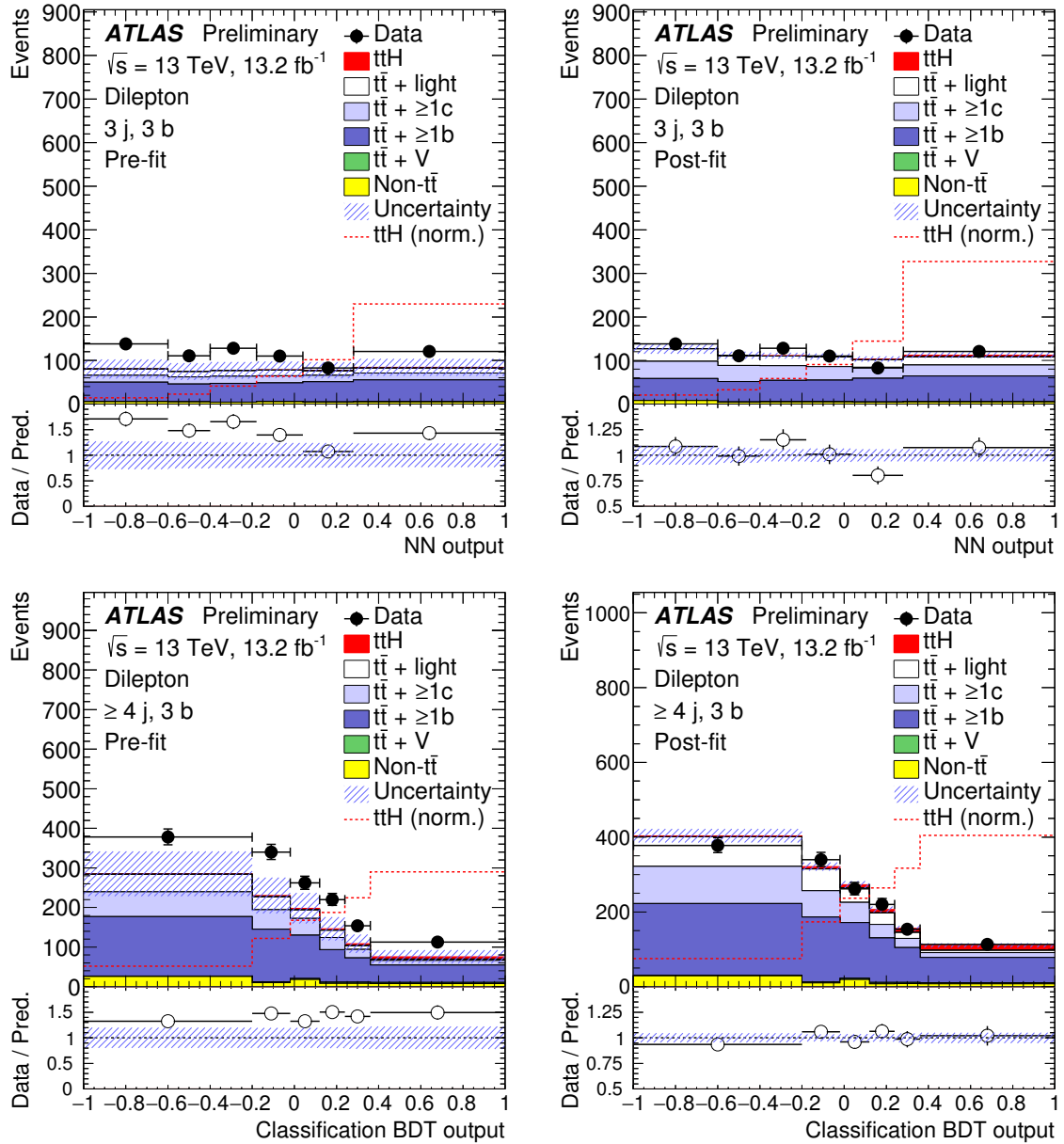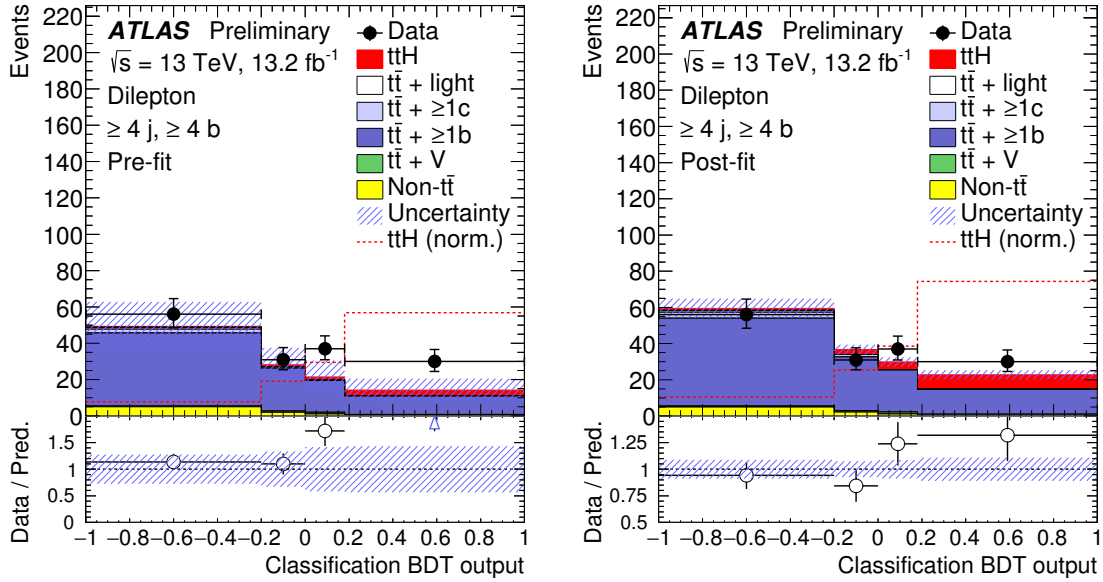
Figure 5.12: Comparison of the data and prediction before (left) and after (right) performing the combined single-lepton and dilepton fit. Shown is the boosted decision tree output in the ($\geq$4j, $\geq$4b) analysis region, which entered the fit. The t$\bar{\text{t}}$H distribution (solid) is normalised to the SM predicted cross section before the fit and to the best-fit cross section after the fit. The dashed line shows the t$\bar{\text{t}}$H distribution normalised to the total yield (from [7]).
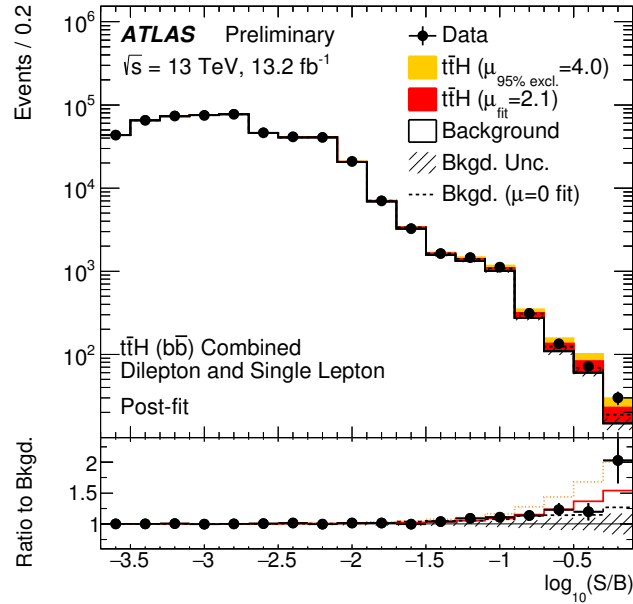

Figure 5.13: Comparison of the data and prediction after the combined single-lepton and dilepton is performed for all bins from the distributions contributing to the fit ordered by log(S/B). The signal is shown normalised to the best-fit cross section and to the excluded value. The result of a fit performed with the signal cross section fixed at zero is also shown (from [7]).

Table 5.14: Summary of the effects of the systematic uncertainties on the signal strength parameter (μ) after the combined single-lepton and dilepton fit. The uncertainties on the cross-section and normalisation of processes are included in the modelling sources unless otherwise mentioned. The background model statistics refers to the statistical uncertainties from the limited number of simulated events and from the data-driven determination of the fake lepton background in the single-lepton channel. Due to correlations between the different sources of uncertainties, the total systematic uncertainty can be different in magnitude and symmetry from the sum in quadrature of the individual sources. The normalisation factors for both $t\bar{t} + \geq 1b$ and $t\bar{t} + \geq 1c$ are included in the statistical component (from [7]).

Uncertainty source	$\Delta\mu$	
$t\bar{t} + \geq 1b$ modelling	$+0.53$	-0.53
Jet flavour tagging	$+0.26$	-0.26
$t\bar{t}H$ modelling	$+0.32$	-0.20
Background model statistics	$+0.25$	-0.25
$t\bar{t} + \geq 1c$ modelling	$+0.24$	-0.23
Jet energy scale and resolution	$+0.19$	-0.19
$t\bar{t} + $ light modelling	$+0.19$	-0.18
Other background modelling	$+0.18$	-0.18
Jet-vertex association and pileup modelling	$+0.12$	-0.12
Luminosity	$+0.12$	-0.12
$t\bar{t} + Z$ modelling	$+0.06$	-0.06
Lepton trigger and reconstruction	$+0.05$	-0.05
Total systematic uncertainty	$+0.90$	-0.75
$t\bar{t} + \geq 1b$ normalisation	$+0.34$	-0.34
$t\bar{t} + \geq 1c$ normalisation	$+0.14$	-0.14
Statistical uncertainty	$+0.49$	-0.49
Total uncertainty	$+1.02$	-0.89

the signal sensitivity will come slowly with increased data and is limited mainly by other factors.

The systematic uncertainty with the largest effect on the signal sensitivity is the modelling of the dominant $t\bar{t} + \geq 1b$ background. This result is a preliminary result, the first result for the search for $t\bar{t}H$ utilising proton collisions at 13 TeV from ATLAS. As such this systematic was calculated in a conservative manner, which should be able
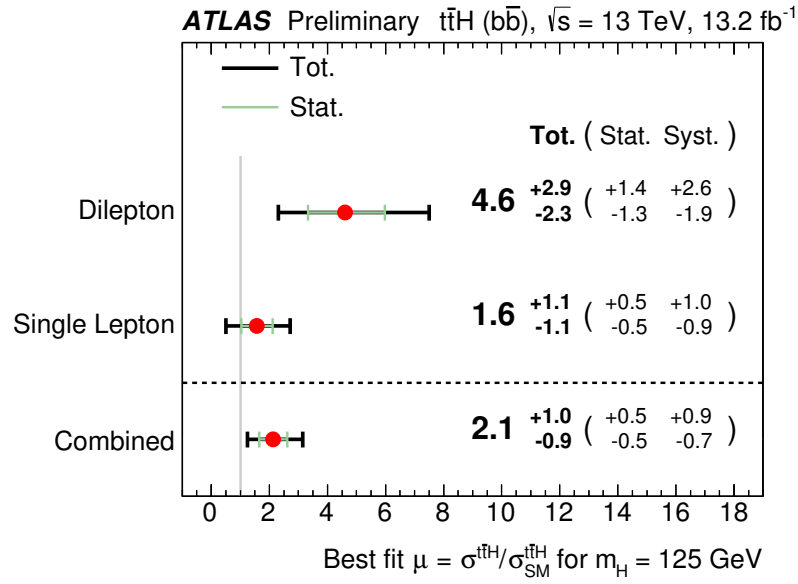
Figure 5.14: Summary of the measured signal strength in the individual single-lepton and dilepton fits along with the measured strength in the combined fit (from [7]).

to be improved with a more thorough consideration and through the use of newer Monte Carlo generators. The next most significant sources of uncertainty are the jet flavour tagging uncertainties, the modelling of tt̄H events, the limited number of generated Monte Carlo events, and the modelling of tt̄ + ≥1c events.

The observed signal strength from the dilepton data is found to be $4.6^{+2.9}_{-2.3}$, when combined with the single-lepton data the value is found to be $2.1^{+1.0}_{-0.9}$, as can be seen in Figure 5.14. This signal strength corresponds to a significance of 2.4 standard deviations away from the Standard Model expectation without the presence of the tt̄H vertex, assuming the signal is produced at the Standard Model predicted rate a significance of 1.8 was expected. This is a mild excess which does not provide sufficient evidence for the discovery of process, as such limits on the production cross section are derived. A 95% confidence limit on the signal strength parameter is set with values greater than 10.1 disfavoured for the dilepton channel alone and values greater than 4.0 disfavoured when combined with the single-lepton channel, this is summarised in Figure 5.15.
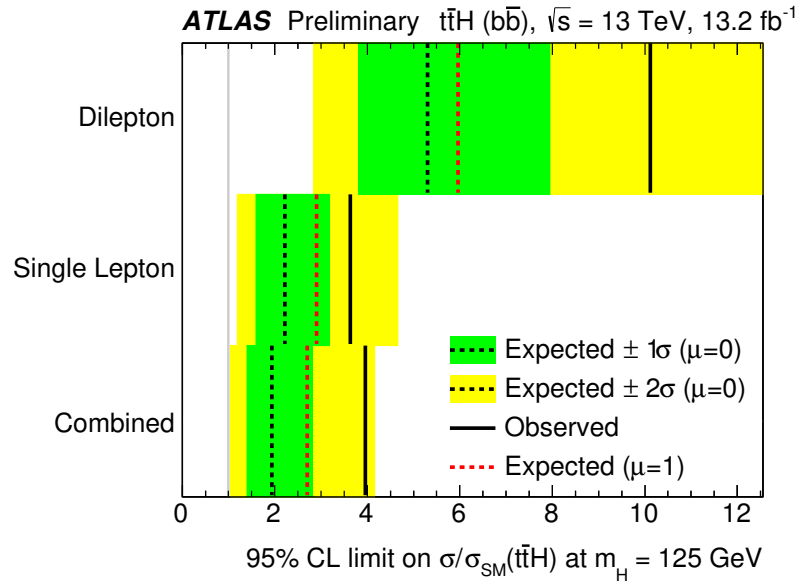
Figure 5.15: Summary of the measured 95% confidence level upper limits on the $t\bar{t}H$ cross-section compared to the predicted values for both the background-only and signal hypotheses. The limits from individual single-lepton and dilepton fits along with the limit from the combined fit are shown (from [7]).

Chapter 6

Novel Techniques to Improve Signal Sensitivity

This chapter details two studies performed attempting to improve the signal sensitivity of the analysis presented in the previous chapter. In Section 6.1 the first of the two studies is documented in which the inclusion of variables correlated with the quality of measurement of an event are considered for inclusion as input to the multivariate classifiers used in the analysis. The second study in Section 6.2 investigates the inclusion of the jet pull angle as a measure of the colour connection between jets in the analysis, both to improve the multivariate classifier and the multivariate reconstruction.

6.1 Event Quality Variables

Event quality variables refer to variables which are correlated with how well measured an event is and as such can be used to separate high quality events from low quality ones. In this section the use of such variables in an analysis is motivated through a toy model in Section 6.1.1. Candidate variables used in the analysis presented in this thesis are selected in Section 6.1.2, and the means of testing their success is explained in Section 6.1.3. Finally the results of including the variable in the multivariate classifier are presented in Section 6.1.4 and the prospects for future work are detailed in Section 6.1.5.

6.1.1 Motivation

In the analysis presented in this thesis and many other analyses performed within ATLAS and beyond the selection of variables to be used in a multivariate classifier follows a fixed procedure. A large collection of candidate variables is produced. These include properties of the individual reconstructed objects in the event (for example the transverse momentum of the jet with the largest transverse momentum) and variables that give information on the shape of the decay products (for example the centrality[1] of the event).

Then for each of these variables the distribution is produced for the background processes and the signal process in order to select a smaller collection of variables with which to train the classifier. In the analysis presented in this thesis, the difference between these two distributions is quantified using the separation defined as

$$S = \frac{1}{2} \cdot \sum_{i \in \text{bin}} \frac{\left(N_i^{\text{signal}} - N_i^{\text{background}} \right)^2}{\left(N_i^{\text{signal}} + N_i^{\text{background}} \right)}. \tag{6.1}$$

Along with the separation for each variable sometimes the correlation between variables is considered so as to prevent the use of variables using the same information, which would appear as highly correlated variables. Once these two pieces of information are collected, a short list of variables is assembled consisting of those with the highest individual separation. Some of these may be removed due to high correlation. This process is typically done by hand meaning the criteria for selection contains subjective input. This short list is then used to train the classifier and further reduction of variables is performed by comparison of the performance of the trained classifier with different inputs. This process of selecting variables means only variables which individually have large separation between signal and background are selected, variables with little or no separation are discarded.

Event quality variables quantify the quality with which the objects in an event were measured on an object-by-object, or event-by-event basis. As these variables are based on the measurement of the objects themselves, not the source of the objects, they are not expected to differ in distribution between the signal process and the background processes and so would be discarded during the variable selection process mentioned

---

[1]Centrality is defined as the sum of the transverse momenta of the objects in an event divided by the sum of their energy.

above. For example a variable that is correlated to the quality of measurement of a jet would be identical for all jets, both signal and background jets.

To demonstrate the utility of event quality variables the following example is given based on [118]. Consider a signal and background each of which produce Gaussian distributions for a given variable (x_1) with different means (μ_s and μ_b respectively) and the same width. The width is dependent on the value of a second variable (x_2), which follows an exponential distribution as summarised in Equations (6.2) to (6.4).

$$
\begin{aligned}
f(x_1, x_2 | \mathrm{s}) &= \mathrm{Gaus}(x_1; \mu_s, \sigma(x_2)) \cdot \mathrm{Exp}(x_2; \lambda) \\
&= \frac{1}{\sqrt{2\pi}\sigma(x_2)} e^{\frac{-(x_1 - \mu_s)^2}{2(\sigma(x_2)^2)}} \cdot \frac{1}{\lambda} e^{\frac{-x_2}{\lambda}}
\end{aligned}
\tag{6.2}
$$

$$
\begin{aligned}
f(x_1, x_2 | \mathrm{b}) &= \mathrm{Gaus}(x_1; \mu_b, \sigma(x_2)) \cdot \mathrm{Exp}(x_2; \lambda) \\
&= \frac{1}{\sqrt{2\pi}\sigma(x_2)} e^{\frac{-(x_1 - \mu_b)^2}{2(\sigma(x_2)^2)}} \cdot \frac{1}{\lambda} e^{\frac{-x_2}{\lambda}}
\end{aligned}
\tag{6.3}
$$

$$
\begin{aligned}
\sigma(x_2) &= \mathrm{Exp}(x_2; \zeta) \\
&= \sigma_0 e^{\frac{-x_2}{\zeta}}
\end{aligned}
\tag{6.4}
$$

A large number of simulated events following these distributions has been produced and the distribution of these can be seen in Figure 6.1. It can be seen in the plots that the variable x_2 can be considered an event quality variable correlating to the accuracy with which x_1 has been measured. In this instance it can be considered that the mean of the Gaussians are the true values of x_1 for the signal and background and the width is the error in the measurement. It is also clear that with the above strategy for variable selection for use in a multivariate classifier x_1 would be utilised as it shows good separation between the signal and background processes and x_2 would be discarded due to a lack of separating power.

The purpose of the multivariate classifier is to take a collection of variables and combine them into a single test statistic which can be used to separate the processes to an arbitrary purity at the expense of efficiency. The Neyman-Pearson lemma [119] states that the optimal test statistic for distinguishing between two hypotheses is determined by taking the ratio of the likelihood of an event occurring under each hypothesis. As such an optimal test statistic, $t(x_1, x_2)$, for this problem can be
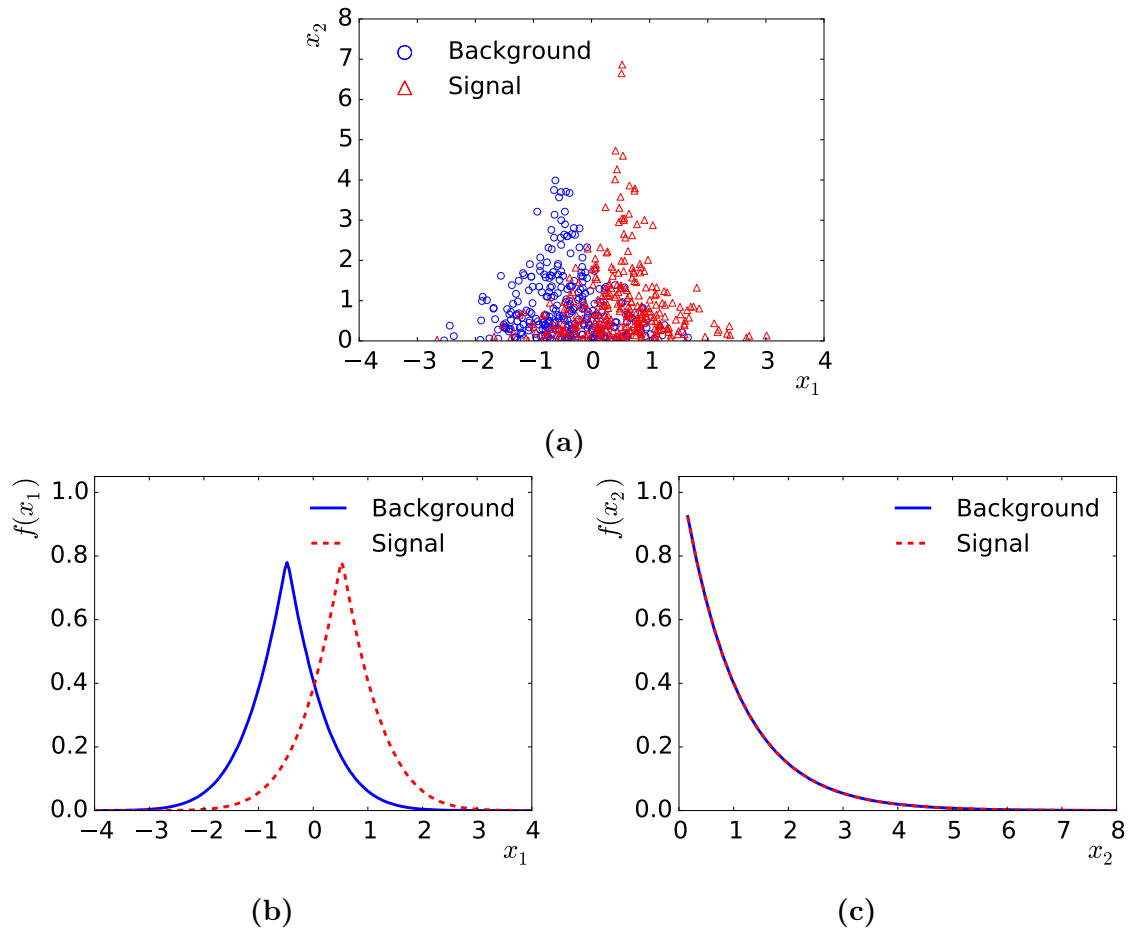
(a)

(b)

(c)

Figure 6.1: Plots showing example distributions as used in the toy example for (a) x_2 plotted against x_1 and the normalised distribution of events over (b) x_1 and (c) x_2 for signal and background.
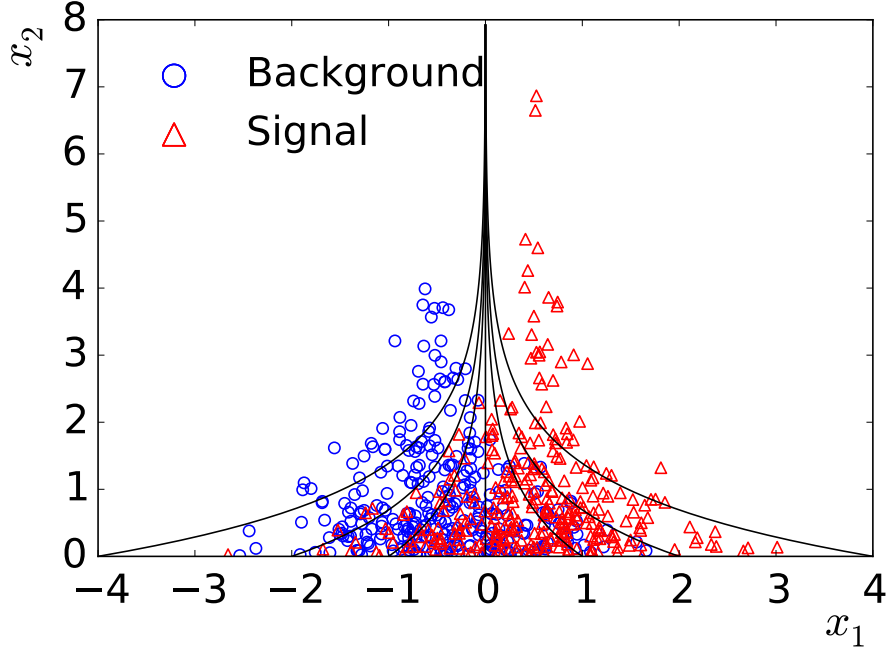
Figure 6.2: Example contours of the exact likelihood ratio given in Equation (6.6) super-imposed on example events.

obtained as

$$t(x_1, x_2) = \frac{f(x_1, x_2|\text{s})}{f(x_1, x_2|\text{b})}.$$ (6.5)

The power of a test statistic is maintained under any monotonic transformation. Therefore, an equivalent test statistic can be constructed from the natural logarithm of this test statistic as given by

$$\ln t = \frac{\frac{1}{2}\left(\mu_b^2 - \mu_s^2\right) + \left(\mu_s - \mu_b\right)x_1}{\sigma_0^2 e^{\frac{-2x_2}{\zeta}}}.$$ (6.6)

Here it can be seen that the optimal test statistic to separate the signal and background hypotheses has a dependence not only on x_1 as would be used in the typical variable selection but also on x_2. This is further illustrated by overlaying lines of fixed t on the scatter plot previously considered as shown in Figure 6.2.

This dependence on x_2 shows a clear utility in the use of event quality variables in the training of the most optimal multivariate classifiers. In this section such variables are searched for to improve the performance of the classifier used in the analysis presented.

6.1.2 Selection of Variables

The effectiveness of the addition of event quality variables is dependent on how wide a distribution of quality there exists between different events. In Table 5.14 the effect of the uncertainties in the analysis on the sensitivity to the process of interest can be seen. Here it can be seen that the two largest measurement uncertainties arise from the identification of jets originating from b-mesons and the measurement of the jet energy scale and resolution. The other measurements' uncertainties (those related to the measurement of the leptons in the analysis) have a very small relative effect.

In the case of identifying the source of jets there is a powerful variable that could be utilised to quantify the quality of measurement, namely the output of the flavour tagging classifier. This variable would give much more detailed information than just binary jet tag currently used in the analysis. However, as this is the output of a multivariate classifier extensive work needs to be performed to ensure the performance is understood and it is correctly modelled for the entire range. Due to the complexity of the validation process, the group within ATLAS who derive and validate this information have only managed to perform the verification and calibration of this variable for a number of fixed working points. Furthermore only one of these working points can be used simultaneously. There is work in the collaboration to extend this further to utilise this powerful variable but that is beyond the scope of this thesis.

This then leaves the measurement of the jet energy scale and resolution as the largest measurement uncertainty. An event quality variable related to this uncertainty is expected to make use of knowledge of differences in the detector geometry and the measurement capabilities of the different sub-detectors used to measure the jet.

The variables used to assess the quality of jets during the jet reconstruction and selection are considered for this purpose and are documented in [106]. In order for the variables to provide significant improvement to the performance it is expected that the variables should take on a broad range of values for the different jets providing a range of levels of quality which can be exploited. Furthermore it is desirable that the jets are well distributed in the quality variable as if the vast majority take only one or two values then the variable will only have limited discriminating power. Using these criteria two variables have been selected as candidate jet quality variables to be used to improve the performance of the classifier.
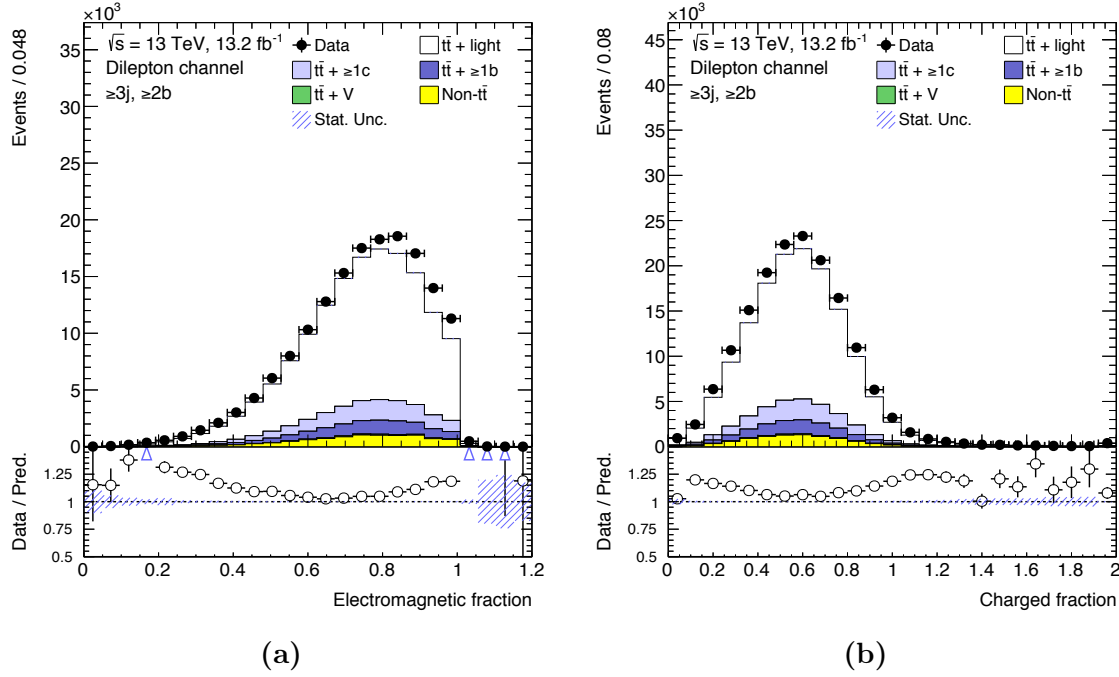
Figure 6.3: Distributions of (a) the electromagnetic fraction and (b) the charged fraction for all jets after the full analysis selection has been performed for both data and simulation.

First is the electromagnetic fraction, which is defined as as the ratio of the energy deposited in the electromagnetic calorimeter to the total energy of the jet. The distribution can be seen in Figure 6.3a. This variable is expected to be correlated to the quality of measurement of the jets as the error on the measurement of energy with the electromagnetic calorimeter is smaller than that with the hadronic calorimeter. This means jets with a larger proportion of the energy measured in the electromagnetic calorimeter will be measured more accurately.

The second variable considered is the charged fraction, which is defined as the ratio of the sum of the transverse momentum of the tracks associated to the jet divided by the calibrated transverse momentum of the jet. The distribution can be seen in Figure 6.3b. This variable is expected to take advantage of the same information as the electromagnetic fraction as charged particles hadrons are measured with a greater uncertainty than the photons from neutral pion decays.

6.1.3 Validation Studies

Truth information from the Monte Carlo simulation is utilised in order to verify that the variables selected for the study correlate to how well the energy of the jets are measured. First the jets considered are matched to truth jets (jets made from particles produced in the parton shower) by considering their separation in (η, ϕ) space[2]. Owing to inefficiencies in the detector and the spread of the particles energy when measured, the jets reconstructed from the truth particles do not necessarily have a one-to-one correlation with the jets reconstructed in the detector. Reconstructed jets are considered in descending order of their transverse momentum and matched to the closest truth jet in (η, ϕ) space up to a maximum separation of $\Delta R = 0.4$. Over 99% of the reconstructed jets are successfully matched to a truth jet using using this method. The jets which are not successfully matched to a truth jet are not considered during this validation procedure.

A variable is constructed from the paired reconstructed and truth jets in order to determine the quality of the measurement. The variable chosen is the difference between the energy of the reconstructed jet and the energy of the truth jet ($E_{\text{reco}}^{\text{jet}} - E_{\text{true}}^{\text{jet}}$). In order to verify the candidate jet quality variable correlates with the quality of measurement the correlation with the test variable should not be considered as this is expected to always be zero for an unbiased measurement (the jet calibration procedure attempts to remove bias from the jet energy measurement). Instead the width of this distribution should be considered to see how often the measured value is close to the true value and how often it differs by a large amount. This is quantified by considering the root mean squared (RMS) distribution of the test variable as a function of the candidate jet quality variable.

The distributions of the RMS is shown for each of the candidate event quality variables in Figure 6.4. In the case of the electromagnetic fraction there is a clear slope in the distribution with the better measured jets falling at higher values of the electromagnetic fraction, as was expected. The charged fraction has a larger variation in the quality of measurement, however the majority of the jets are found in the region $0.3 <$ Charged Fraction < 0.9 where the distribution is nearly flat, just the extreme values differ indicating poor measurement. These results indicate the two candidate variables provide information on the quality of the measurement of the jets. As such

---

[2]The distance is measured as $\Delta R = \sqrt{(\Delta\phi)^2 + (\Delta\eta)^2}$
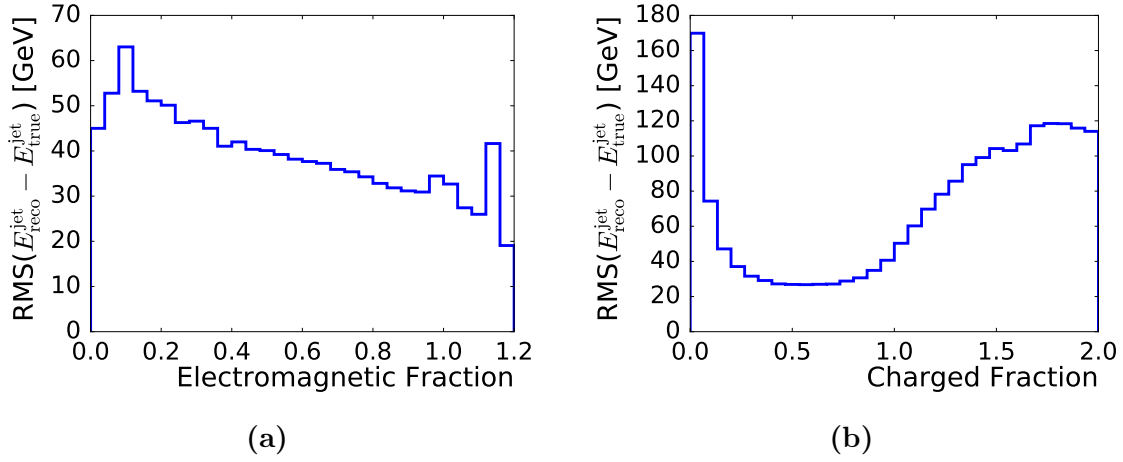
Figure 6.4: A plot of the RMS values of $E_{\text{reco}}^{\text{jet}} - E_{\text{true}}^{\text{jet}}$ as a function of (a) the electromagnetic fraction and (b) the charged fraction for all truth matched jets in simulated $t\bar{t}H$ and $t\bar{t}$ events.

the variables have been added to the analysis in the multivariate classifier used in the signal enriched regions to separate signal from background.

6.1.4 Results

The candidate jet quality variables are introduced to the multivariate classification algorithm used in the analysis in the $(\geq 4\text{j}, 3\text{b})$ and $(\geq 4\text{j}, \geq 4\text{b})$ regions. In these regions a boosted decision tree [120, 121] is used to separate the signal from the background. It is trained using the predicted $t\bar{t}H$ events for the signal and the predicted $t\bar{t}$ + Jets events for the background as this background dominates in this region so is a good approximation of the total background.

The jet quality variables are added to the classifier by providing the values of the quality variable for the four leading jets and for the jets associated to b-quarks from the Higgs boson and the top quark decays by the multivariate reconstruction. Trainings are performed using the same settings for the classification algorithm as those used in the analysis and a training with only the variables used in the analysis is done to compare the performance. Three total trainings are performed:

1. A training identical to the one used in the analysis,

2. A training with the variables related to the electromagnetic fraction added,

3. A training with the variables related to the charged fraction added.

The classifiers produced for the second and third trainings are shown in Figure 6.5, along with the Receiver Operating Characteristic (ROC) curve for the three trainings shown overlaid. The ROC curve is a plot of the background rejection efficiency versus the signal acceptance efficiency; the closer the line is to the top right corner the better the classifier performs at separating the signal and background.

When developing the classifiers analyses typically use a number of measures to quantify the quality of the classifier. The two used in the optimisation of the multivariate classifiers in this analysis are:

- The separation of the signal and background distributions defined in Equation (6.1)

- The area under the ROC curve

The first of these two methods can give inconsistent values depending on the exact choice of binning used, as such the area under the ROC curve will be used to assess the quality of the outputs in this thesis. The values for the area under the ROC curve are given in Table 6.1 for each of the trainings in the two regions. Note these values are calculated by averaging over the values obtained for five separate trainings, each trained on 80% of the data and tested on the remaining 20% such that no two values use the same event for testing. The error is the standard deviation of the five values.

It can be seen from the table and the plots of the distributions no significant improvement in separation is made from the addition of the candidate jet quality variables with any changes in the area under the ROC curve being smaller than the associated error. The small errors show that the algorithm manages to achieve a stable result with the training set giving confidence that the result is due to the lack of significant improvement in the classifier data and not due to problems with the classification algorithm.

6.1.5 Conclusion and Outlook

The candidate event quality variables selected by considering variables related to the quality of the jets did not have any significant improvement to the separation achieved by the multivariate classifier. The lack of improvement achieved shows only that the variables selected were not effective, the motivation for the incorporation of event quality variables into the classifier is unaffected. For this technique to be adopted
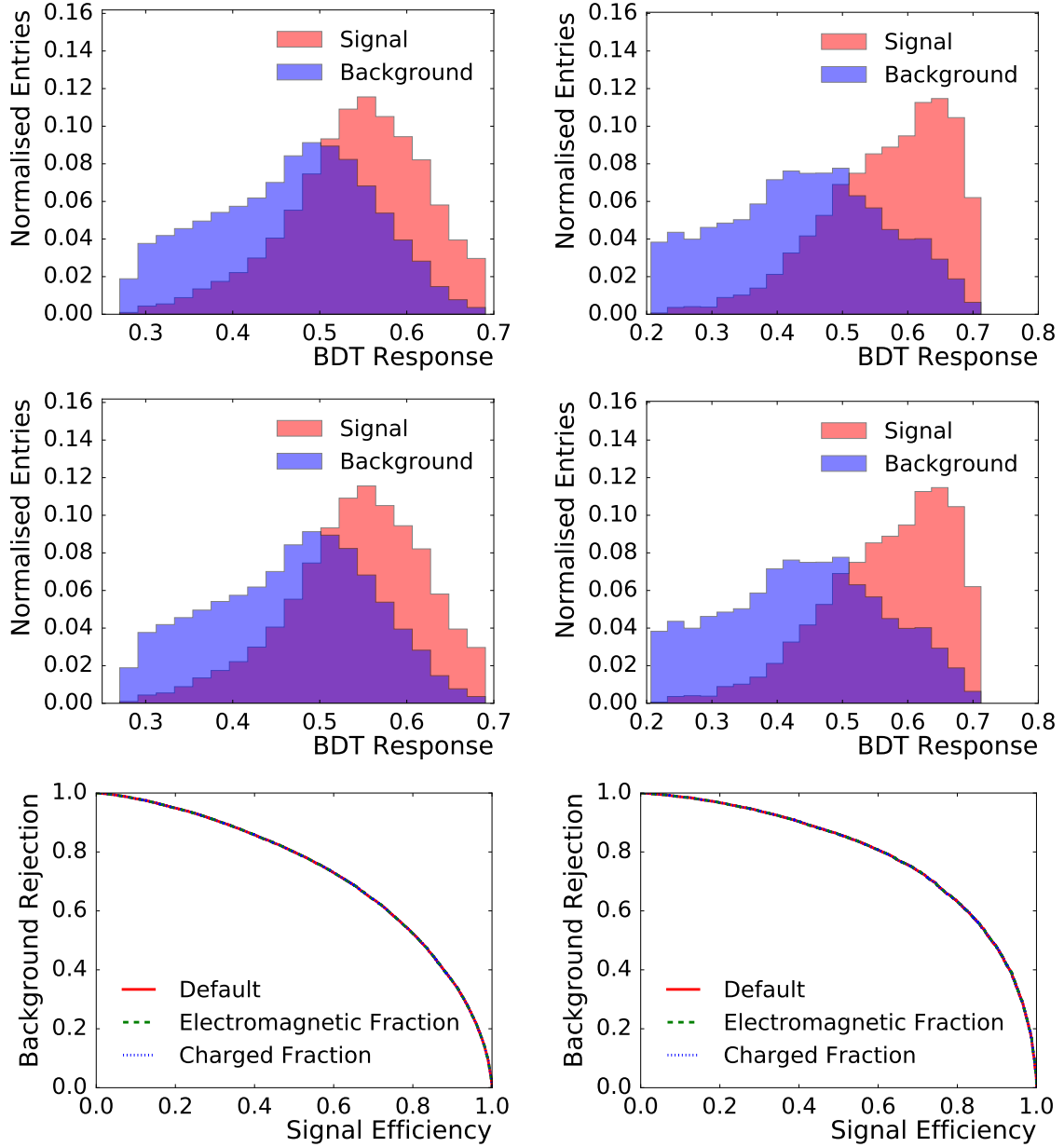
Figure 6.5: Output from the training of the multivariate classifiers with candidate jet quality variables. The trainings are performed in the (left) ($\geq$4j, 3b) and (right) ($\geq$4j, $\geq$4b) regions. The classifier output is shown for (top) the added electromagnetic fraction variables and (middle) the added charged fraction variables. The ROC curves are shown (bottom) in each region for all three trainings, note due to a lack of improvement in the classifier the three lines can not be distinguished.

Table 6.1: Summary of area under the ROC curve for the different trainings with and without the candidate jet quality variables in the two different regions.

| Training | Area under the ROC curve | |
	$(\geq 4j, 3b)$	$(\geq 4j, \geq 4b)$
Default	0.7289 ± 0.0049	0.7734 ± 0.0089
Electromagnetic Fraction	0.7290 ± 0.0049	0.7734 ± 0.0089
Charged Fraction	0.7288 ± 0.0048	0.7734 ± 0.0089

into the analysis further study is required to select variables which correlate to the quality of the measurement of the event. Any candidate variables selected for this purpose can be tested in the same way as was established in this section to verify their suitability for use.

6.2 Colour Flow Variables

Colour flow variables are variables which relate to the way the colour charges propagated during the particle interactions. This is measured by looking for jets originating from quarks with opposite colour charge by considering their jet pulls, and specifically the angle between the jet pull and the line connecting the pair of jets. The motivation for including variables of this type along with a more thorough description of the variables can be found in Section 6.2.1. The selection of the exact variables to be used to improve the signal sensitivity is described in Section 6.2.2. The results of including these variables in the multivariate algorithms is documented in Section 6.2.3. Finally the outlook for further work on colour flow variables is described in Section 6.2.4.

6.2.1 Motivation

The performance of the analysis presented in this thesis is dictated in part by the ability to separate events with a signal like topology from those with a background like topology. This separation is achieved through the use of a multivariate classifier into which a number of variables are input. These variables contain information about the number of jets, their transverse momenta and their relative locations in the detector along with similar information about the leptons and variables built from the combination of these properties. The classifier also uses information from the output
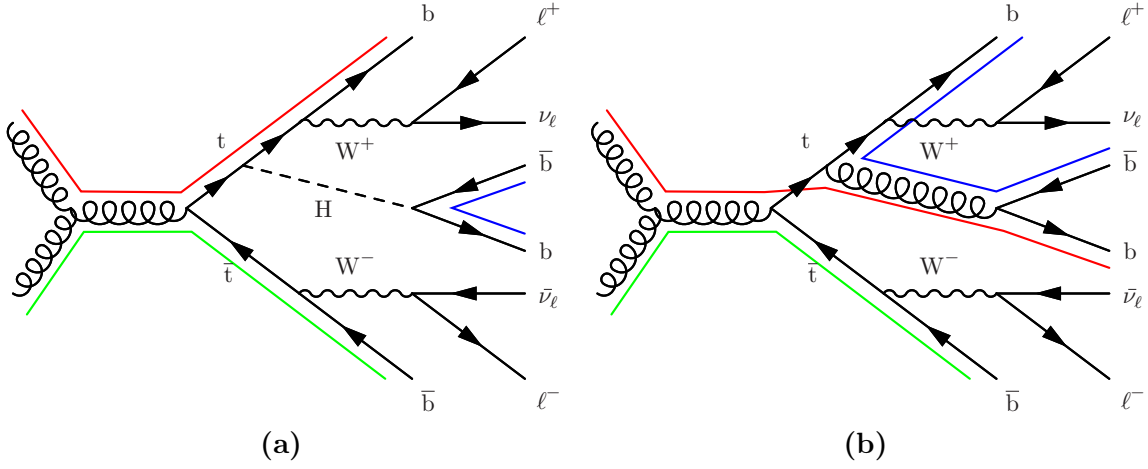
Figure 6.6: Diagrams illustrating the colour connections present in (a) the signal and (b) the $t\bar{t} + {\geq}1b$ background for an example tree level process. Note the line connecting the gluons from the protons is omitted.

of a secondary multivariate classifier which aims to find the most likely pairing of the reconstructed objects to the leptons and quarks in the signal process and derived information related to this.

All these variables are made by simply taking the four-momenta of the reconstructed objects and combining them in different ways. While this produces a classifier which gives good discrimination between the signal and background processes it leaves much of the information collected by the detector unused or only used indirectly. One such source of information comes from the distribution of particles found within the jets from which a quantity known as the jet pull, and subsequently the jet pull angle [122] can be derived.

The jet pull angle can be used to infer the degree of colour connection between jets in the detector, information that is previously unused. Colour connection is a means of describing the radiation pattern in QCD by modelling the connection between coloured objects through the use of colour strings. The colour strings connect a coloured object to an object with the corresponding anti-colour. When the particles reach sufficient separation these colour strings break producing particles along their length which can be observed in the detector. In Figure 6.6 the propagation of the colour charges has been visualised using coloured lines for example Feynman diagrams for the signal and the predominant background processes, the ends of which show which objects are connected by colour strings.

The breaking of the colour strings between coloured objects means an increase in the amount of radiation in the space between the two objects is expected to be seen. There are a number of ways of quantifying this information but this section will focus on the jet pull angle. The jet pull angle looks only at the distribution of the particles which make up the jet not the particles outside of the jets. During the jet reconstruction, tracks which fall within the region of the jet defined by the clustering in the calorimeter are associated to that jet. From these tracks the two-dimensional jet pull vector $(\vec{v}_p^J)$ can be defined as

$$\vec{v}_p^J = \sum_{i \in J} \frac{p_T^i |\vec{r}_i|}{p_T^J} \vec{r}_i, \tag{6.7}$$

where i denotes the tracks within jet J, p_T^i (p_T^J) denotes the transverse momenta of the track (jet) and $\vec{r}_i$ denotes the position of the track relative to the jet axis in $(y, \phi)^3$ space (from [122]).

From the jet pull vector the jet pull angle can then be defined, which is the angle between the jet pull vector and the line connecting the jet to a second jet in (y, ϕ) space as shown in Figure 6.7. This angle is expected to be small for colour connected jets since the breaking of the colour string between the jets causes increased radiation in that plane which will fall on one edge of the jet. Since the pull vector is weighted by not only the transverse momentum of the tracks but also the squared distance between the radiation and the jet axis even a small amount of extra radiation from the colour string can heavily influence the pull vector. The use of this variable has previously been shown effective in an ATLAS measurement of the colour connection between the jets coming from the W boson in $t\bar{t}$ events [123].

6.2.2 Selection of Variables

In the signal rich regions of the analysis there are a large number of jets (at least four jets in the two with the highest signal purity) and when considered in ordered pairs of jets (the definition of the pull angle means $\theta_p^{1,2} \neq \theta_p^{2,1}$) this number increases still. This makes it challenging to construct a variable, or set of variables using these properties which will provide information to the multivariate classifier. In Figure 6.6

---

[3]In this section the direction y is used to represent the rapidity of the object defined as $y = 0.5 \log\left(\frac{E+p_z}{E+p_z}\right)$ where E (p_z) denotes the energy (z-component of the momentum) of the object.
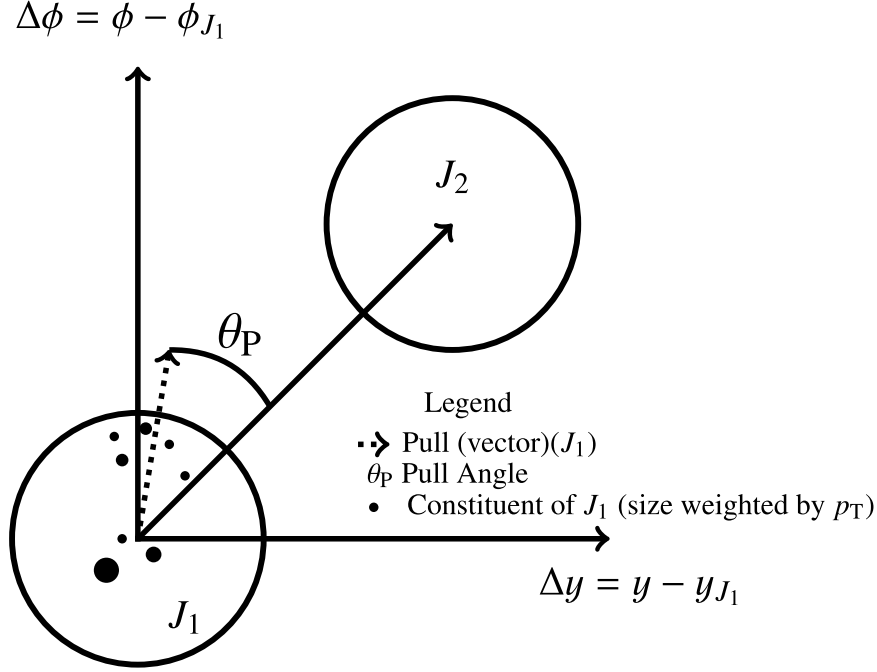
Figure 6.7: Diagram illustrating the definition of the jet pull angle from the jet J_1 to the jet J_2 (from [123]).

it can be seen that the colour connections between the jets are different for the signal and background processes and it is this difference that can be utilised to separate them.

The difference between the two options for these diagrams is not in what reconstructed objects are connected but in the source of those objects[4]. In the signal process the two b-quarks from the Higgs boson are connected to each other and isolated from the rest of the event and the two b-quarks from the top quarks are connected to the proton remnants.

It can be verified that the jet pull angle corresponds to the qualitative picture previously described as can be seen in Figure 6.8a in which the pull angle between colour connected and colour isolated jets is compared. The colour connected and isolated jets are selecting by matching the reconstructed jets to the particles form the decay of the objects in the truth record. The colour connected jets are selected by associating the jets with the b-quarks from the decay of the Higgs boson whereas the colour isolated jets are selected: one associated with a b-quark from the Higgs

---

[4]Note, other diagrams can be drawn such that all the final state b-quarks are colour connected to the protons remnants for the background process, which is more readily distinguished.
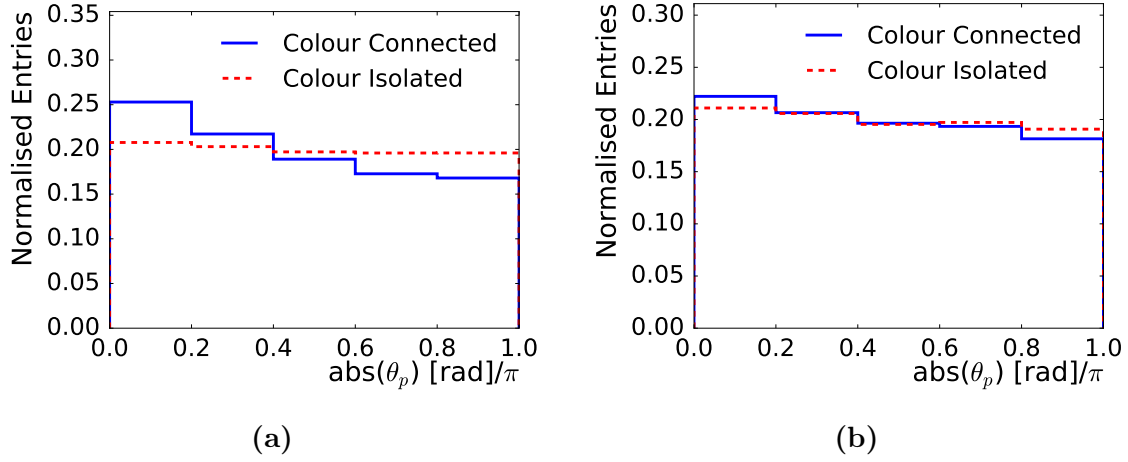
Figure 6.8: A comparison of the jet pull angle between a pair of colour connected jets, chosen as the jets from the decay of the Higgs boson, and colour isolated jets, chosen as a jet from the decay of the Higgs boson and a jet from the decay of the top quark. The jets were chosen (a) using Monte Carlo truth information and (b) using the output from the multivariate reconstruction algorithm.

boson decay, the other associated with the b-quark from the top quark decay. This separation can still be seen, although reduced due to selection inefficiencies, when looking at the pull angles between the same jets but selected using the multivariate reconstruction algorithm instead of truth information as in Figure 6.8b.

As such during classification training all variables of this sort, pull angles between each pair of reconstructed objects (the b-quarks from the Higgs-boson and top-quark decays) are introduced to the algorithm. Along with these variables a collection of other variables are defined:

- the magnitude of the jet pull for each of the objects from the reconstruction algorithm

- the number of tracks used during the calculation of the jet pulls for each of the objects from the reconstruction algorithm

- the sum of jet pulls for all jets in the event

- the average of jet pulls for all jets in the event

- the average of jet pulls from all jets not associated with the Higgs boson from each of the objects from the reconstruction algorithm

Table 6.2: Summary of area under the ROC curve for the different trainings with and without the candidate jet pull angle variables in the two different regions for both the multivariate classification and reconstruction algorithms.

Training	Area under the ROC curve	
	$(\geq 4j, 3b)$	$(\geq 4j, \geq 4b)$
Default	0.7289 ± 0.0049	0.7734 ± 0.0089
Pull Angle	0.7290 ± 0.0049	0.7733 ± 0.0089

- the minimum and maximum values of the jet pull in the y and ϕ direction for all jets in the event

- the pull angles for the nearest and furthest pairs of jets in η and (η,ϕ) space

All of these variables are used during the classification training since there is no expected loss of performance of a boosted decision tree classifier with an increased number of variables.

The use of this information to improve the performance of the multivariate reconstruction algorithm is also attempted. In this case the only variables added to the algorithm are the pull angles between each permutation of the jets assigned to the decay objects. None of the other defined variables above are used since all variables used in the training of the reconstruction algorithm are functions of pairs of the reconstructed objects.

6.2.3 Results

Classification

The training of the multivariate classifier proceeds in the same manner as in Section 6.1.4, except in this case there are only two classifiers trained. The default classifier is once again trained with the same settings and variables as those used in the analysis and the pull angle classifier is trained with the added variables described in the previous section.

The results of this training can be seen in Figure 6.9 along with the values for the area under the ROC curve in Table 6.2. There is no significant improvement seen when adding the jet pull angle variables to the multivariate classifier with the area
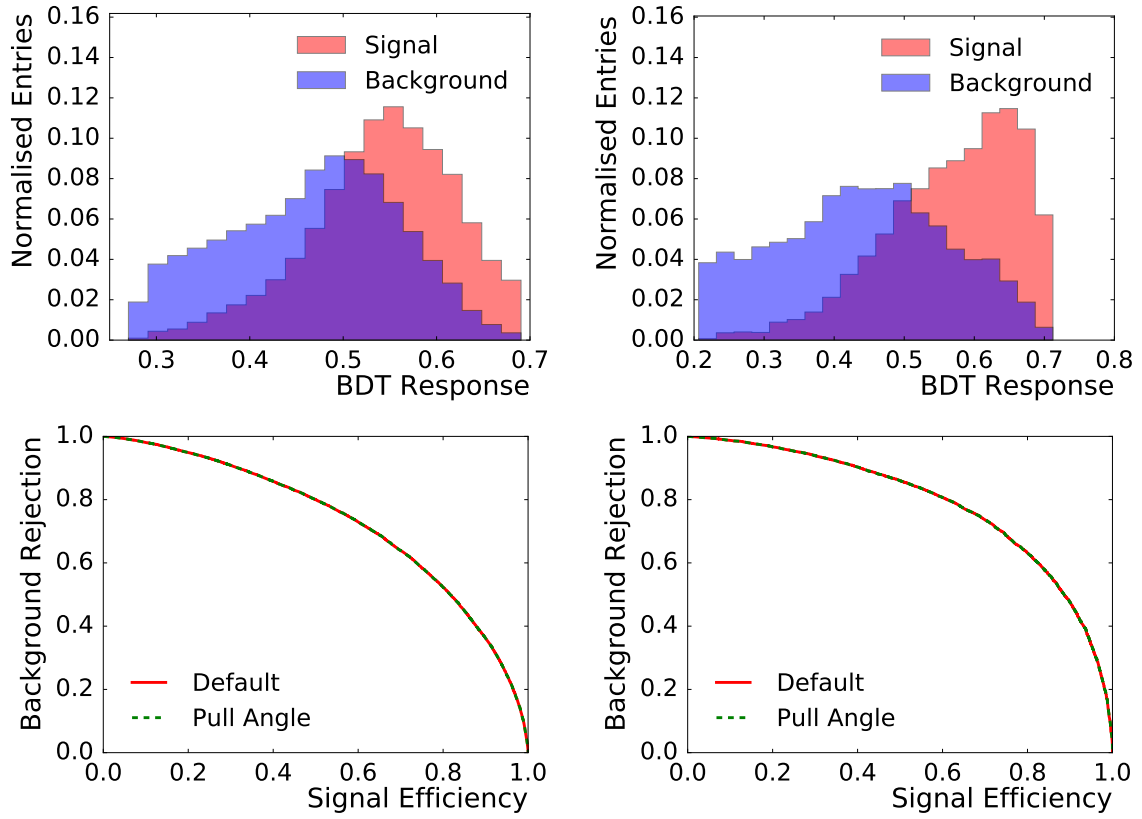
Figure 6.9: Output from the training of the multivariate classifiers with candidate jet pull angle variables. The trainings are performed in the (left) ($\geq$4j, 3b) and (right) ($\geq$4j, $\geq$4b) regions. The classifier output is shown (top) for the added jet pull angle variables and the ROC curves are shown (bottom) in each region for both trainings, note due to a lack of improvement in the classifier the two lines can not be distinguished.

under the ROC curve of the two trainings being within the error on the value for both regions.

Reconstruction

The variables related to jet pull angle were added to the multivariate reconstruction algorithm as described above. The way in which the quality of the reconstruction algorithm is assessed is different to the classification algorithm as optimal reconstruction does not need large separation between the signal and background distributions coming from the algorithm but should correctly match the reconstructed objects to the source of these objects. As such the efficiency of the reconstruction is considered for the trained algorithms. The efficiency is calculated using a sample which only contains events in which the Higgs boson decayed into b-quarks so as to remove events which can not be correctly matched. Next the efficiency of matching the reconstructed objects to the truth particles from the decay of the top quarks and the Higgs boson is assessed as if no object was reconstructed for a given particle the algorithm can not correctly match the jets. Finally the truth matched objects are compared to the reconstructed objects to assess the efficiency of the reconstruction.

The efficiency of both truth matching the objects and then reconstructing the object correctly can be seen in Figure 6.10. No improvement is seen from the reconstruction algorithm used in the analysis. While separation between the correct assignment of jets to the objects from the incorrect assignment is visible using the jet pull angle variables they are strongly correlated with variables such as the physical separation of the jets in the detector. As such the jet pull angle variables are not used in the final reconstruction algorithm.

6.2.4 Conclusion and Outlook

The jet pull angle, as a measure of the colour connection between jets, was added to the input variables for the multivariate classification and reconstruction algorithms used in the analysis. The algorithms when trained with the jet pull angle variables did not have significantly better performance than those used without the jet pull angle variables. The lack of improvement is likely due to the high correlation between the jet pull angle variables and other variables used as input to the algorithms and
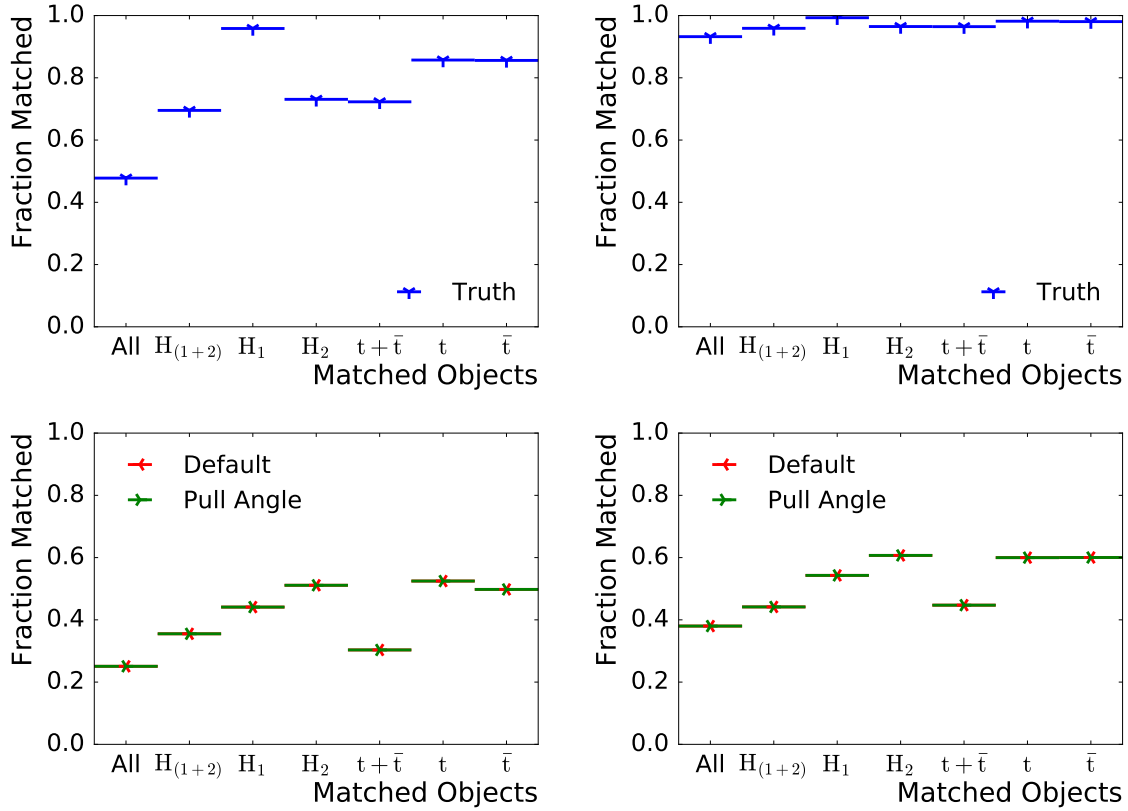
Figure 6.10: Efficiency of the multivariate reconstruction algorithm at matching the b-jets to the correct b-hadrons from the top-quark and Higgs-boson decays. The two decay products from the Higgs boson are labelled $H_1(H_2)$ for the leading (subleading) decay particle and the decay products from the top quarks are labelled as the top from which they originate. The trainings are performed in the (left) ($\geq$4j, 3b) and (right) ($\geq$4j, $\geq$4b) regions. The efficiency with which the jets can be matched to the true objects is shown (top) and the efficiency of the reconstruction of the objects relative to the efficiency of the true reconstruction is shown (bottom) for trainings with and without the added jet pull angle variables.

because the effect of the colour connection between the jets is a smaller effect than the basic kinematic properties of the events.

While jet pull angles were not successful in improving the signal sensitivity in the analysis the use of variables related to the colour connection between the jets could still be useful. Other techniques for extracting information related to the colour connection of jets, such as the inter-jet particle flow (in which all particle produced in the region between two jets are considered, even those produced outside the jet areas) could still provide improvement to the analysis. These other variables could be more sensitive to the effects of the colour connection due to the fact they utilise more information in the detector than the pull angle, which is restricted to signals within the jet.

Furthermore the jet pull angle could be improved by consideration of not only the distribution of tracks in the jet but also the distribution of the signals in the calorimeter. In the previous ATLAS analysis [123] looking at jet pull angles it was found that using only tracks was more efficient than only calorimeter information, which was the justification for the use of tracks in this study. Instead of considering the two separately a possible improvement to the jet pull angles could be achieved by considering both the tracks and calorimeter information through the application of techniques such as particle flow jets which where pioneered in the ALEPH experiment at LEP [124]. When constructing particle flow jets the energy from well measured tracks is first subtracted from the calorimeter such that the clustering algorithm can use a combination of the tracks and clusters to build the jets without considering the same information twice. This would give the accuracy of the tracks with the added information from the clusters, potentially giving more accurate jet pulls which would provide better separation between colour connected jets and those which are not.

Chapter 7

Conclusions and Outlook

This chapter summarises the conclusions from the work presented in this thesis, which can be found in Section 7.1. Next the combination of the $t\bar{t}H(H \to b\bar{b})$ result with the $t\bar{t}H$ analysis targeting decays of the Higgs boson to leptons and the $t\bar{t}H$ analysis targeting decays of the Higgs boson to photons is documented in Section 7.2. Finally an outlook on the future for $t\bar{t}H$ searches is provided in Section 7.3.

7.1 Conclusions

This thesis has presented a search for $t\bar{t}H(H \to b\bar{b})$ with the top quarks decaying leptonically along with two studies attempting to improve the signal sensitivity of this search.

The search was carried out using $13.2\,\mathrm{fb}^{-1}$ of proton-proton collision data at $\sqrt{s} = 13$ TeV collected by the ATLAS experiment at the LHC. No significant evidence for $t\bar{t}H(H \to b\bar{b})$ for was found with a best fit signal strength parameter found to be $\mu = 4.6^{+1.4}_{-1.3}(\mathrm{stat})^{+2.6}_{-1.9}(\mathrm{syst})$. Since no significant evidence was found a 95% confidence limit was set on the signal strength parameter disfavouring values higher than 10.1. The combination with the single lepton channel was also presented. A combined best fit signal strength parameter was found to be $\mu = 2.1^{+0.5}_{-0.5}(\mathrm{stat})^{+0.9}_{-0.7}(\mathrm{syst})$. This is also insufficient to be classed as significant evidence, as such a 95% confidence limit is put on the signal strength parameter with values above 4.0 disfavoured.

Studies were presented showing the inclusion of event quality variables into the multivariate classifier used in the analysis and the inclusion of colour flow variables into both the multivariate classifier and multivariate reconstruction algorithms in the

analysis. For both sets of variables no significant improvement to the performance of the algorithms was seen.

7.2 Full ATLAS t$\bar{\text{t}}$H Combination

Alongside the t$\bar{\text{t}}$H(H $\rightarrow$ b$\bar{\text{b}}$) analysis, on which the author was involved, other analyses were taking place targeting t$\bar{\text{t}}$H events with different Higgs boson decay modes [125, 126]. Note due to the complexities in correctly predicting the background distributions and the low sensitivity to the signal no fully hadronic analysis has been performed in Run 2 at this time. The completed analyses were combined into a single t$\bar{\text{t}}$H search in ATLAS, the result of which was presented alongside the individual channel results at ICHEP 2016 [127]. The results of this combination can be seen in Figure 7.1. It can be seen that the best fit signal strength parameter in the combined fit is found to be $\mu = 1.8^{+0.4}_{-0.4}(\text{stat})^{+0.6}_{-0.5}(\text{syst})$. This is an improvement on the result presented using the Run 1 data but is still not significant enough to be classified as evidence of t$\bar{\text{t}}$H. A 95% confidence limit on the signal strength parameter is set with values above 3.0 disfavoured.

7.3 Outlook

It is an exciting time to be searching for a t$\bar{\text{t}}$H signal assuming that t$\bar{\text{t}}$H occurs at the Standard Model predicted rate. Since the completion of this analysis, the ATLAS experiment has collected another 22.9 fb^{-1} of 13 TeV up to the end of 2016. Furthermore the LHC is expected to deliver as many, if not more, proton-proton collisions in 2017 as were recorded in 2016 leading to more than 70 fb^{-1} of data being collected in Run 2 by the end of 2017. This over fivefold increase in data from the result presented in this thesis to the end of 2017 gives a good chance of a t$\bar{\text{t}}$H discovery.

A simple extrapolation of the fit used in the full combination presented in the previous section to the dataset collected by the end of 2016 leads to an expected significance of t$\bar{\text{t}}$H of a little less than 3σ and an extrapolation to a 100 fb^{-1} dataset would give a significance a little less than 5σ. These extrapolations assume that the analysis strategy would remain the same and the uncertainties would not change.
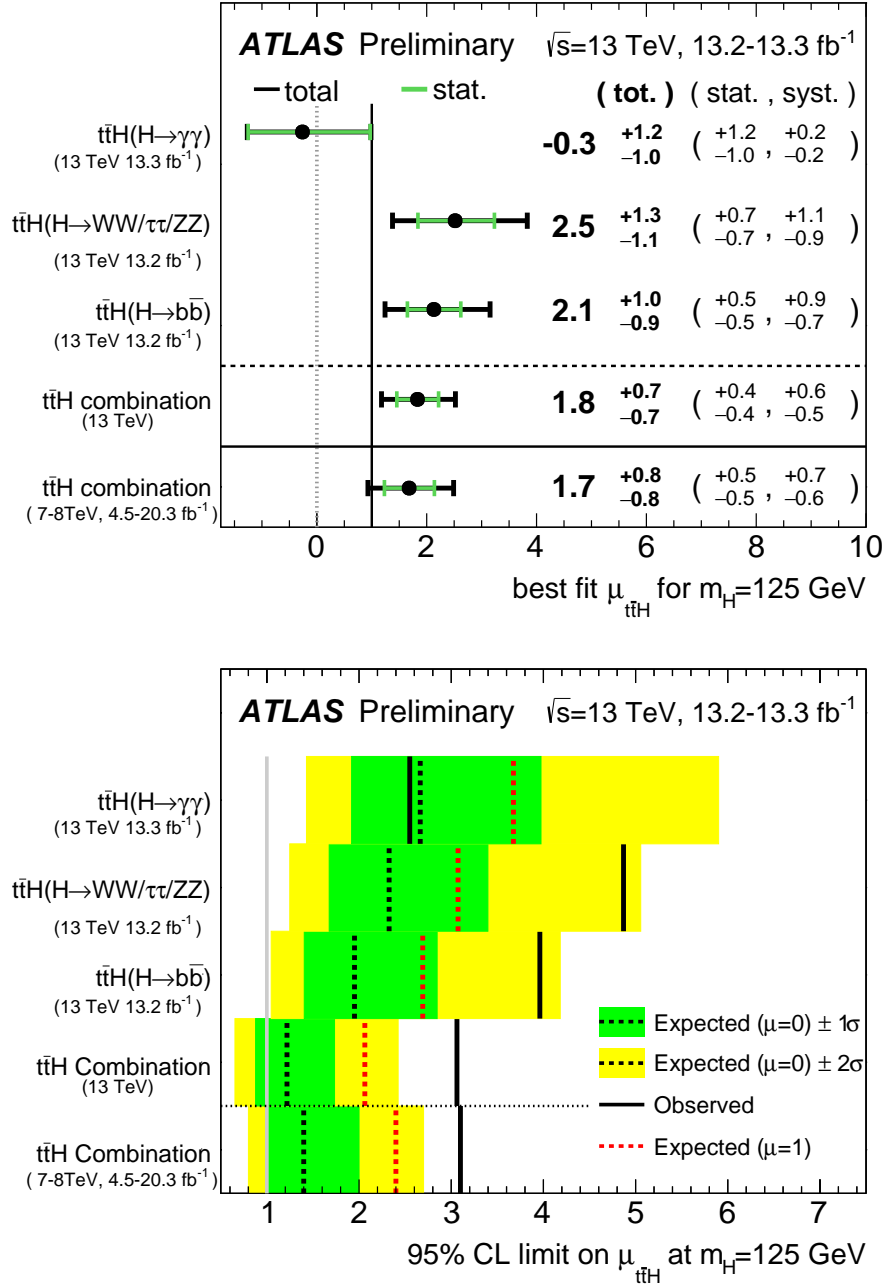
Figure 7.1: Summary of (top) the best fit signal strength parameters and (bottom) the 95% upper limit on signal strength for each $t\bar{t}H$ analysis performed in ATLAS and the combination and the Run 1 result for comparison (from [127]).

There are a number of improvements expected in the analyses from the result presented here and the extrapolated results mentioned, which could give enough added sensitivity to have evidence for and then a discovery of $t\bar{t}H$. The improvements to the analysis include the use of a b-tagging algorithm that provides multiple working points simultaneously. This would allow a greater number of regions to be constructed in the analysis which can be used to further separate the signal from the background and new regions to be defined targeting specific backgrounds providing stronger constraints on their related uncertainties. Furthermore new advancements in the Monte Carlo generators have become available with newer version of the generating software than was used in this analysis. These could lead to smaller uncertainties on the modelling of the $t\bar{t} + \geq 1b$ background that provided the largest uncertainty to the $t\bar{t}H(H \rightarrow b\bar{b})$ analysis.

The improvements in the analysis and the extra data expected from the LHC all point to a bright future for $t\bar{t}H$ discovery. Beyond Run 2, the LHC will be upgraded to a higher luminosity machine with which a much larger dataset is expected to be collected. With this larger dataset the $t\bar{t}H$ process can be measured in detail and can be used to set limits on the top Yukawa coupling constraining the Standard Model and probing for processes beyond the Standard Model.

Bibliography

[1]   The ATLAS Collaboration, *Observation of a new particle in the search for the Standard Model Higgs boson with the ATLAS detector at the LHC*, Physics Letters B 716.1 (2012), pp. 1–29, DOI: 10.1016/j.physletb.2012.08.020

[2]   CMS Collaboration, *Observation of a new boson at a mass of* 125 GeV *with the CMS experiment at the LHC*, Physics Letters B 716.1 (2012), pp. 30–61, DOI: 10.1016/j.physletb.2012.08.021

[3]   The ATLAS Collaboration and CMS Collaboration, *Combined Measurement of the Higgs Boson Mass in pp Collisions at $\sqrt{s} = 7$ and* 8 TeV *with the ATLAS and CMS Experiments*, Phys. Rev. Lett. 114 (2015), p. 191803, DOI: 10.1103/PhysRevLett.114.191803

[4]   The ATLAS Collaboration and CMS Collaboration, *Measurements of the Higgs boson production and decay rates and constraints on its couplings from a combined ATLAS and CMS analysis of the LHC pp collision data at $\sqrt{s} = 7$ and* 8 TeV, Journal of High Energy Physics 2016.8 (2016), p. 45, DOI: 10.1007/JHEP08(2016)045

[5]   T. Behnke et al., *The International Linear Collider Technical Design Report - Volume 1: Executive Summary* (2013), arXiv: 1306.6327 [physics.acc-ph]

[6]   B. Sowden for the ATLAS collaboration, *The Performance and Development of the Inner Detector Trigger Algorithms at ATLAS for LHC Run 2*, *Proceedings of the Division of Particles and Fields 2015*, Nov. 2015, arXiv: 1511.01136 [physics.ins-det]

[7]   The ATLAS Collaboration, *Search for the Standard Model Higgs boson produced in association with top quarks and decaying into $b\bar{b}$ in pp collisions at $\sqrt{s} =$ 13 TeV with the ATLAS detector*, tech. rep. ATLAS-CONF-2016-080, Aug. 2016, URL: https://cds.cern.ch/record/2206255

[8]   S. L. Glashow, *Partial-symmetries of weak interactions*, Nuclear Physics 22.4 (1961), pp. 579–588, DOI: 10.1016/0029-5582(61)90469-2

[9] S. Weinberg, *A Model of Leptons*, Phys. Rev. Lett. 19.21 (Nov. 1967), pp. 1264–1266, DOI: `10.1103/PhysRevLett.19.1264`

[10] A. Salam, *Elementary Particle Theory, Proceedings of the Eighth Nobel Symposium*, ed. by N. Svartholm, Almqvist & Wiksell, 1968, pp. 367–377

[11] G. 't Hooft and M. Veltman, *Regularization and renormalization of gauge fields*, Nuclear Physics B 44.1 (1972), pp. 189–213, DOI: `10.1016/0550-3213(72)90279-9`

[12] F. Englert and R. Brout, *Broken Symmetry and the Mass of Gauge Vector Mesons*, Phys. Rev. Lett. 13.9 (Aug. 1964), pp. 321–323, DOI: `10.1103/PhysRevLett.13.321`

[13] P. W. Higgs, *Broken symmetries, massless particles and gauge fields*, Physics Letters 12.2 (1964), pp. 132–133, DOI: `10.1016/0031-9163(64)91136-9`

[14] P. W. Higgs, *Broken Symmetries and the Masses of Gauge Bosons*, Phys. Rev. Lett. 13.16 (Oct. 1964), pp. 508–509, DOI: `10.1103/PhysRevLett.13.508`

[15] G. S. Guralnik, C. R. Hagen and T. W. B. Kibble, *Global Conservation Laws and Massless Particles*, Phys. Rev. Lett. 13.20 (Nov. 1964), pp. 585–587, DOI: `10.1103/PhysRevLett.13.585`

[16] P. W. Higgs, *Spontaneous Symmetry Breakdown without Massless Bosons*, Phys. Rev. 145.4 (May 1966), pp. 1156–1163, DOI: `10.1103/PhysRev.145.1156`

[17] T. W. B. Kibble, *Symmetry Breaking in Non-Abelian Gauge Theories*, Phys. Rev. 155.5 (Mar. 1967), pp. 1554–1561, DOI: `10.1103/PhysRev.155.1554`

[18] M. Thomson, *Modern Particle Physics*, Cambridge Univeristy Press, 2013, ISBN: 9781107034266

[19] D. Griffiths, *Introduction to Elementary Particles*, 2nd ed., Wiley-VCH, 2008, ISBN: 3527406018

[20] C. Patrignani et al. (Particle Data Group), *Review of Particle Physics*, Chin. Phys. C 40 (2016), p. 100001, DOI: `10.1088/1674-1137/40/10/100001`

[21] J. Goldstone, A. Salam and S. Weinberg, *Broken Symmetries*, Phys. Rev. 127.3 (Aug. 1962), pp. 965–970, DOI: `10.1103/PhysRev.127.965`

[22] D. de Florian et al., *Handbook of LHC Higgs Cross Sections: 4. Deciphering the Nature of the Higgs Sector*, tech. rep. FERMILAB-FN-1025-T, Oct. 2016, URL: `http://cds.cern.ch/record/2227475`

[23] The ATLAS Collaboration, *Search for $H \to \gamma\gamma$ produced in association with top quarks and constraints on the Yukawa coupling between the top quark and the Higgs boson using data taken at* 7 TeV *and* 8 TeV *with the ATLAS detector*, Physics Letters B 740 (2015), pp. 222–242, DOI: `10.1016/j.physletb.2014.11.049`

[24] The ATLAS Collaboration, *Search for the Standard Model Higgs boson produced in association with top quarks and decaying into $b\bar{b}$ in pp collisions at $\sqrt{s} =$* 8 TeV *with the ATLAS detector*, The European Physical Journal C 75.7 (2015), p. 349, DOI: `10.1140/epjc/s10052-015-3543-1`

[25] The ATLAS Collaboration, *Search for the associated production of the Higgs boson with a top quark pair in multilepton final states with the ATLAS detector*, Physics Letters B 749 (2015), pp. 519–541, DOI: `10.1016/j.physletb.2015.07.079`

[26] The ATLAS Collaboration, *Search for the Standard Model Higgs boson decaying into $b\bar{b}$ produced in association with top quarks decaying hadronically in pp collisions at $\sqrt{s} =$* 8 TeV *with the ATLAS detector*, Journal of High Energy Physics 2016.5 (2016), p. 160, DOI: `10.1007/JHEP05(2016)160`

[27] CMS Collaboration, *Search for the associated production of the Higgs boson with a top-quark pair*, Journal of High Energy Physics 2014.9 (2014), p. 87, DOI: `10.1007/JHEP09(2014)087`

[28] CMS Collaboration, *Search for a standard model Higgs boson produced in association with a top-quark pair and decaying to bottom quarks using a matrix element method*, The European Physical Journal C 75.6 (2015), p. 251, DOI: `10.1140/epjc/s10052-015-3454-1`

[29] F. Bezrukov, J. Rubio and M. Shaposhnikov, *Living beyond the edge: Higgs inflation and vacuum metastability*, Phys. Rev. D92.8 (2015), p. 83512, DOI: `10.1103/PhysRevD.92.083512`

[30] O. S. Brüning et al., *LHC Design Report*, tech. rep. CERN-2004-003-V-1, 2004, DOI: `10.5170/CERN-2004-003-V-1`

[31] S. Gilardoni et al., *Fifty years of the CERN Proton Synchrotron : Volume 2*, tech. rep. CERN-2013-005, Sept. 2013, DOI: `10.5170/CERN-2013-005`

[32] The ATLAS Collaboration, *Luminosity Public Results Run 2*, 2016, URL: `https://twiki.cern.ch/twiki/bin/view/AtlasPublic/LuminosityPublicResultsRun2` (visited on 26/09/2016)

[33] The ATLAS Collaboration, *The ATLAS Experiment at the CERN Large Hadron Collider*, Journal of Instrumentation 3.08 (2008), S08003, DOI: `10.1088/1748-0221/3/08/S08003`

[34] The ATLAS Collaboration, *Studies of the performance of the ATLAS detector using cosmic-ray muons*, The European Physical Journal C 71.3 (2011), p. 1593, DOI: `10.1140/epjc/s10052-011-1593-6`

[35] M. Shochet et al., *Fast TracKer (FTK) Technical Design Report*, tech. rep. CERN-LHCC-2013-007; ATLAS-TDR-021, June 2013, URL: `https://cds.cern.ch/record/1552953`

[36] B. R. Webber, *A QCD model for jet fragmentation including soft gluon interference*, Nuclear Physics B 238.3 (1984), pp. 492–528, DOI: `10.1016/0550-3213(84)90333-X`

[37] B. Andersson et al., *Parton fragmentation and string dynamics*, Physics Reports 97.2 (1983), pp. 31–145, DOI: `10.1016/0370-1573(83)90080-7`

[38] S. Agostinelli et al., *Geant4 - a simulation toolkit*, Nuclear Instruments and Methods in Physics Research Section A: Accelerators, Spectrometers, Detectors and Associated Equipment 506.3 (2003), pp. 250–303, DOI: `10.1016/S0168-9002(03)01368-8`

[39] J. Allison et al., *Geant4 developments and applications*, IEEE Transactions on Nuclear Science 53.1 (Feb. 2006), pp. 270–278, DOI: `10.1109/TNS.2006.869826`

[40] J. Allison et al., *Recent developments in Geant4*, Nuclear Instruments and Methods in Physics Research Section A: Accelerators, Spectrometers, Detectors and Associated Equipment 835 (2016), pp. 186–225, DOI: `10.1016/j.nima.2016.06.125`

[41] The ATLAS Collaboration, *The ATLAS Simulation Infrastructure*, The European Physical Journal C 70.3 (2010), pp. 823–874, DOI: `10.1140/EPJC/S10052-010-1429-9`

[42] E. Richter-Was, L. Poggioli and D. Froidevaux, *ATLFAST 2.0 a fast simulation package for ATLAS*, tech. rep. ATL-PHYS-98-131, 1998, URL: `http://cds.cern.ch/record/683751`

[43] T. Cornelissen et al., *Concepts, Design and Implementation of the ATLAS New Tracking (NEWT)*, tech. rep. ATL-SOFT-PUB-2007-007, 2007, URL: `http://cds.cern.ch/record/1020106/`

[44] W. Waltenberger, R. Frühwirth and P. Vanlaer, *Adaptive vertex fitting*, Journal of Physics G: Nuclear and Particle Physics 34.12 (Dec. 2007), N343, DOI: `10.1088/0954-3899/34/12/N01`

[45] The ATLAS Collaboration, *Electron efficiency measurements with the ATLAS detector using the 2015 LHC proton-proton collision data*, tech. rep. ATLAS-CONF-2016-024, 2016, URL: `http://cds.cern.ch/record/2157687`

[46] The ATLAS Collaboration, *Muon reconstruction performance of the ATLAS detector in proton–proton collision data at $\sqrt{s} = 13$ TeV*, The European Physical Journal C 76.5 (Mar. 2016), p. 292, DOI: `10.1140/epjc/s10052-016-4120-y`

[47] The ATLAS Collaboration, *Monte Carlo Calibration and Combination of In-situ Measurements of Jet Energy Scale, Jet Energy Resolution and Jet Mass in ATLAS*, tech. rep. ATLAS-CONF-2015-037, Aug. 2015, URL: `https://cds.cern.ch/record/2044941`

[48] The ATLAS Collaboration, *Jet Calibration and Systematic Uncertainties for Jets Reconstructed in the ATLAS Detector at $\sqrt{s} = 13$ TeV*, tech. rep. ATL-PHYS-PUB-2015-015, July 2015, URL: `https://cds.cern.ch/record/2037613`

[49] The ATLAS Collaboration, *Expected performance of the ATLAS b-tagging algorithms in Run-2*, tech. rep. ATL-PHYS-PUB-2015-022, July 2015, URL: `https://cds.cern.ch/record/2037697`

[50] The ATLAS Collaboration, *Optimisation of the ATLAS b-tagging performance for the 2016 LHC Run*, tech. rep. ATL-PHYS-PUB-2016-012, June 2016, URL: `https://cds.cern.ch/record/2160731`

[51] The ATLAS Collaboration, *Performance of missing transverse momentum reconstruction for the ATLAS detector in the first proton-proton collisions at at $\sqrt{s} = 13$ TeV*, tech. rep. ATL-PHYS-PUB-2015-027, July 2015, URL: `http://cds.cern.ch/record/2037904`

[52] T. A. Collaboration, *ATLAS Muon Combined Performance in 2016*, 2016, URL: `https://atlas.web.cern.ch/Atlas/GROUPS/PHYSICS/PLOTS/MUON-2016-004/` (visited on 03/03/2017)

[53] The ATLAS Collaboration, *Expected performance of the ATLAS experiment : detector, trigger and physics*, tech. rep. CERN-OPEN-2008-020, 2009, URL: `https://cds.cern.ch/record/1125884`

[54] The ATLAS Collaboration, *Jet energy measurement with the ATLAS detector in proton-proton collisions at $\sqrt{s} = 7$ TeV*, The European Physical Journal C 73.3 (2013), p. 2304, DOI: `10.1140/epjc/s10052-013-2304-2`

[55] W. Lampl et al., *Calorimeter Clustering Algorithms: Description and Performance*, tech. rep. ATL-LARG-PUB-2008-002. ATL-COM-LARG-2008-003, Apr. 2008, URL: `https://cds.cern.ch/record/1099735`

[56] M. Cacciari, G. P. Salam and G. Soyez, *The anti-k_t jet clustering algorithm*, Journal of High Energy Physics 2008.04 (2008), p. 63, DOI: `10.1088/1126-6708/2008/04/063`

[57] M. Cacciari and G. P. Salam, *Pileup subtraction using jet areas*, Physics Letters B 659.1-2 (2008), pp. 119–126, DOI: `10.1016/j.physletb.2007.09.077`

[58] The ATLAS Collaboration, *Tagging and suppression of pileup jets with the ATLAS detector*, tech. rep. ATLAS-CONF-2014-018, May 2014, URL: `http://cds.cern.ch/record/1700870`

[59] V. Barger, J. Ohnemus and R. J. N. Phillips, *Event shape criteria for single-lepton top-quark signals*, Phys. Rev. D 48.9 (Nov. 1993), R3953–R3956, DOI: `10.1103/PhysRevD.48.R3953`

[60] K. Cranmer et al., *HistFactory: A tool for creating statistical models for use with RooFit and RooStats*, tech. rep. CERN-OPEN-2012-016, Jan. 2012, URL: `https://cds.cern.ch/record/1456844`

[61] G. Cowan et al., *Asymptotic formulae for likelihood-based tests of new physics*, The European Physical Journal C 71.2 (2011), p. 1554, DOI: `10.1140/epjc/s10052-011-1554-0`

[62] A. L. Read, *Presentation of search results: the CL s technique*, Journal of Physics G: Nuclear and Particle Physics 28.10 (2002), p. 2693, DOI: `10.1088/0954-3899/28/10/313`

[63] D. J. Lange, *The EvtGen particle decay simulation package*, Nuclear Instruments and Methods in Physics Research Section A: Accelerators, Spectrometers, Detectors and Associated Equipment 462.1-2 (2001), pp. 152–155, DOI: `10.1016/S0168-9002(01)00089-4`

[64] P. Z. Skands, *Tuning Monte Carlo generators: The Perugia tunes*, Phys. Rev. D 82.7 (Oct. 2010), p. 74018, DOI: `10.1103/PhysRevD.82.074018`

[65] The ATLAS Collaboration, *ATLAS Run 1 Pythia8 tunes*, tech. rep. ATL-PHYS-PUB-2014-021, Nov. 2014, URL: `https://cds.cern.ch/record/1966419`

[66] The ATLAS Collaboration, *Modelling of the $t\bar{t}H$ and $t\bar{t} + $ V (V $= W, Z$) processes for $\sqrt{s} = 13$ TeV ATLAS analyses*, tech. rep. ATL-PHYS-PUB-2016-005, Jan. 2016, URL: https://cds.cern.ch/record/2120826

[67] J. Alwall et al., *The automated computation of tree-level and next-to-leading order differential cross sections, and their matching to parton shower simulations*, Journal of High Energy Physics 2014.7 (2014), p. 79, DOI: 10.1007/JHEP07(2014)079

[68] R. D. Ball et al., *Parton distributions for the LHC run II*, Journal of High Energy Physics 2015.4 (2015), p. 40, DOI: 10.1007/JHEP04(2015)040

[69] P. Artoisenet et al., *Automatic spin-entangled decays of heavy resonances in Monte Carlo simulations*, Journal of High Energy Physics 2013.3 (2013), p. 15, DOI: 10.1007/JHEP03(2013)015

[70] T. Sjöstrand et al., *An Introduction to PYTHIA 8.2*, Comput. Phys. Commun. 191 (2015), pp. 159–177, DOI: 10.1016/j.cpc.2015.01.024

[71] R. D. Ball et al., *Parton distributions with LHC data*, Nuclear Physics B 867.2 (2013), pp. 244–289, DOI: 10.1016/j.nuclphysb.2012.10.003

[72] R. Raitio and W. W. Wada, *Higgs-boson production at large transverse momentum in quantum chromodynamics*, Phys. Rev. D 19.3 (Feb. 1979), pp. 941–944, DOI: 10.1103/PhysRevD.19.941

[73] W. Beenakker et al., *NLO QCD corrections to $t\bar{t}H$ production in hadron collisions*, Nuclear Physics B 653.1-2 (2003), pp. 151–203, DOI: 10.1016/S0550-3213(03)00044-0

[74] S. Dawson et al., *Associated Higgs boson production with top quarks at the CERN Large Hadron Collider: NLO QCD corrections*, Phys. Rev. D 68.3 (Aug. 2003), p. 34022, DOI: 10.1103/PhysRevD.68.034022

[75] Y. Zhang et al., *QCD NLO and EW NLO corrections to production with top quark decays at hadron collider*, Physics Letters B 738 (2014), pp. 1–5, DOI: 10.1016/j.physletb.2014.09.022

[76] S. Frixione et al., *Electroweak and QCD corrections to top-pair hadroproduction in association with heavy bosons*, Journal of High Energy Physics 2015.6 (2015), p. 184, DOI: 10.1007/JHEP06(2015)184

[77] The ATLAS Collaboration, *Simulation of top quark production for the ATLAS experiment at $\sqrt{(}s) = 13$ TeV*, tech. rep. ATL-PHYS-PUB-2016-004, Jan. 2016, URL: https://cds.cern.ch/record/2120417

[78] P. Nason, *A new method for combining NLO QCD with shower Monte Carlo algorithms*, Journal of High Energy Physics 2004.11 (2004), p. 40, DOI: `10.1088/1126-6708/2004/11/040`

[79] S. Frixione, P. Nason and C. Oleari, *Matching NLO QCD computations with parton shower simulations: the POWHEG method*, Journal of High Energy Physics 2007.11 (2007), p. 70, DOI: `10.1088/1126-6708/2007/11/070`

[80] S. Alioli et al., *A general framework for implementing NLO calculations in shower Monte Carlo programs: the POWHEG BOX*, Journal of High Energy Physics 2010.6 (2010), p. 43, DOI: `10.1007/JHEP06(2010)043`

[81] J. M. Campbell et al., *Top-pair production and decay at NLO matched with parton showers*, Journal of High Energy Physics 2015.4 (2015), p. 114, DOI: `10.1007/JHEP04(2015)114`

[82] H.-L. Lai et al., *New parton distributions for collider physics*, Phys. Rev. D 82.7 (Oct. 2010), p. 74024, DOI: `10.1103/PhysRevD.82.074024`

[83] T. Sjöstrand, S. Mrenna and P. Skands, *PYTHIA 6.4 physics and manual*, Journal of High Energy Physics 2006.05 (2006), p. 26, DOI: `10.1088/1126-6708/2006/05/026`

[84] J. Pumplin et al., *New Generation of Parton Distributions with Uncertainties from Global QCD Analysis*, Journal of High Energy Physics 2002.07 (2002), p. 12, DOI: `10.1088/1126-6708/2002/07/012`

[85] M. Czakon and A. Mitov, *Top++: A program for the calculation of the top-pair cross-section at hadron colliders*, Computer Physics Communications 185.11 (2014), pp. 2930–2938, DOI: `10.1016/j.cpc.2014.06.021`

[86] M. Cacciari et al., *Top-pair production at hadron colliders with next-to-next-to-leading logarithmic soft-gluon resummation*, Physics Letters B 710.4-5 (2012), pp. 612–622, DOI: `10.1016/j.physletb.2012.03.013`

[87] P. Bärnreuther, M. Czakon and A. Mitov, *Percent-Level-Precision Physics at the Tevatron: Next-to-Next-to-Leading Order QCD Corrections to $q\bar{q} \to t\bar{t}+$X*, Phys. Rev. Lett. 109.13 (Sept. 2012), p. 132001, DOI: `10.1103/PhysRevLett.109.132001`

[88] M. Czakon and A. Mitov, *NNLO corrections to top-pair production at hadron colliders: the all-fermionic scattering channels*, Journal of High Energy Physics 2012.12 (2012), p. 54, DOI: `10.1007/JHEP12(2012)054`

[89] M. Czakon and A. Mitov, *NNLO corrections to top pair production at hadron colliders: the quark-gluon reaction*, Journal of High Energy Physics 2013.1 (2013), p. 80, DOI: `10.1007/JHEP01(2013)080`

[90] M. Czakon, P. Fiedler and A. Mitov, *Total Top-Quark Pair-Production Cross Section at Hadron Colliders Through $\mathcal{O}(\alpha_S^4)$*, Phys. Rev. Lett. 110.25 (June 2013), p. 252004, DOI: `10.1103/PhysRevLett.110.252004`

[91] M. Czakon, D. Heymes and A. Mitov, *High-Precision Differential Predictions for Top-Quark Pairs at the LHC*, Phys. Rev. Lett. 116.8 (Feb. 2016), p. 82003, DOI: `10.1103/PhysRevLett.116.082003`

[92] M. Czakon, D. Heymes and A. Mitov, *Dynamical scales for multi-TeV top-pair production at the LHC*, Journal of High Energy Physics 2017.4 (2017), p. 71, DOI: `10.1007/JHEP04(2017)071`

[93] F. Cascioli et al., *NLO matching for production with massive b-quarks*, Physics Letters B 734 (2014), pp. 210–214, DOI: `10.1016/j.physletb.2014.05.040`

[94] T. Gleisberg et al., *Event generation with SHERPA 1.1*, Journal of High Energy Physics 2009.02 (2009), p. 7, DOI: `10.1088/1126-6708/2009/02/007`

[95] F. Cascioli, P. Maierhöfer and S. Pozzorini, *Scattering Amplitudes with Open Loops*, Phys. Rev. Lett. 108.11 (Mar. 2012), p. 111601, DOI: `10.1103/PhysRevLett.108.111601`

[96] S. Frixione et al., *Single-top hadroproduction in association with a W boson*, Journal of High Energy Physics 2008.07 (2008), p. 29, DOI: `10.1088/1126-6708/2008/07/029`

[97] N. Kidonakis, *Two-loop soft anomalous dimensions for single top quark associated production with a W^- or H^-*, Phys. Rev. D 82.5 (Sept. 2010), p. 54018, DOI: `10.1103/PhysRevD.82.054018`

[98] N. Kidonakis, *Next-to-next-to-leading logarithm resummation for s-channel single top quark production*, Phys. Rev. D 81.5 (Mar. 2010), p. 54028, DOI: `10.1103/PhysRevD.81.054028`

[99] N. Kidonakis, *Next-to-next-to-leading-order collinear and soft gluon corrections for t-channel single top quark production*, Phys. Rev. D 83.9 (May 2011), p. 91503, DOI: `10.1103/PhysRevD.83.091503`

[100] The ATLAS Collaboration, *Monte Carlo Generators for the Production of a W or Z/γ* Boson in Association with Jets at ATLAS in Run 2*, tech. rep. ATL-PHYS-PUB-2016-003, Jan. 2016, URL: https://cds.cern.ch/record/2120133

[101] T. Gleisberg and S. Höche, *Comix, a new matrix element generator*, Journal of High Energy Physics 2008.12 (2008), p. 39, DOI: 10.1088/1126-6708/2008/12/039

[102] S. Höche et al., *QCD matrix elements + parton showers. The NLO case*, Journal of High Energy Physics 2013.4 (2013), p. 27, DOI: 10.1007/JHEP04(2013)027

[103] The ATLAS Collaboration, *Measurement of W and Z Boson Production Cross Sections in pp Collisions at $\sqrt{s} = 13$ TeV in the ATLAS Detector*, tech. rep. ATLAS-CONF-2015-039, Aug. 2015, URL: https://cds.cern.ch/record/2045487

[104] The ATLAS Collaboration, *Measurement of the inclusive $W^{\pm}$ and Z/γ^* cross sections in the e and μ decay channels in pp collisions at $\sqrt{s} = 7$ TeV with the ATLAS detector*, Phys. Rev. D 85.7 (Apr. 2012), p. 72004, DOI: 10.1103/PhysRevD.85.072004

[105] The ATLAS Collaboration, *Multi-Boson Simulation for 13 TeV ATLAS Analyses*, tech. rep. ATL-PHYS-PUB-2016-002, Jan. 2016, URL: https://cds.cern.ch/record/2119986

[106] The ATLAS Collaboration, *Selection of jets produced in 13 TeV proton-proton collisions with the ATLAS detector*, tech. rep. ATLAS-CONF-2015-029, July 2015, URL: https://cds.cern.ch/record/2037702

[107] The ATLAS Collaboration, *Estimation of non-prompt and fake lepton backgrounds in final states with top quarks produced in proton-proton collisions at $\sqrt{s} = 8$ TeV with the ATLAS detector*, tech. rep. ATLAS-CONF-2014-058, Oct. 2014, URL: http://cds.cern.ch/record/1951336

[108] The ATLAS Collaboration, *Improved luminosity determination in pp collisions at $\sqrt{s} = 7$ TeV using the ATLAS detector at the LHC*, The European Physical Journal C 73.8 (2013), p. 2518, DOI: 10.1140/epjc/s10052-013-2518-3

[109] The ATLAS Collaboration, *Luminosity determination in pp collisions at $\sqrt{s} = 8$ TeV using the ATLAS detector at the LHC*, The European Physical Journal C 76.12 (2016), p. 653, DOI: 10.1140/epjc/s10052-016-4466-1

[110] S. van der Meer, *Calibration of the effective beam height in the ISR*, tech. rep. CERN-ISR-PO-68-31. ISR-PO-68-31, 1968, URL: https://cds.cern.ch/record/296752

[111] The ATLAS Collaboration, *Electron and photon energy calibration with the ATLAS detector using data collected in 2015 at $\sqrt{s} = 13$ TeV*, tech. rep. ATL-PHYS-PUB-2016-015, Aug. 2016, URL: https://cds.cern.ch/record/2203514

[112] The ATLAS Collaboration, *Performance of algorithms that reconstruct missing transverse momentum in $\sqrt{s} = 8$ TeV proton-proton collisions in the ATLAS detector*, The European Physical Journal C 77.4 (2017), p. 241, DOI: 10.1140/epjc/s10052-017-4780-2

[113] The ATLAS Collaboration, *Calibration of b-tagging using dileptonic top pair events in a combinatorial likelihood approach with the ATLAS experiment*, tech. rep. ATLAS-CONF-2014-004, Feb. 2014, URL: https://cds.cern.ch/record/1664335

[114] The ATLAS Collaboration, *Performance of b-jet identification in the ATLAS experiment*, Journal of Instrumentation 11.04 (2016), P04008, DOI: 10.1088/1748-0221/11/04/P04008

[115] A. D. Martin et al., *Parton distributions for the LHC*, The European Physical Journal C 63.2 (2009), pp. 189–285, DOI: 10.1140/epjc/s10052-009-1072-5

[116] The ATLAS Collaboration, *Measurements of fiducial cross-sections for $t\bar{t}$ production with one or two additional b-jets in pp collisions at $\sqrt{s} = 8$ TeV using the ATLAS detector*, The European Physical Journal C 76.1 (2016), p. 11, DOI: 10.1140/epjc/s10052-015-3852-4

[117] CMS Collaboration, *Measurement of $t\bar{t}$ production with additional jet activity, including b quark jets, in the dilepton decay channel using pp collisions at $\sqrt{s} = 8$ TeV*, The European Physical Journal C 76.7 (2016), p. 379, DOI: 10.1140/epjc/s10052-016-4105-x

[118] G. Cowan, *University of London Postgraduate Lectures for Particle Physicists*, 2016, URL: http://www.pp.rhul.ac.uk/~cowan/stat_course.html

[119] J. Neyman and E. S. Pearson, *On the Problem of the Most Efficient Tests of Statistical Hypotheses*, Breakthroughs in Statistics: Foundations and Basic Theory, Springer New York, 1992, pp. 73–108, ISBN: 978-1-4612-0919-5, DOI: 10.1007/978-1-4612-0919-5_6

[120] T. Hastie, R. Tibshirani and J. Friedman, *The Elements of Statistical Learning*, 2nd ed., Springer-Verlag New York, 2009, ISBN: 978-0-387-84858-7, DOI: `10.1007/978-0-387-84858-7`

[121] T. Hastie et al., *Multi-class AdaBoost*, Statistics and Its Interface 2.3 (2009), pp. 349–360, DOI: `10.4310/SII.2009.v2.n3.a8`

[122] J. Gallicchio and M. D. Schwartz, *Seeing in Color: Jet Superstructure*, Phys. Rev. Lett. 105.2 (July 2010), p. 022001, DOI: `10.1103/PhysRevLett.105.022001`

[123] The ATLAS Collaboration, *Measurement of colour flow with the jet pull angle in $t\bar{t}$ events using the ATLAS detector at $\sqrt{s} = 8$ TeV*, Physics Letters B 750 (2015), pp. 475–493, DOI: `10.1016/j.physletb.2015.09.051`

[124] D. Buskulic et al., *Performance of the ALEPH detector at LEP*, Nuclear Instruments and Methods in Physics Research Section A: Accelerators, Spectrometers, Detectors and Associated Equipment 360.3 (1995), pp. 481–506, DOI: `10.1016/0168-9002(95)00138-7`

[125] The ATLAS Collaboration, *Search for the Associated Production of a Higgs Boson and a Top Quark Pair in Multilepton Final States with the ATLAS Detector*, tech. rep. ATLAS-CONF-2016-058, Aug. 2016, URL: `https://cds.cern.ch/record/2206153`

[126] The ATLAS Collaboration, *Measurement of fiducial, differential and production cross sections in the $H \rightarrow \gamma\gamma$ decay channel with $13.3\,\mathrm{fb}^{-1}$ of 13 TeV proton-proton collision data with the ATLAS detector*, tech. rep. ATLAS-CONF-2016-067, Aug. 2016, URL: `https://cds.cern.ch/record/2206210`

[127] The ATLAS Collaboration, *Combination of the searches for Higgs boson production in association with top quarks in the $\gamma\gamma$, multilepton, and $b\bar{b}$ decay channels at $\sqrt{s} = 13$ TeV with the ATLAS Detector*, tech. rep. ATLAS-CONF-2016-068, Aug. 2016, URL: `https://cds.cern.ch/record/2206211`